

HARD STATE MANIFESTATIONS OF GALACTIC BLACK HOLE TRANSIENTS

by
Tolga Dinçer

Submitted to the Graduate School of Engineering and Natural Sciences
in partial fulfillment of
the requirements for the degree of
Doctor of Philosophy

Sabancı University
August 2013

TITLE OF THE THESIS/DISSERTATION

APPROVED BY:

Asst. Prof. Dr. / Assoc. Prof. Dr. / Prof. Dr. Emrah Kalemi *Emrah Kalemi*
(Thesis Supervisor)

Asst. Prof. Dr. / Assoc. Prof. Dr. / Prof. Dr. Tansel Ak *Tansel Ak*

Asst. Prof. Dr. / Assoc. Prof. Dr. / Prof. Dr. M. Ali Akar *M. Ali Akar*

Asst. Prof. Dr. / Assoc. Prof. Dr. / Prof. Dr. Ünal Ertan *Ünal Ertan*

Asst. Prof. Dr. / Assoc. Prof. Dr. / Prof. Dr. Müjdat Getin *Müjdat Getin*

DATE OF APPROVAL: day/month/year

13/08/2013

© Tolga DiŇer 2013

All Rights Reserved

Abstract

HARD STATE MANIFESTATIONS OF GALACTIC BLACK HOLE TRANSIENTS

Tolga Dinçer

Physics, Ph.D. Thesis, 2013

Supervisor: Emrah Kalemci

Keywords: *astrophysical jets, black holes, compact objects*

This thesis is aimed at understanding the accretion-ejection processes and the physical environment in the vicinity of the Galactic black hole transients (GBHT) in the hard state. In this context, X-ray spectral and temporal, optical/infrared (OIR) photometric and radio properties of GBHTs during the outburst decay are examined. As part of developing analysis techniques for this aim, we first investigate a jet associated brightening in the OIR light curves of GX 339-4 during its 2011 outburst decay. The spectral energy distributions taken at the rising part of the OIR rebrightening yield flat spectra, indicating components other than optically thin emission from the compact jet. Again during the rising part of the brightening we detected fluctuations with the binary period of the system. Then, for a large sample of sources, we investigate the relation between the jet formation and the changes or differences in the short term X-ray variability, especially low frequency quasi periodic oscillations. We find that the X-ray variability patterns differ with respect to the source's track in the radio X-ray correlation. We also discuss the nature of X-ray spectral softening within a few days prior to or following the start of the indications of the jet activity. Finally, we compare the relation between the spectral hardness and the reflection amplitude of black hole and neutron star systems to discuss the nature of their differences.

Özet

GALAKSİMİZDEKİ KARA DELİK GEÇİCİLERİNİN SERT DÖNEM MANİFESTOLARI

Tolga Dinçer

Fizik, Doktora Tezi, 2013

Danışman: Emrah Kalemci

Anahtar kelimeler: *astrofiziksel jetler, kara delikler, tıknaz cisimler*

Bu tez galaksimizdeki kara delik geçicilerinin yığılma-püskürtme süreçlerini ve fiziksel çevrelerini anlamaya yöneliktir. Bu bağlamda, kara delik geçicilerinin patlama sönümü esnasındaki X-ışını tayfsal ve zamansal, görsel/kızılötesi fotometrik ve radyo özellikleri incelendi. Öncelikle, geliştirdiğimiz analiz tekniklerini kullanarak GX 339-4 kara delik geçicisinin 2011 yılı patlama sönümü esnasındaki jet kaynaklı olduğu düşünülen görsel/kızılötesi ışık eğrilerindeki parlamayı inceledik. Parlamaların ilk aşamalarından elde edilen tayfsal enerji dağılımlarının, optikçe ince jet emisyonundan farklı nitelik gösteren düz bir tayfa sahip olduğu bulundu. Yine bu parlamaların ilk aşamalarında sistemin yörünge periyoduna ait salınımlar gözlemlendi. Daha sonra, çok sayıda kaynak için, jet oluşumu ve kısa dönem X-ışını değişkenliği arasındaki ilişkiyi inceledik. Başta, düşük frekanslı periyodığe yakın salınımlar olmak üzere X-ışını değişkenliğindeki değişimlere ya da farklılıklara göz attık. X-ışını değişkenliğindeki davranışların radyo / X-ışını lüminozite ilişkisindeki kaynaklara göre ayrıldığında farklılık gösterdiğini bulduk. Ayrıca jet oluşumundan birkaç gün önce ya da sonra gözlenen X-ışını tayfindaki yumuşamanın doğasını tartıştık. Son olarak nötron yıldızı ve kara delik sistemleri arasındaki farklılıkların doğasını anlamak için her iki sistemdeki tayfsal sertlik ve yansıma genliği arasındaki ilişkiyi karşılaştırdık.

Acknowledgements

First of all, I would like to thank my supervisor Emrah Kalemci for his guidance, support and for all the things that I have learnt from him. I also thank for his patience when I am not doing well. I owe him much. I must also say that this thesis would not finish without his help.

Then, I would like to thank to my thesis juries Ali Alpar, Müjdat Çetin, Ünal Ertan, and Tansel Ak for their patience, constructive criticism and helpful advices.

It is a pleasure to thank all members of the astrophysics group in Sabancı University who taught me and with whom I worked or had discussions.

This thesis would not have been possible if Michelle Buxton and Charles Bailyn in Yale Astronomy Department did not conduct the SMARTS observations of black hole systems. I would like to thank them for sharing their data with me. The works in Chapter 3 involved collaboration with John A. Tomsick, Michelle M. Buxton, Charles D. Bailyn and Stephane Corbel. I would like to thank all of them for their contribution. The text in that chapter is reprint of the material published in *Astrophysical Journal*. I would like to thank Tomaso Belloni for his reading the draft and valuable comments before it is sent for publication. The idea that led to the work in Chapter 6 originally belongs to Marat Gilfanov. I visited him at Max Planck Institut für Astrophysik and conducted part of the work there. I would like to thank him for sharing his idea and for his hospitality during my stay in Max Planck. I also would like to thank all scientists who contributed to the Tübingen Timing Tools. Without those tools, the timing analysis in this thesis would be a pain in the neck for me.

I acknowledge financial supports from the Scientific and Technical Research Council of Turkey (TÜBİTAK) through grants 106T570 and 111T222, and also from FP6 Marie Curie Actions Transfer of Knowledge (ASTRONS, MTKD-CT-2006-042703) and FP7 Initial Training Network Black Hole Universe, ITN 215212.

I also would like to thank some friends that I spend great times in Sabancı University: Göktuğ Karpat, Cenk Yanık, Barış Çakmak, Aykut Teker, Zeynep Sungur, Nur F. Tortop, Tuna Demircik (the best company for the sports activities) and Ece Kurtaraner - glad to catch up with all of you. A special thanks goes to İskender Yalçınkaya, I will not forget our cooking sessions and also miss the times that we played in the same jazz band.

Lastly, I would like to thank my parents for all their support and sacrifice during my time away from them.

Contents

1	Introduction	1
1.1	Black hole X-ray binaries	2
1.1.1	Physical properties of a black hole	3
1.1.2	Formation of a black hole	3
1.1.3	How do we claim an X-ray binary harbor a black hole?	4
1.2	Classification of black hole X-ray binaries	5
1.3	Outburst mechanisms	6
1.4	Observational properties of black hole X-ray binaries	8
1.4.1	X-ray states	8
1.4.2	Multiwavelength emission properties	11
1.4.3	Accretion-ejection models and multiwavelength emission mechanisms	14
2	X-ray instruments and data analysis	22
2.1	X-ray instruments	22
2.1.1	The Rossi X-ray Timing Explorer	22
2.1.2	Swift X-ray telescope	23
2.2	Timing analysis	24
2.2.1	The discrete Fourier transform	24
2.2.2	The power spectral density (PSD)	25
2.3	Spectral Analysis and Models	28
2.3.1	Spectral Analysis	28
2.3.2	Spectral Models	28
3	X-Ray, optical and infrared observations of GX 339-4 during its 2011 outburst decay	31
3.1	Introduction	31
3.2	Observations and data analysis	31
3.2.1	<i>RXTE</i> observations	31
3.2.2	<i>Swift</i> observations	32
3.2.3	SMARTS observations	33
3.3	Results	33
3.3.1	X-ray evolution	33
3.3.2	No evidence for softening	36
3.3.3	Light curves	36
3.3.4	Evidence for binary period in the optical light curves	38
3.3.5	SEDs	42
3.4	Discussion	42
3.4.1	Evolution in the X-ray regime	43

3.4.2	Origin of OIR emission on the initial decay	44
3.4.3	Rebrightening due to a jet?	44
3.4.4	Understanding the broadband SEDs	44
3.4.5	On the modulations of the OIR light curves	46
4	Accretion–Jet process and X-ray variability	47
4.1	Introduction	47
4.2	Data analysis	47
4.2.1	Spectral analysis	47
4.2.2	Temporal analysis	48
4.2.3	Transitions	48
4.3	Results	51
4.3.1	Evolution of the peak frequencies	55
4.3.2	Changes in the evolution of the L_3	55
4.3.3	Evolution of the type-C QPOs	56
4.3.4	Rms variability: Tracks in the radio-X-ray luminosity relation	57
4.3.5	ν_{QPO} -luminosity relation	57
4.4	Discussion	60
4.4.1	Constraining the QPO behavior	60
4.4.2	Connection between the radio-X-ray luminosity plane and the broadband X-ray variability	61
4.4.3	Evaluating the predictions of the MDAF theory	62
5	Softening of the X-ray spectrum during outburst decays	76
5.1	Introduction	76
5.2	Observations and data analysis	76
5.3	Evolution of the softening during outburst decays	77
5.3.1	4U 1543–47	77
5.3.2	GX 339–4	77
5.3.3	XTE J1550–564	79
5.3.4	XTE J1118+480	79
5.3.5	GRO J1655–40	80
5.3.6	H 1743–322	81
5.4	Relation of the photon index to the ELF	81
5.5	Power-law ELF decay rate	82
5.6	Discussion	83
6	Reflection in neutron star and black hole X-ray binaries	86
6.1	Introduction	86
6.2	Observations and data reduction	87
6.3	Spectral model	87
6.4	Compton- γ -R relation	88
6.5	Discussion	89
7	Conclusions	91
	Bibliography	93

List of Figures

1.1	Energy and power spectra of the hard and the soft states of a black hole Cyg X-1.	9
1.2	Sketch of the general behavior of a black hole X-ray binary in the HID and HRD, with the HID regions corresponding to the X-ray states.	10
1.3	Jets resolved in radio images of black hole systems.	11
1.4	Radio, hard and soft X-ray monitoring of GX 339-4 during its outburst in 1997/1998.	12
1.5	Radio and X-ray luminosities for Galactic accreting black hole binaries during the hard and quiescent states	13
1.6	The main components of the X-ray emission from an accreting black hole (left) and a plausible geometry of the accretion flow in the hard state (right). Adapted from Gilfanov (2010).	15
1.8	Schematic diagram of the MDAF model for the BHXB GRS 1915+105.	19
1.9	Spectrum from a standard canonical jet emission model.	21
2.1	Schematic of the <i>RXTE</i> spacecraft	23
2.2	An illustration of Swift satellite	24
2.3	Lorentzian fit to a typical PSD.	27
3.1	Evolution of the X-ray parameters and the OIR light curves of GX 339-4	35
3.2	Hardness-intensity diagram of GX 339-4	37
3.3	Evolution of the photon index from <i>RXTE</i> and <i>Swift</i>	38
3.4	X-ray and OIR light curves of GX 339-4	39
3.5	Sinusoidal fits to the OIR light curves.	40
3.6	OIR SEDs sampled from different stages of both the intermediate and the hard states.	41
3.7	Broadband SEDs of GX 339-4 for two selected days.	43
4.1	The changes that marks the timing, index, and IR (right) transitions for 4U-1543-47	49
4.2	Evolution of the X-ray power spectral parameters along with the IR and/or radio information for all the outburst decays	52
4.3	The total rms amplitude vs the qpo rms amplitude for all type-C QPOs.	56
4.4	Rms amplitude of variability vs photon index (Γ)	58
4.5	Rms amplitude of variability vs Eddington luminosity fraction	59
4.6	Peak frequency of the type-C QPO vs total ELF	60
4.7	Evolution of the PSD modeled with Lorentzians for 4U 1543-47 during its 2002 outburst decay.	64

4.8	Evolution of the PSD modeled with Lorentzians for H 1743–322 during its 2003 outburst decay.	65
4.9	Evolution of the PSD modeled with Lorentzians for H 1743–322 during its 2008 outburst decay.	66
4.10	Evolution of the PSD modeled with Lorentzians for H 1743–322 during its 2009 outburst decay.	67
4.11	Evolution of the PSD modeled with Lorentzians for GRO J1655–40 during its 2005 outburst decay.	68
4.12	Evolution of the PSD modeled with Lorentzians for GX 339–4 during its 2003 outburst decay.	69
4.13	Evolution of the PSD modeled with Lorentzians for GX 339–4 during its 2005 outburst decay.	70
4.14	Evolution of the PSD modeled with Lorentzians for GX 339–4 during its 2007 outburst decay.	71
4.15	Evolution of the PSD modeled with Lorentzians for GX 339–4 during its 2011 outburst decay.	72
4.16	Evolution of the PSD modeled with Lorentzians for XTE J1550–564 during its 2000 outburst decay.	73
4.17	Evolution of the PSD modeled with Lorentzians for XTE J1720–318 during its 2003 outburst decay.	74
4.18	Evolution of the PSD modeled with Lorentzians for XTE J1752–223 during its 2010 outburst decay.	75
5.1	Time evolution of the softening for 4U 1543–47	78
5.2	Time evolution of the softening for GX 339–4	78
5.3	Time evolution of the softening for XTE J1550–564	79
5.4	Time evolution of the softening for XTE J1550–564	80
5.5	Time evolution of the softening for XTE J1118+480	80
5.6	Time evolution of the softening for GRO J1655–40	81
5.7	Time evolution of the softening for H 1743–322	82
5.8	Relation between the photon index and Eddington luminosity fraction	83
5.9	Time evolution of the power-law ELF for GBHTs that show significant evidence for softening and lack of evidence for softening	84
6.1	HIDs of 4U 1608–52 and Aql X–1 observed with the <i>RXTE</i> /ASM.	87
6.2	Compton- γ parameter vs reflection amplitude for both BHXBs and atolls	89
6.3	T_{seed} and T_e dependence of the correlation between the Compton- γ parameter and the reflection amplitude for 4U 1608–52.	90

List of Tables

1.1	Properties of BHXBs	7
3.1	Observational Parameters Obtained from <i>RXTE</i> Data	34
3.2	Model Parameters Derived from the Light Curves (for a Fixed Period $P =$ 1.77 days)	41
4.1	Transition times of GBHTs during outburst decay	55
5.1	E-folding decay rates of the power-law ELF's	85
6.1	Hydrogen column densities of BHXBs and atolls used in the spectral fits .	88

LIST OF ABBREVIATIONS

- ADAF:** Accretion dominated accretion flow
- ASM:** All sky monitor
- BAT:** Burst Array Telescope
- BH:** Black hole
- BHXB:** Black hole X-ray binary
- ELF:** Eddington luminosity fraction
- FFT:** Fast Fourier transform
- FWHM:** Full width half maximum
- GBHT:** Galactic black hole transient
- GTI:** Good time interval
- HEXTE:** High Energy X-ray Timing Explorer
- HID:** Hardness-intensity diagram
- HIMS:** Hard intermediate state
- HRD:** Hardness-rms diagram
- IDL:** Interactive Data Language
- IR:** Infrared
- ISCO:** Innermost stable circular orbit
- MDAF:** Magnetically dominated accretion flow
- MJD:** Modified Julian Day, MJD is Julian Day JD–2400000.5
- MRI:** Magneto-rotational instability
- NS:** Neutron star
- NSXB:** Neutron star X-ray binary
- OIR:** Optical and infrared
- PCA:** Proportional Counter Array

PCU: Proportional Counter Unit

PSD: Power spectral density

SED: Spectral energy distribution

SIMS: Soft intermediate state

SN: Supernova

QPO: Quasi-periodic oscillation

RXTE: Rossi X-ray Timing Explorer

WD: White dwarf

XRT: X-ray telescope

CHAPTER 1

Introduction

Galactic black hole transients are accreting binary systems that undergo sporadic outbursts that last for months to years. Years of intense monitoring observations of these sources with X-ray space telescopes show that during an outburst they exhibit two main states with correlated spectral and temporal properties: the hard and the soft state (Remillard & McClintock, 2006; Belloni, 2010). In the soft state, the X-ray spectrum of the source is dominated by emission from an optically thin, geometrically thick accretion disk and the variability is weak. In the hard state, the X-ray spectrum shows a power-law component extending to hard X-rays, the variability is very strong (with rms amplitude exceeding 30%) and the power spectrum sometimes show peaks that indicate quasi-periodic oscillations (QPO) in the system. The physical origin of the power-law component in the X-ray spectrum is still debated, but common models imply a hot inner flow (plasma of electrons, perhaps in the form of a corona) surrounding the black hole or the base of compact jets. Likewise the origin of the QPOs is still a mystery.

Besides the correlated X-ray properties, black hole transients also exhibit state dependent optical, infrared and radio properties (Fender, 2006). In the hard state, there is significant contribution from compact jets from radio to optical frequencies in the form of synchrotron emission whereas in the soft state, the jet related emission is quenched in all wavelengths. In the past decade, the transitions from the soft to hard state attracted significant attention as it serves the perfect conditions to study the properties of the accretion and the jet formation. Until recently it was not possible to obtain the jet formation times with radio observations due to poor coverage. Better coverage was obtained in optical and infrared thanks to the SMARTS telescopes allowing us to track the formation of compact jet (Jain et al., 2001; Buxton & Bailyn, 2004). At the time of writing this thesis a couple of black hole transients were covered in all wavelengths throughout the outbursts allowing detailed investigation of the relation between the formation of jets and X-ray spectral and temporal properties (Chun et al., 2013; Corbel et al., 2013b).

In spite of these progresses, we do not have a clear picture of how a transition from accretion disk dominated soft state to the hard state leads to the formation of compact jets. Moreover, we currently lack the phenomenology to understand how the formation of compact jet affects the accretion properties of black hole transients. For example, the hard state is known to show a softening of the X-ray spectrum at low flux levels but its relation to the jet formation remains unexplored. Another example is related to the short term X-ray variability. During the hard to soft state transition on the outburst rise, a connection between the disappearance of X-ray variability and formation of powerful radio flares was investigated (Fender et al., 2009). On the other hand, a systematic study of the relation of QPO parameters to the formation of compact steady jets in the hard state during the

outburst decay has never been done. The work in this thesis contributed to these efforts in terms of analysis and interpretation of multiwavelength data.

The thesis is structured as follows. This chapter is an introduction to black hole X-ray binaries. Chapter 2 introduces the X-ray instruments, and the data analysis methods and techniques used in this thesis. Chapter 3 through 6 present the recent work done which consists of four projects. In Chapter 3, we investigate a jet associated brightening in the optical and infrared light curves during a recent outburst decay of a black hole transient. In Chapter 4, we relate the jet formation to the changes or differences in the short term X-ray variability using a larger set of black hole sources. In Chapter 5, we discuss the nature of the softening of the X-ray spectrum. Apart from these, we compare the relation between the spectral hardness and the reflection amplitude of black hole and neutron star systems in Chapter 6. Finally, the conclusions can be found in Chapter 7.

1.1 Black hole X-ray binaries

Black hole X-ray binaries are systems that consist of a black hole and a normal star revolving around each other by gravitational attraction. When the separation between the two are small, roughly on the order of the diameter of the normal star, the black hole accretes matter from the surface of the normal star (also called the donor star). Due to angular momentum conservation, the matter leaving the normal star does not directly fall onto the compact object but goes into orbit around it. The transferred matter forms an accretion disk in which it spirals slowly inwards due to viscosity-induced transfer of angular momentum outwards. As a result of this process, a considerable fraction of the gravitational potential energy of the infalling matter goes to heating the accretion disk, resulting in a disk luminosity that can be approximated by:

$$L_{acc} = 2\eta \frac{GM\dot{M}}{R_S} = \eta \dot{M}c^2 \quad (1.1)$$

(Shapiro & Teukolsky, 1983) where $\eta = 0.057-0.42$, depending on the angular momentum of the BH. Realistic values of \dot{M} and η yield a typical luminosity of $\sim 10^{37}$ ergs/s for an accretion onto a BH binary system. This luminosity matches the observed X-ray luminosity from BHXBs. There is a theoretical maximum X-ray luminosity that can be radiated by the compact object of mass M , so-called the Eddington limit or the Eddington luminosity. This limit is achieved when the inward gravitational force balances the the outward radiation pressure on the ionized plasma. For a steady and spherically symmetric accretion flow:

$$F_{grav} = F_{rad} \iff \frac{GMm_p}{D^2} = \frac{L\sigma_T}{4\pi D^2 c} \quad (1.2)$$

where σ_T is the Thomson cross-section and c is the speed of light and m_p is the mass of a proton. The Eddington luminosity is then:

$$L_{Edd} = \frac{4\pi GMm_p c}{\sigma_T} \approx 1.3 \times 10^{38} \left(\frac{M}{M_\odot} \right) \text{ ergs}^{-1} \quad (1.3)$$

It depends only on the mass of the black hole. If the observed accretion luminosity of the source exceeds this limit, the source switches off the accretion. If some or all of the

observed luminosity is produced by other means, for instance nuclear burning, the outer layers of material begins to be blown off and the source cannot remain steady.

The analysis and interpretation of the observations of black hole X-ray binaries requires a theoretical understanding of the black holes. Moreover, the observed emission properties of black hole X-ray binaries show similarities to those of some neutron star X-ray binaries. Therefore, first I summarize the physical properties of black holes, next briefly discuss the formation of NSs and BHs in X-ray binaries, and finally explain how we claim an X-ray binary harbor a black hole.

1.1.1 Physical properties of a black hole

In general relativity, a black hole (BH) is the vacuum solution of Einstein's field equations of a point like object whose mass is completely concentrated at the center of the object. There exists a boundary that separates the inside of the BH from the rest of the universe which is called the event horizon. The radius of the event horizon is defined as

$$R_H = \frac{GM}{c^2} [1 + (1 - a^2)^{1/2}] \quad (1.4)$$

where a is the dimensionless spin parameter of the black hole:

$$0 \leq a = \frac{cJ}{GM^2} < 1 \quad (1.5)$$

where c is the speed of light and J is the spin angular momentum of the black hole.

This boundary is not made of any material. So, a BH does not possess hard surface. All events that occur inside the event horizon are forever hidden from an outside observer. The gravity is so high that once inside, particles and even light can never escape to the outside. Since matter can fall in but never leave, the mass of a BH can only increase. Consequently, the surface area of the event horizon would only increase. For a non-rotating BH, $R_H = 2GM/c^2$ and it is called the Schwarzschild radius R_S . For a maximally rotating BH, $R_H = GM/c^2 = R_S/2$.

In general relativity, a dynamically important parameter of a BH is the innermost stable orbit (ISCO). Circular orbits outside the ISCO are stable to small perturbations, but those inside the ISCO are unstable. For a non-rotating BH, $R_{ISCO} = 3R_S$ whereas for a maximally rotating BH, $R_{ISCO} = R_S/2$ if the orbit corotates with the BH and $R_{ISCO} = 4.5R_S$ if it counter rotates. When the material reaches the ISCO, stable orbits are no more available, so the material free falls into the black hole.

1.1.2 Formation of a black hole

During its life, a normal star is in equilibrium between the inward gravitational force and the outward radiation force. The main source of the radiation is the nuclear fusion in the central regions. When the star runs out of nuclear fuel, the inward gravitational pull cannot be counterbalanced by the radiation force or thermal pressure. The star collapses until some other form of force enables an equilibrium against the gravitation. The equilibrium is sustained in three types of compact objects: white dwarfs (WD), neutron stars (NS) and black holes (BH). In WDs and NSs, the equilibrium is attained by the Fermionic repulsion. WDs are supported by degenerate electron pressure, NSs by degenerate neutron

pressure. BHs, on the other hand, are completely collapsed stars that could not provide any resistance against the gravitational pull, and therefore are collapsed to singularities.

The mass of the progenitor (M_P) determines the type of the resultant compact object. When $6M_\odot < M_P < 8M_\odot$, there is only contraction of the star and a WD is formed (Smartt, 2009). Note that, a white dwarf has a theoretical maximum mass $\sim 1.4M_\odot$ and it is called the Chandrasekhar mass limit. If the WD increases its mass by accreting matter, it explodes as a type Ia supernova (SN). When $M_P > 8M_\odot$, thermonuclear SN explosions of different types are produced (type Ib, Ic and no H lines; Types II and H lines). At the end of these SN explosions, a NS or a BH is formed.

1.1.3 How do we claim an X-ray binary harbor a black hole?

The compact object in XBs can be a WD, NS or a BH (see Section 1.1.2). In order to observationally claim that the compact object is a BH, one has to show the presence of its event horizon. Currently this is impossible with direct imaging method because of their small sizes and large distances. Therefore, indirect methods are often invoked to determine whether the compact object is a BH or not.

The most reliable indirect method is to determine its mass. As mentioned earlier, WDs have a theoretical maximum mass limit (see Section 1.1.2). Similarly, NSs also have a theoretical maximum mass above which the gravitational collapse is unavoidable (Oppenheimer & Volkoff, 1939). This mass has not been determined with good accuracy because of the uncertainty in the equation of state of NSs and due to factors such as spin. However, most theoreticians find $3M_\odot$ is a safe upper limit for the mass of a NS (e.g. Kalogera & Baym, 1996). So, if the mass of the compact object is greater than $3M_\odot$, it can be claimed as a BH.

How do we measure the mass of a compact object in XBs? The most accurate mass measurement in astrophysics is via dynamical method. When the stellar companion is bright enough, it is sometimes possible to identify the absorption lines in the optical spectrum of the stellar companion. The absorption lines in the optical spectrum show a Doppler shift because the stellar companion orbits around the compact object. This Doppler shift gives the radial velocity of the stellar companion. If the radial velocity and the binary period of the system are known, they can be used to calculate the mass function of a binary system:

$$f(M_1, M_2, i) \equiv \frac{(M_2 \sin i)^3}{(M_1 + M_2)^2} = \frac{P_{orb} v_1^3}{2\pi G} \quad (1.6)$$

where P_{orb} is the orbital period of the system, v_1 is the radial velocity of the companion star obtained from Doppler shift, i is the inclination angle of the system with respect to the line of sight, M_2 is the mass of the compact object and M_1 is the mass of the stellar companion. The mass function does not give the mass of the compact object but provides a lower limit by setting $M_1 = 0$ and $i = 90^\circ$. A lower limit exceeding $3M_\odot$ is enough to claim a BH. For a tighter constraint on the mass of the compact object, the mass of the stellar companion can be approximated through its spectral class, and the inclination of the system can be approximated through eclipses (or lack of).

There are also XBs which are thought to harbor a black hole even though the mass of the compact object cannot be dynamically measured. The presence of a BH in those

systems are referred from the similarity of their observational X-ray properties to that of known BHXBs. These X-ray properties are characteristic X-ray spectrum, state dependent variability properties, quasi-periodic oscillations (QPOs) in 0.1-450 Hz range, and also the radio and near-infrared (NIR) properties. However, NSs and BHs have similar gravitational potential wells. Hence the accretion and ejection processes in low magnetic field NS can be very similar and they may show similar X-ray, radio and NIR characteristics to that of BHXBs. Type-I X-ray bursts and coherent pulsations have been used to identify the NSs since they require a surface.

Recent works have presented some other differences between the NSs and BHs. These are, for instance; i) BHXBs are generally under-luminous in the quiescence compared to NSXBs (McClintock et al., 2004), which is possibly because some of the energy is advected into the black hole without being radiated away (Narayan et al., 1996); ii) unlike BHXBs, NSXBs show aperiodic variability at frequencies > 100 Hz which is possibly due to absence of hard surface and therefore a boundary layer (Sunyaev & Revnitsev, 2000); iii) some BHXBs show higher radio luminosity than NSs at a given X-ray luminosity (Migliari & Fender, 2006); iv) at highest luminosities, the NSXBs exhibit boundary layer emission as the disk matter interacts with the surface of the NS but BHXBs do not (see e.g. Revnitsev et al., 2013). In Chapter 6, we present another difference in X-ray spectral properties of BHXBs and weak magnetic field NSXBs.

1.2 Classification of black hole X-ray binaries

Depending on the observational properties of BHXBs, there several classification schemes used in the literature.

The first one depends on the identification of the black hole, i.e. dynamically (mass function) identified and observationally identified. Dynamically identified ones either have $f \geq 3M_{\odot}$ or their estimated masses are greater than $3M_{\odot}$. The sources without mass function measurements, but showing observationally similar characteristics to GBHs are called the observationally identified black holes. I show all known BHXBs in Table 1.1.

The second one depends on the mass of the companion star. Consequently, they are sub-categorized into two classes:

- Low-mass BHXBs: $M_{donor} < 1M_{\odot}$
- High-mass BHXBs: $M_{donor} > 10M_{\odot}$.

In high-mass BHXBs, the donor is an early type star (O or B). The binary periods are typically several days. High-mass BHXBs contain a supergiant (SG) O or B type star. The mass transfer is via a strong stellar wind and/or Roche lobe overflow. The X-ray emission is persistent, and large variability is common. In low-mass BHXBs, the donor has a spectral type later than B. Although the binary periods of low-mass BHXBs range from hours to several days, they are typically < 24 h and the orbits are usually circular.

A third classification depends on the X-ray activity. Some BHXBs are persistently visible whereas other BHXBs are only visible when they undergo outbursts. So according to their X-ray activity, the former is called “persistents” and the latter is “transients”. The distinction between the persistents and transients is believed to lie mainly on the nature of the stellar companion. The persistents are mostly the low-mass BHXBs whereas the

transients are usually low-mass BHXBs. The main focus of this work is the transient systems.

1.3 Outburst mechanisms

Both the persistent and transient X-ray sources show variable X-ray activity. Therefore, a large intensity increase is not enough to deem that a source is in an outburst. Tanaka & Shibazaki (1996) employs the following criteria for the definition:

- The X-ray flux increases by more than two orders of magnitude within several days.
- The flux declines on time scales of several tens of days to more than one hundred days, and eventually returns to the pre-outburst level.
- In recurrent transients, the duration of an outburst is shorter than the quiescent period: the duty ratio over a long time span is less than unity.
- There is no fixed periodicity in the recurrence.

The outbursts are thought to be caused by a sudden dramatic increase in the mass accretion rate onto the compact object. Two competing models have been proposed to explain the outbursts: the disk instability model (see e.g. Osaki, 1974; Mineshige & Osaki, 1983) and the mass instability transfer models (see e.g. Hameury et al., 1990).

In the original disk instability model, a thermal instability in the accretion disk triggers the outburst. This thermal instability is associated with the ionization of hydrogen and helium. In the quiescence, the disk is cool and neutral. As matter accumulates in the disk, the density and the temperature increases. Hydrogen begins to ionize and hence the opacity increases. The disk becomes hotter and hotter until hydrogen is fully ionized. The disk jumps to a hot state with much higher viscosity causing a rapid increase in the mass accretion rate creating an X-ray outburst. Later, the surface density and the temperature fall until a critical density is reached where hydrogen begins to recombine. At this point the accretion disk returns to the cool state. Over years, the model has been modified to explain the observed behavior of X-ray novae (see e.g. Lasota, 2001, for the details).

In the mass instability transfer model, the surface of the companion star is considered to be X-ray illuminated by the compact object. The outer layers of the companion star expands and hence an instability occurs in the companion's atmosphere which leads to a sudden mass transfer. Consequently, the mass inflow from the outer region of the accretion disk on the compact object is suddenly enhanced, giving rise to an outburst. The outburst ends when all of the matter in the disk has been accreted on the compact object. In order for a mass transfer instability to trigger an outburst, the hard X-ray flux must exceed the intrinsic stellar flux. However, the X-ray flux in the quiescence is too low to induce this instability. Therefore, this mechanism seems to be unlikely (Tanaka & Shibazaki, 1996).

Table 1.1. Properties of BHXBs

Common Name	Spec. Type	P_{orb} (hr)	$f(M)$ (M_{\odot})	M_1 (M_{\odot})	i (deg)	Reference (dynamical)	D (kpc)	Reference (distance)
Dynamically identified BHXBs								
A0620-003	K4V	7.8	2.76 ± 0.01	6.6 ± 0.25	51.0 ± 0.09	1,2	1.06 ± 0.12	11
4U 1543-47	A2V	26.8	0.25 ± 0.01	9.4 ± 1.0	20.7 ± 1.5	3	7.5 ± 0.5	2
XTE J1550-564	G8/K8IV	37.0	7.73 ± 0.40	9.1 ± 0.6	74.7 ± 3.8	4	4.4 ± 0.5	3
GRO J1655-40	F3/F5IV	62.9	2.73 ± 0.09	6.3 ± 0.27	70.2 ± 1.9	3,5	3.2 ± 0.5	4
V4641 Sgr	B9III	67.6	3.13 ± 0.13	7.1 ± 0.3	75 ± 2	3	9.9 ± 2.4	6
V404 Cyg	K0III	155.3	6.08 ± 0.06	12 ± 2	55 ± 4	6	2.39 ± 0.14	8
GRO J0422+32	M2V	5.1	1.19 ± 0.02	3,7	2 ± 1	9,10
GRS 1009-45	K7/M0V	6.8	3.17 ± 0.12	3,8	3.82 ± 0.27	10
XTE J1118+480	K5/M0V	4.1	6.1 ± 0.3	3,9,10	1.7 ± 0.1	12
Nova Mus 91	K3/K5V	10.4	3.01 ± 0.15	3,11	5.89 ± 0.26	10
GS 1354-64	GIV	61.1	5.73 ± 0.29	12	>25	1
XTE J1650-500	K4V	7.7	2.73 ± 0.56	13	2.6 ± 0.7	13
GX 339-4	...	42.1	5.8 ± 0.5	14,15	9.0 ± 3.0	5
Nova Oph 77	K3/7V	12.5	4.86 ± 0.13	3,6	8.6 ± 2.1	14
GS 2000+251	K3/K7V	8.3	5.01 ± 0.12	3,6	2.7 ± 0.7	14
GRS 1915+105	K/MIII	739	9.5 ± 3.0	...	66 ± 2	16,17,18,19	9 ± 3	7
XTE J1859+226	...	6.58	4.5 ± 0.6	>5.42	<70	29	8 ± 3	10
IC 10 X-1	...	34.9	7.64 ± 1.26	>20	...	22,23
NGC 300-1	...	32.3	2.6 ± 0.3	>10	...	24
M33 X-7	...	82.9	0.46 ± 0.07	15.65 ± 1.45	...	25
LMC X-3	B3V	40.9	2.3 ± 0.3	26
LMC X-1	O7III	93.8	0.886 ± 0.037	10.91 ± 1.54	...	27
Cyg X-1	O9.7Iab	134.4	0.251 ± 0.007	>8	...	28	1.86 ± 0.11	16
Observationally identified BHXBs								
H 1743-322	75 ± 3	15	8.5 ± 0.8	15
MAXI J1659-152	M5V	2.414	$65-80$	31
IGR J17091-3624
XTE J1752-223
XTE J1720-318
4U 1630-47
MAXI J1543-564
MAXI J1836-194
MAXI J1910-057
Swift J1753.5-0127	...	3.24	30

Note. — Sources used in this work are highlighted with boldface font.

References. — for dynamical data: (1) Neilsen et al. (2008); (2) Cantrell et al. (2010); (3) Orosz (2003); (4) Orosz et al. (2011); (5) Greene et al. (2001); (6) Charles & Coe (2006); (7) Filippenko et al. (1995); (8) Filippenko et al. (1999); (9) McClintock et al. (2001); (10) Gelino et al. (2006); (11) Orosz et al. (1996); (12) Casares et al. (2009); (13) Orosz et al. (2004); (14) Hynes et al. (2003a); (15) Muñoz-Darias et al. (2008); (16) Greiner et al. (2001); (17) Neil et al. (2007); (18) Harlaftis & Greiner (2004); (19) Fender et al. (1999); (20) Filippenko & Chornock (2001); (21) Zurita et al. (2002); (22) Prestwich et al. (2007); (23) Silverman & Filippenko (2008); (24) Crowther et al. (2010); (25) Orosz et al. (2007); (26) Cowley (1992); (27) Orosz et al. (2009); (28) Caballero-Nieves et al. (2009); (29) Corral-Santana et al. (2011); (30) Zurita et al. (2008); (31) Kuulkers et al. (2013)

References. — for distance measurement: (1) Casares et al. (2009); (2) Özel et al. (2010); (3) Orosz et al. (2011); (4) Hjellming & Rupen (1995); (5) Hynes et al. (2004); (6) Orosz et al. (2001); (7) Fender et al. (1999); (8) Miller-Jones et al. (2009); (9) Webb et al. (2000); (10) Hynes (2005); (11) Cantrell et al. (2010); (12) Gelino et al. (2006); (13) Homan et al. (2006); (14) Barret et al. (1996); (15) Steiner et al. (2012); (16) Reid et al. (2011)

1.4 Observational properties of black hole X-ray binaries

Black hole X-ray binaries are classified into distinct emission states and often observed to show state transitions. These states can be distinguished by their X-ray spectra and short term X-ray variability, and also by radio emission. The variability is often described in terms of power spectral density. It will be described in detail in Section 2.2. Overviews presenting the phenomenology of the black hole states can be found in Remillard & McClintock (2006) and Belloni (2010). Here, I summarize the observed properties of black hole X-ray binaries and introduce the basic physical components that are believed to be responsible for the different emission states.

1.4.1 X-ray states

The emission states are built up on two different X-ray emission components: a soft thermal radiation in the form of a combination of black bodies at different temperatures (Mitsuda et al., 1984) and a harder component showing a power-law spectrum. The soft and hard components dominate the soft and the hard states, respectively. In this regard, the soft and the hard states are the main black hole states. The aperiodic short term X-ray variability on timescales of 0.001s to 1000s correlates with the main states. The hard state shows strong variability whereas the soft state shows weak or no variability. See Figure 1.1 for the energy and power spectra of the hard and the soft states.

The thermal component is believed to originate from an optically thick, geometrically thin standard accretion disk (Shakura & Sunyaev, 1973). The power-law component, on the other hand, is believed to originate from an optically thin, hot plasma (corona or ADAF). It can be physically modelled by thermal Comptonization of cold seed photons ($kT_{seed} \sim 1$ keV) in a hot electron plasma ($kT_e \sim 100$ keV) which the seed photons are believed to originate from the accretion disk (see Gilfanov, 2010, for a review of the Comptonization). Alternatively, recent observations show that the X-ray radiation at lower luminosities ($10^{-3} < L_{Edd} < 10^{-4}$) may also be dominated by the jet synchrotron emission (Russell et al., 2010, 2012).

Both the persistent and transient sources may show the main states. For black hole transients, the evolution of states is coupled to the evolution of the outburst. The hard state is found at the beginning and the end of the outburst whereas the soft state is found at the middle of the outburst. In addition to the main states, there also exist two transitional states: the hard- and the soft-intermediate states (Belloni, 2010). In these states, the X-ray spectral and temporal properties are not suited to the main states, but present the properties of a mixture of the main states. More importantly, their identification depends on the identification of some quasi-periodic oscillations (QPO) seen in the power spectrum.

Hardness-intensity (HID) and hardness-rms (HRD) diagrams are two useful tools that aid to characterize the general behavior of black hole transients (Belloni, 2010). The four spectral states are shown in a graphical illustration in Figure 1.2. The four states are observed regularly in black hole transients, starting from the hard state with increasing flux, crossing the HIMS and the SIMS and reaching the soft state. After spending some time in the soft state, the flux starts to decrease. At some point, a reverse transition takes place, the path is followed backwards to the hard state and then to the quiescence. While the majority of the outburst decays follow this standard evolution, a number of outburst

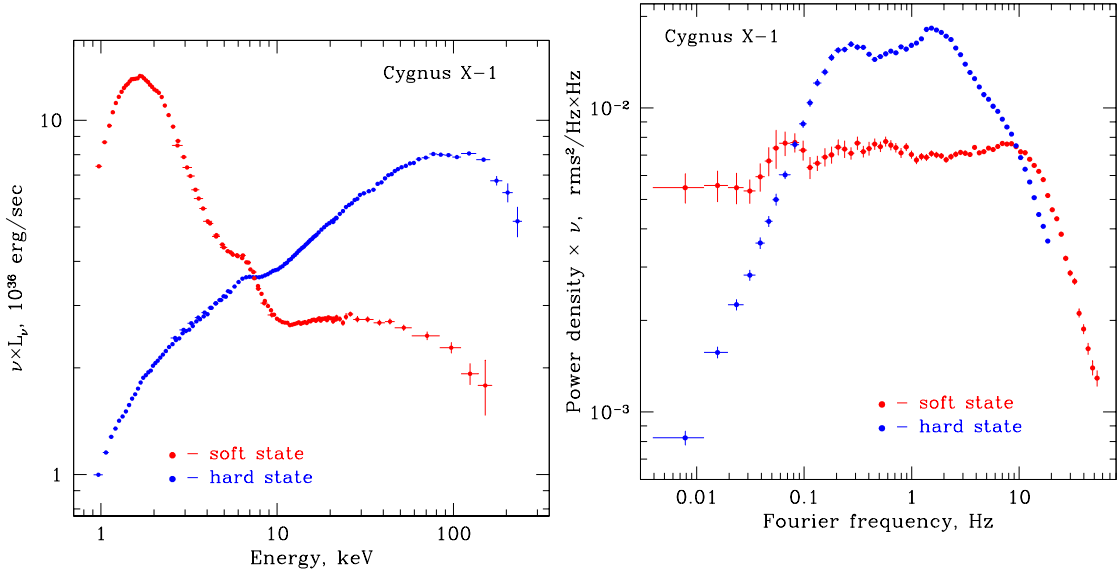


Figure 1.1 Energy and power spectra of the hard and the soft states of a black hole Cyg X–1. Adapted from Gilfanov (2010).

decay are observed to return quiescence before reaching the soft state. These outbursts are called the “failed” outbursts. The duration of a cycle in the HID is about months to years within the detection limits of *RXTE*/PCA and varies from source to source and also from outburst to outburst. A recent study shows that the rise of the outbursts and the transitions happen faster than the middle and the final decay part of the outbursts (Dunn et al., 2010).

In the following, the main characteristics of the black hole states are highlighted. **Hard state:** This state is associated with the vertical branch in the HID. It is phenomenologically characterized by a hard, power-law dominated energy spectrum with a typical photon index of 1.5–1.8 in the 3–25 keV band. A thermal disk component is usually not present in the X-ray spectrum as the inner disk temperature is below when looked at with *RXTE* instrument. Hard state has strong variability with integrated fractional rms amplitudes of ~ 30 – 45% . Its PSD can be decomposed in a number of Lorentzian components. As the flux increases, the integrated variability decrease and the peak frequencies of the Lorentzians increase. One of the Lorentzian components can take the form of a type-C QPO.

Hard–intermediate state (HIMS): The energy spectra in the hard–intermediate state is softer than in the hard state with a steeper power–law (with a photon index of up to ~ 2.5) and a thermal disk component. The hard–intermediate state describes a portion of the horizontal branch in the HID. During a transition from the soft-to-hard, the photon index decreases and the disk fraction decreases. The power spectrum in the hard–intermediate state has a lower fractional rms amplitude (10–20%) than in the hard state and shows a clear type-C QPO with a peak frequency that evolves with hardness.

Soft–intermediate state (SIMS): The spectrum in this state is slightly softer than that in the hard–intermediate state and the PSDs show very different timing properties. The fractional rms amplitude of variability is as low as a few %. A QPO of either type-A or

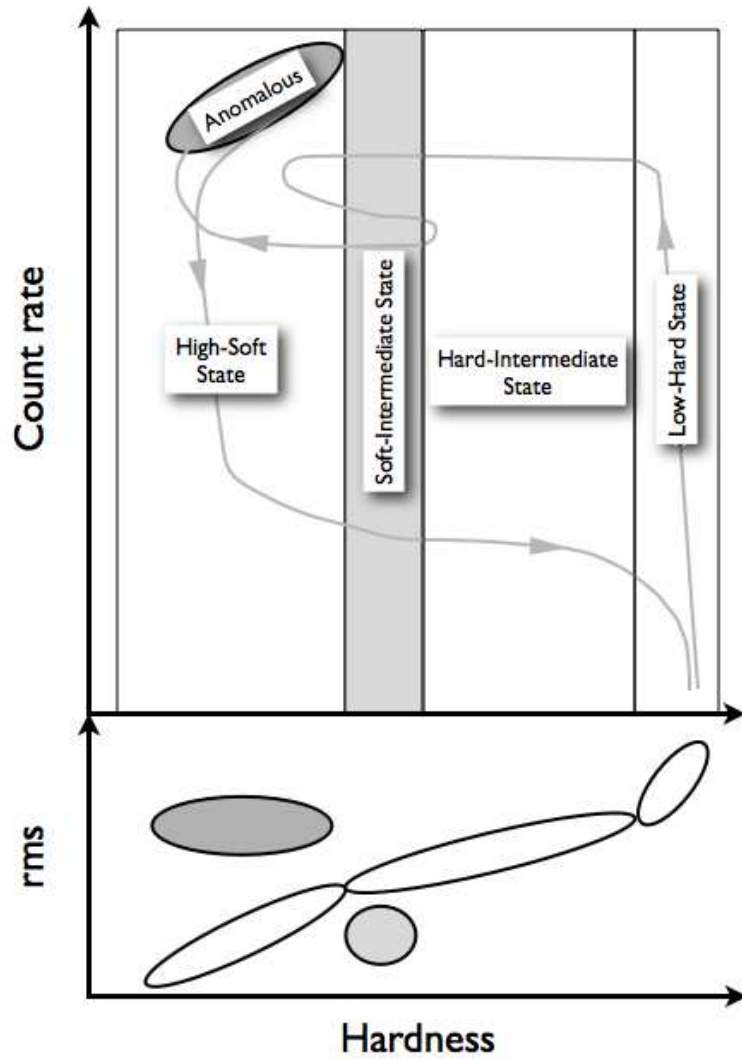


Figure 1.2 Sketch of the general behavior of a black hole X-ray binary in the HID (top) and HRD (bottom), with the HID regions corresponding to the X-ray states. The sketch is taken from Belloni (2010).

of type-B is often present.

Soft state: This state is dominated by a soft thermal disk component with small contribution to the total flux from a power-law component. Variability is weak, down to 1% fractional rms amplitudes, and weak QPOs are sometimes detected in the 10–30 Hz range.

Quiescent state: It is thought to be an extension of the hard state at lower luminosities and its separation from the hard state depends mostly on the detection capability of the X-ray instruments. The spectrum in this state is usually modelled with a power-law. Observations of some sources in this state show a softer X-ray spectrum compared to that of in the hard state (Plotkin et al., 2013).

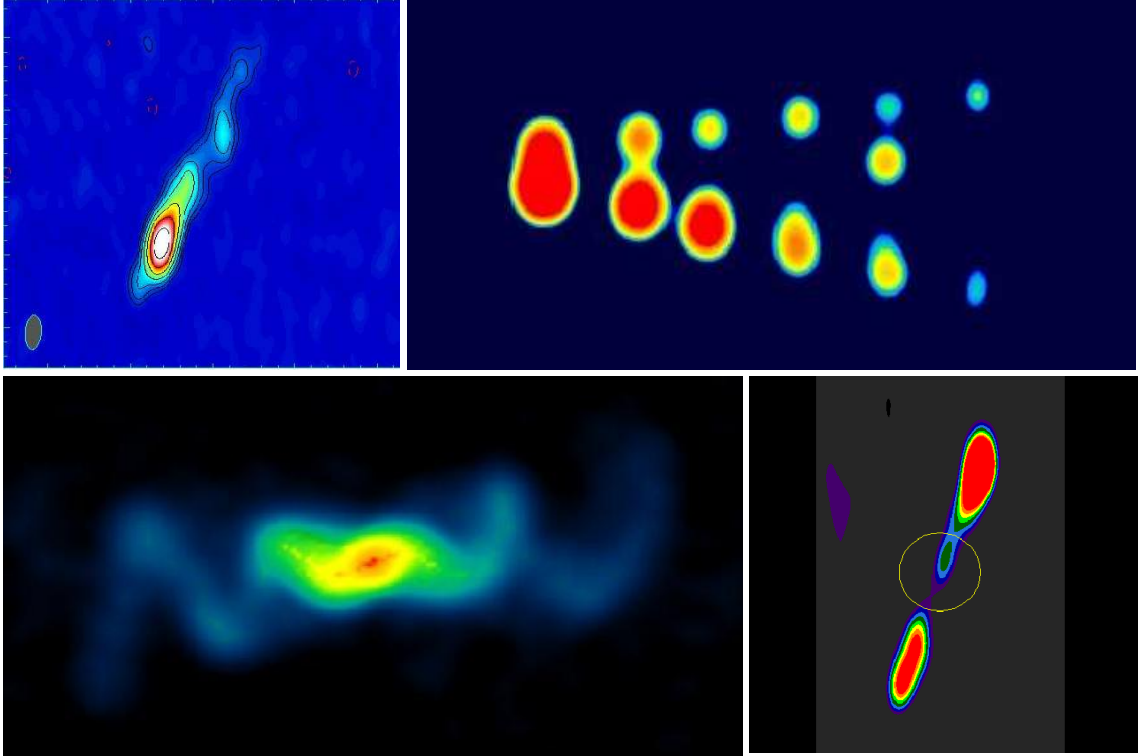


Figure 1.3 Jets resolved in radio images of black hole systems. Top left: milliarc-scale, steady jet from HMXB Cyg X–1. Top right: transient arcsec-scale radio jet from a black hole transient GRS 1915+105, Bottom left: arcsec-scale radio jet from the first Galactic radio source discovered: SS 433. The binary orbit is almost edge-on. Bottom right: fossil, arcmin-scale radio jets around a Galactic center black hole in 1E 140.7–2942. The figure is taken from Gallo (2010).

1.4.2 Multiwavelength emission properties

1.4.2.1 Radio

The radio emission from X-ray binaries is thought to be synchrotron in nature. It is inferred by the non-thermal spectra and high brightness temperatures. The hard state is associated with a flat or slightly inverted radio spectrum ($S_\nu \propto \nu^\alpha$ with $\alpha \sim 0$). In analogy with those observed in active galactic nuclei, the flat spectra are interpreted as a self-absorbed synchrotron emission from steady, collimated, compact jets (Blandford & Konigl, 1979; Hjellming & Johnston, 1988). The high resolution radio maps have confirmed the jet interpretation of BHXBs in the hard state (see Figure 1.3). The soft state, on the contrary, is not associated with a flat radio spectrum, the core radio fluxes drop by a factor of at least 50 compared to the hard state (Fender et al. 1999; Russell et al. 2011; see also Fig. fig:radioevolstates). This is generally interpreted as the physical suppression of the jet. Any radio emission in this regime, if present, is attributed to the optically thin synchrotron emission (Corbel et al., 2004; Fender et al., 2004). The transition from HIMS to SIMS is associated with the bright, optically thin ($\alpha < 0$), short lived radio flares.

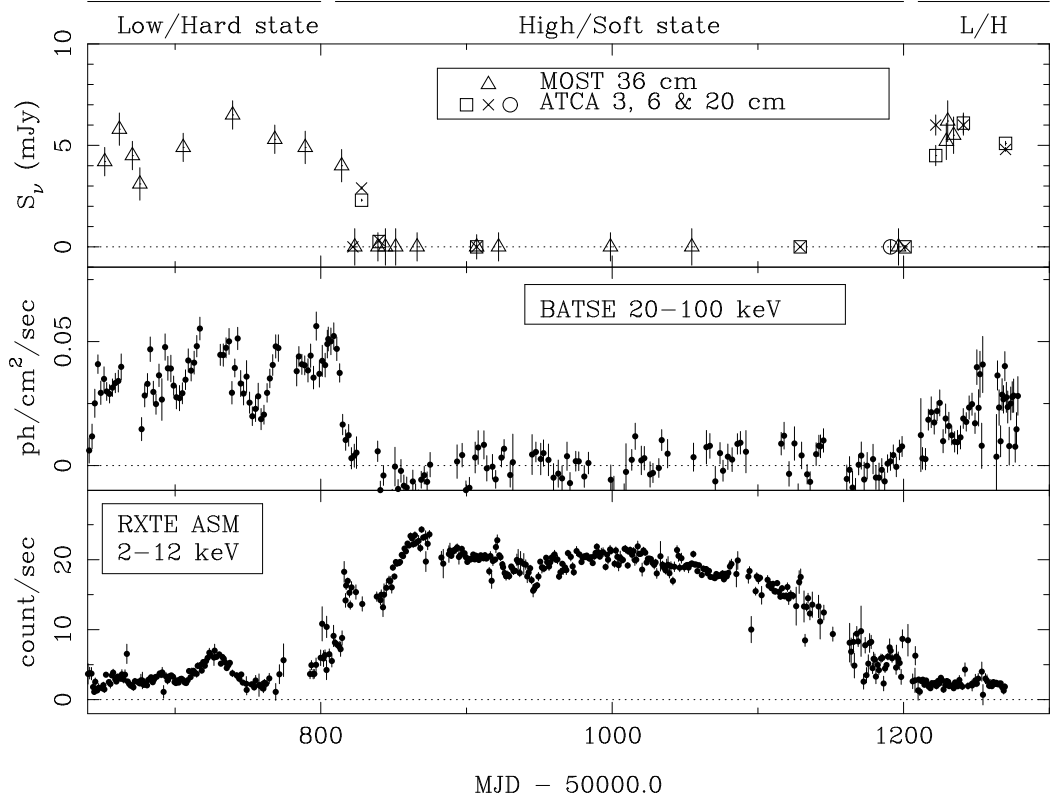


Figure 1.4 Radio, hard and soft X-ray monitoring of GX 339-4 during its outburst in 1997/1998. The radio emission in the soft state is lower than that of in the hard state by a factor of 25. The figure is taken from Fender et al. (1999).

1.4.2.2 Optical and infrared

The optical and infrared (OIR) radiation from black hole X-ray binaries (BHXBs) may have contributions from a number of components of the system. In high-mass BHXBs, the OIR emission is dominated by the massive stellar-companion in the system (van den Heuvel & Heise, 1972). In low-mass BHXBs, the OIR emission is expected from outer parts of the disk, the jet and the companion star (Russell et al., 2006). There is now a lot of effort on disentangling the emission from these components (Russell et al., 2010).

The OIR light curves show similar behavior to the radio evolution. During the transition from the hard to soft state, the OIR light curves show a sharp drop (Homan et al., 2005a), and during the decay they show a brightening. In terms of X-ray spectral properties, this brightening happens when the source is fully back in the hard state with its X-ray spectrum close to its hardest (Kalemci et al. 2005; Buxton et al. 2012; see also Chapter 3). The OIR SEDs of the excess emission taken during the brightening show a spectral slope of $\alpha \sim -0.6$ at a few mJy for some sources (Kalemci et al., 2005; Russell et al., 2010). This negative slope cannot be explained with a disk origin, but is rather consistent with the optically thin jet synchrotron emission. When all this information is put together, the jets are thought to be contributing to the OIR emission.

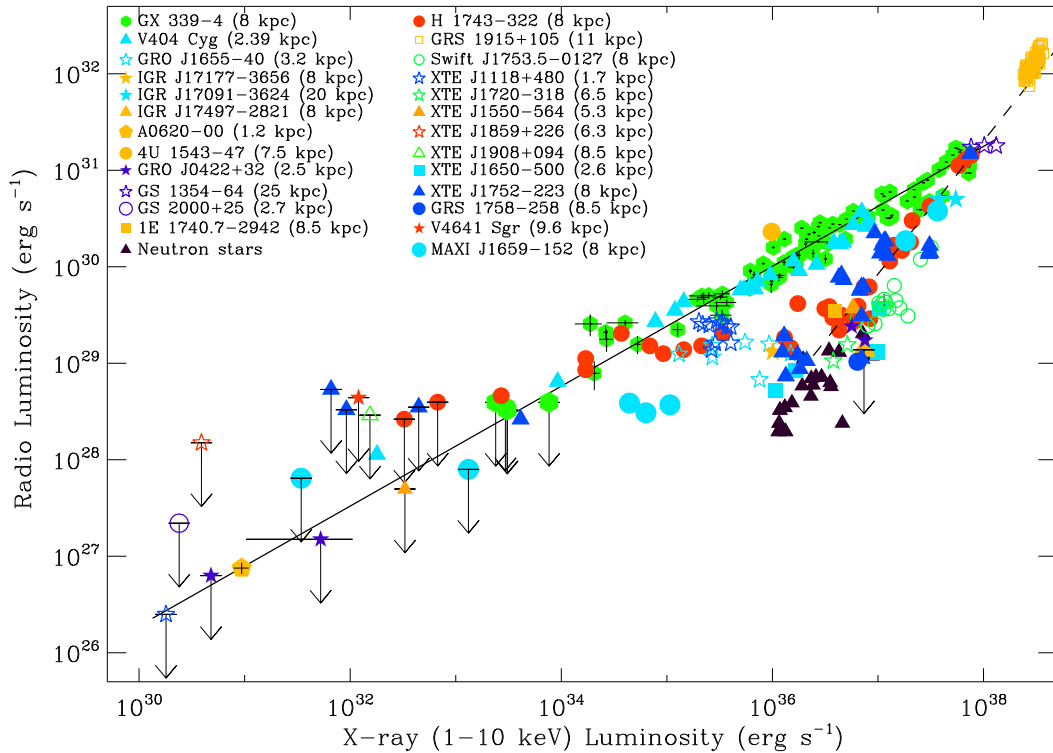


Figure 1.5 Radio and X-ray luminosities for Galactic accreting black hole binaries during the hard and quiescent states (Corbel et al., 2013a). It illustrates the distinction between the standard and the outliers track.

1.4.2.3 Radio–X-ray luminosity relation

In the last decade, a strong relationship was established between the X-ray and radio emission of BHXBs during the hard state (Hannikainen et al., 1998; Corbel et al., 2000, 2003; Gallo et al., 2003b; Corbel et al., 2008). The relationship takes the form of a non-linear power-law luminosity correlation, $L_{Rad} \propto L_X^b$, where L_{Rad} is the radio luminosity, L_X the X-ray luminosity and b is $\approx 0.5-0.7$. Such a relationship was interpreted as a strong connection between the accretion flow (standard disk, corona, or ADAF) and the compact jets, and gained universality as this radio/X-ray correlation has been extended to active galactic nuclei with an additional dependence on the mass of the black hole (Merloni et al., 2003; Falcke et al., 2004; K rding et al., 2006a). The non-linearity of the relation led to the hypothesis that the total power output of quiescent BHXBs could be dominated by radiatively inefficient outflow, rather than by the local dissipation of gravitational energy in the accretion flow (Fender et al., 2003; K rding et al., 2006b).

However, in the following years, in addition to existing relationship, many outliers are found to lie well outside the standard correlation (Corbel et al., 2004; Rodriguez et al., 2007; Soleri et al., 2010), creating a second correlation track¹ with $b = 0.98 \pm 0.08$ (Gallo et al., 2012). For a given luminosity, the ‘outliers’ track exhibit a fainter radio luminosity

¹In the literature, the reported values of the power-law index, b , show slight variations depending on the source analyzed.

compared to those of ‘standard’ track (see Fig. 1.5). In addition to this dual track behavior, some sources show transition from outliers track to the standard track below a critical X-ray luminosity $L_{3-100\text{keV}} \approx 5 \times 10^{-3} L_{Edd}$ (Coriat et al., 2009; Ratti et al., 2012). This picture of the radio-X-ray luminosity relation challenges our current understanding of the inflow/outflow connection.

Some recent studies have focused on understanding the reasons that can cause to the dual tracks. Coriat et al. (2011) demonstrated that the difference between the tracks may be due to the radiative efficiency of the accretion flows. While radiatively inefficient flows are consistent with the standard track, radiatively efficient flows are consistent with the outliers track. These results are obtained from combination of theoretical scalings of the jet and the accretion flow models. Another possibility is that the radio luminosity may be directly related to the jet power, therefore any difference in the binary parameters of the sources may result in different jet powers for a given X-ray luminosity. Soleri & Fender (2011) investigated such a possibility, but they could not produce the observed relations.

1.4.3 Accretion-ejection models and multiwavelength emission mechanisms

The phenomenology and the basic accretion-ejection components described in the previous section are well established. In the following, I give a brief summary of the accretion-ejection models and emission mechanisms that are presently discussed to explain the phenomenology. This summary is intended to provide a basis to interpret the results presented in Chapter 3 through 6.

1.4.3.1 Standard α accretion disk model

Shakura & Sunyaev (1973) proposed a fundamental theory of accretion disk known as the standard accretion disk model or simply the α disk model. The model considers a geometrically thin and optically thick disk that rotates around the black hole with Keplerian angular velocity. The height of the disk is in equilibrium by the pressure p of the disk against the vertical component of the gravity. The matter in the disk gradually moves inward due to viscous stress. In the model, the matter in the disk is turbulent and the turbulent viscous stress tensor is parametrized by the disk pressure: $t_{\alpha\phi} = \alpha p$, where α is the viscosity parameter. The α parameter has not been computed in detail. Comparison between observations and the model indicate a value between 0.1-1 (Shapiro & Teukolsky, 1983).

The radiation from an optically thick, geometrically thin disk is in the form a multi-color black body (Mitsuda et al., 1984). Each annulus of the disk radiates as a black body of temperature with temperature distribution of $T \sim r^{-3/4}$. The temperature of the disk increases toward the compact object and makes a peak at ~ 1 keV in XBs. For frequencies $\nu \ll kT(R_{out})/h$, the black body function takes the Rayleigh jeans form; hence the flux density scales as $F_\nu \propto \nu^2$. This emission comes from the outer parts of the disk. For intermediate frequencies, the flux density scales as $F_\nu \propto \nu^{1/3}$. For frequencies $\nu \gg kT(R_{out})/h$ the black body function takes the Wien form; hence the flux density scales as $F_\nu \propto 2h\nu^3 c^{-2} e^{-h\nu/kT}$. This corresponds to the hottest part of the disk, the inner regions of the disk.

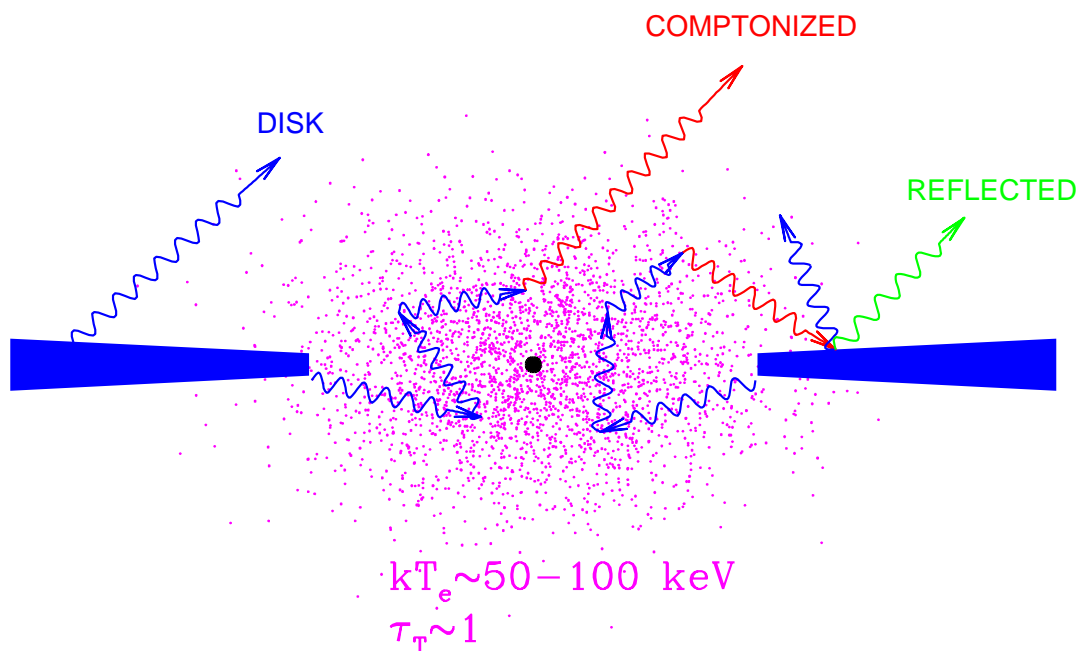


Figure 1.6 The main components of the X-ray emission from an accreting black hole (left) and a plausible geometry of the accretion flow in the hard state (right). Adapted from Gilfanov (2010).

1.4.3.2 Corona

The standard accretion disk model is inadequate in describing the hard X-ray emission in the spectra in the power-law form. A plausible mechanism that can produce this hard spectral component is the Comptonization of soft photons on hot electrons in the vicinity of the compact object (Sunyaev & Truemper, 1979; Sunyaev & Titarchuk, 1980). This mechanism successfully explains the observed luminosity and the overall spectral energy distribution observed in the hard X-ray band.

The Comptonization site is often referred to as a corona. It is essentially a cloud of hot thermal or non-thermal electrons. There are strong uncertainties regarding the geometry of the corona. A commonly considered geometry is the sombrero configuration (see Figure 1.6). In this configuration, it is assumed that outside some truncation radius the accretion takes place predominantly in accordance with the standard disk model whereas closer to the compact object the accretion disk is transformed into a hot optically thin and geometrically thick flow. There is no commonly accepted mechanism of the truncation of the disk and formation of the corona. The most promising is the evaporation of the accretion disk under the effect of the heat conduction (Meyer & Meyer-Hofmeister, 1994; Meyer et al., 2000). Such a configuration provides a physically motivated picture describing the formation of the corona and destruction of the optically thick disk.

The accretion disk and the corona forms a complex system. Since some regions of the

corona are in contact with the accretion disk, there will be interactions between the two components such as the reflection of the hard X-ray photons (e.g. Comptonized photons) from the accretion disk. In the following, I discuss the Comptonization and the reflection processes.

Comptonization The elastic scattering of the electromagnetic radiation from the free charged particles is known as the Thomson scattering. It is only valid as long as the photon energies are much less than the mass energy of the electrons ($h\nu \ll mc^2$). In this process, the incident photons are approximated as continuous electromagnetic waves which then induce dipole radiation from an oscillating electron in all directions. The differential Thomson cross-section for unpolarized incident radiation at angle θ is given by:

$$\frac{d\sigma_T}{d\Omega} = \frac{1}{2}r_0^2(1 + \cos^2\theta) \quad (1.7)$$

where $r_0 = \frac{e^2}{m_e c^2}$ is the classical electron radius. The total cross-section σ_T for electrons with charge e can be obtained by integrating the differential-cross section over all scattering angles:

$$\sigma_T = \frac{8\pi}{3}r_0^2 = 6.652 \times 10^{-25} \text{cm}^2 \quad (1.8)$$

Note that σ_T is inversely proportional to m_e^2 . So, the cross-section for the protons are smaller than that for the electrons by a factor of $(m_e/m_p)^2 \sim 10^{-7}$. This makes the scattering negligible for particles other than electrons.

The inelastic scattering of photons from free charged particles are known as the Compton scattering. In a simple Compton scattering process, a photon of energy E collides with an electron at rest, transfers kinetic energy to the electron while reducing its own energy to E' , which is given by:

$$E' = \frac{E}{1 + \frac{E}{m_e c^2}(1 - \cos\theta)} \quad (1.9)$$

The differential cross section for this process is given by Klein-Nishina formula which takes into account the quantum electrodynamical effects:

$$\frac{d\sigma_{KN}}{d\Omega} = \frac{3}{16\pi}\sigma_T \left(\frac{E'^2}{E}\right) \left(\frac{E}{E'} + \frac{E'}{E} - \sin^2\theta\right) \quad (1.10)$$

When $E = E'$, this reduces to the classical expression given in equation 1.7. The total cross section can be obtained by integrating the Klein-Nishina formula over all scattering angles (see e.g. Rybicki & Lightman, 1979). For high photon energies, the Klein-Nishina cross-section is reduced and hence the Compton scattering becomes less efficient.

In astronomical sources, the electrons are not at rest but can be in thermal motion. They are assumed to have a relativistic Maxwellian velocity distribution with a characteristic temperature T_e :

$$N(\gamma) \sim \gamma^2 \beta \exp(-\gamma m_e c^2 / kT_e) \quad (1.11)$$

where $\beta = v_e/c$ is the electron velocity, and $\gamma = (1 - \beta^2)^{-1/2}$ is the Lorentz factor. In this process, if the incident photons have lower energy than the electrons, on average they gain energy from the electrons through Compton collisions. Due to the Maxwellian distribution, this process is called thermal Comptonization.

The average fractional energy loss of an incident photon, per collision, is given by:

$$\left\langle \frac{\Delta E}{E} \right\rangle = -\frac{E}{m_e c^2} \quad (1.12)$$

This is obtained by averaging the equation 1.9 over all scattering angles. In addition, the average energy gain by the photon from an electron with $kT_e < m_e c^2$ is $4kT_e/m_e c^2$ (Rybicki & Lightman, 1979). When this is combined with the equation 1.12, the mean fractional energy change of the photons, per collision, is

$$\left\langle \frac{\Delta E}{E} \right\rangle = \frac{4kT_e - E}{m_e c^2} \quad (1.13)$$

The expression states that the photons, on average, gain energy as long as $E < 4kT_e$. Moreover, the electrons will cool unless energy is deposited into them by other processes.

An important parameter is the approximate fractional total energy change for a photon which traverses a Comptonizing plasma of optical depth τ_e . It can be determined by multiplying the average fractional energy gain and the average number of scatterings. The standard random-walk arguments dictate that the average number of scatterings is $\max(\tau, \tau^2)$. Hence the total fractional energy change is given by:

$$y = \frac{4kT_e}{m_e c^2} \max(\tau, \tau^2) \quad (1.14)$$

which is called the Compton ‘‘y-parameter’’.

The Compton spectrum emerging from repeated scatterings requires a solution of the Kompaneets equation (Rybicki & Lightman, 1979). The equation describes the evolution of the photon distribution function due to repeated inverse Compton scattering. General solutions to the Kompaneets equation are analytically complex and mostly calculated numerically (e.g. Sunyaev & Titarchuk, 1980). For energies where $y \ll 1$, only Thomson scattering is important and the initial soft photon spectrum will not be modified. For $y \gg 1$, the spectrum is saturated due to a competition between the Compton scattering higher energy photons and the inverse Compton scattering of lower energy photons. This competition thermalizes the spectrum to a cloud temperature T_e and at higher energies the spectrum becomes a Wien law.

For $y \gtrsim 1$, only the high energy part of the spectrum saturates to the Wien law. For escaped photons of intermediate energies, the spectrum takes a power-law form.

Reflection When a cold material is irradiated by hard X-rays it produces backscattered radiation, fluorescence, recombination and other emissions. All these constitute the reflection spectrum and depends on the surface composition of the material. In astrophysical situations, the cold material is often the accretion flow or the surface of the star.

The most notable features of the reflection spectrum are the fluorescence iron K_α line at 6.4–7 keV, a Compton hump at ~ 30 keV, and K_α absorption edges as shown in Figure 1.7. The Compton hump is produced due to photoabsorption and Compton

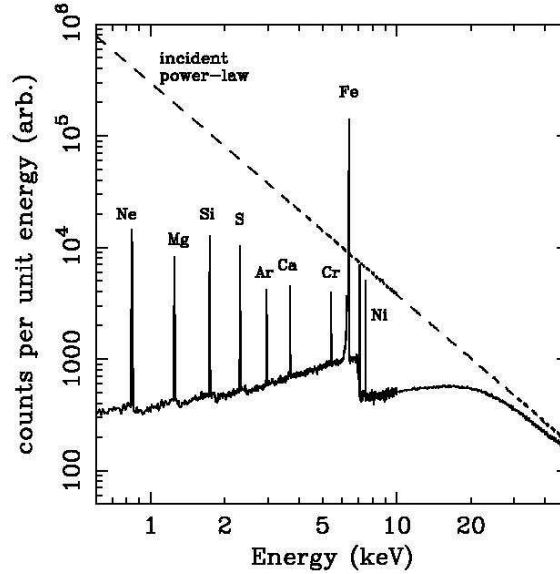


Figure 1.7 The reflection spectrum obtained by an incident power-law spectrum with a photon index $\Gamma = 2$ (dashed line) on a cold neutral slab of matter with cosmic abundances (Reynolds, 1996).

scattering processes. The soft energy photons (~ 15 keV) will be predominantly absorbed in the cold medium whereas hard energy photons (> 15 keV) will be mostly Compton scattered until they escape the system or are photoabsorbed. The absorption edges are due to discontinuities in the photoelectric cross-section. The particular shape and the amplitude of the reflection features depend on the geometry of the primary source and the reprocessing medium and the abundance of heavy elements. Also, it is affected by the ionization and proper motion of the reflector and general relativistic effects. For a detailed review of the reflection phenomena see Fabian & Ross (2010).

The modeling of this component led to very important correlation between the disk solid angle and the spectral index. A comparison of this correlation for BHXBs and NSXBs is studied in Chapter 6.

1.4.3.3 Advection dominated accretion flow

Since the standard disk model was not able to explain the hard X-rays observed in low rate accreting sources, the ADAF model was proposed (Esin et al., 1996). The ADAF model assumes that the inner region of the standard disk close to the compact object is replaced by an hot accretion flow. Most of the energy stored in the inner hot flow is advected into the black hole and only a small portion of the energy is radiated away. Therefore, the radiative efficiency is lower than that of the standard disk model.

An ADAF may be present in two regimes, depending mainly on the accretion rate and the optical depth. In the first regime, defined as “the slim accretion disk”, the accretion rate is high and the optical depth becomes very high; the radiation is trapped in the accretion disk (Abramowicz et al., 1988). In the second regime, the accretion rate is low and the accretion flow is optically thin; the gas is unable to radiate its heat energy in less than accretion time (Narayan & Yi, 1994).

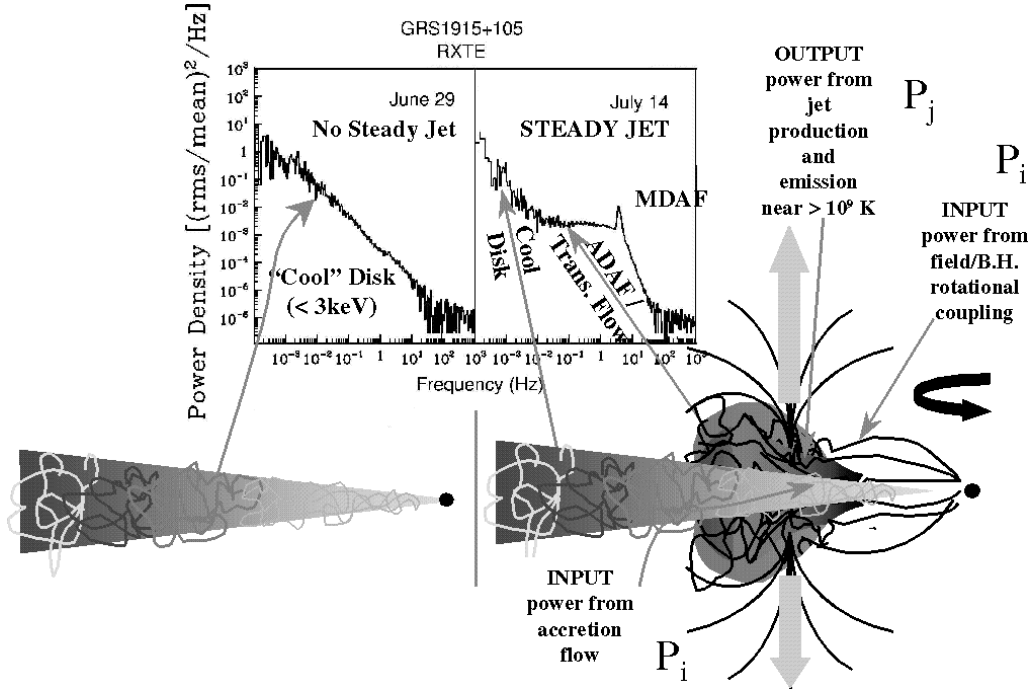


Figure 1.8 Schematic diagram of the MDAF model for the BHXB GRS 1915+105. In the soft state, a cool disk is associated with the power spectrum when no jet is produced (left). In the hard state, not only an ADAF is required but an MDAF to produce the few Hz cutoff and the QPO, and an outward facing magnetosphere to produce the jet. Figure is taken from Meier (2005).

Over the years, the original ADAF model has been modified and led to development of a quite number of sub classes. For instance, in the ADIOS (advection dominated inflow-outflow solution) the advected energy is transported outward in the form of an outflow (Blandford & Begelman, 1999), in CDAF (convection dominated accretion flow) the convection transports angular momentum toward the inner part of the flow (Quataert & Gruzinov, 2000), in luminous hot accretion flow (LHAF) the efficiency of the accretion flow is higher (Yuan, 2001). We discuss a special case of ADAF model below since we test its predictions in this work.

1.4.3.4 Magnetically dominated accretion flow

Meier (2012) suggests that at low accretion rates (where ADAF can occur), the accretion flow inside a radius $R \sim 100R_g = 100 GM/c^2$ should develop a black hole magnetosphere in a structure similar to the ones studied in Tomimatsu & Takahashi (2001); Uzdensky (2004). In this picture, the closed magnetic field lines connecting the disk at R with the event horizon could channel the accretion flow toward the black hole, creating a magnetically dominated accretion flow (MDAF). Open field lines anchored at R , on the other hand, could create magneto-hydrodynamic jets or winds.

The suggested mechanism for MDAF formation is radiative cooling of the accretion flow. Cooling lowers the plasma pressure and decreases the disk vertical scale height. Both leads to a dramatic increase in the dominance of magnetic stresses over the thermal

and radiation pressure.

MDAF is an inefficient flow. It is a nearly-radial, in-spiral geometrically thick flow because of magnetic pressure. The majority of the gravitational energy released is converted into radial inflow kinetic energy, not heat.

This model has some potential features that can explain the observed accretion-ejection properties of BHXBs (Meier, 2005, 2012).

- The flow may break up into inhomogeneous spokes and consequently this may produce low-frequency QPOs for $10M_{\odot}$ black hole. So a signature of an MDAF can be the presence of a QPO.
- In MDAF, the MRI turbulence is shut off and the inflow is laminar along strong magnetic fields. Therefore, the power-spectra is expected to show a cut-off at higher frequencies.
- In the MDAF state, the jets are launched through the open magnetic fields located at $\sim 100R_g$. The jet power decreases as the this radius increases. If some sources enters to an MDAF state, this can explain the lower radio luminosity of some sources at a given X-ray luminosity.
- The model predicts a semi-empirical, semi-theoretical relation between the QPO frequency and the X-ray luminosity. The scaling between the parameters is $\nu_{QPO} \propto L_X^{1.1}$.

Figure 1.8 shows an illustration of the geometrical configuration of the MDAF model and its correspondance to the observed X-ray temporal properties.

1.4.3.5 Standard canonical jet emission model

The standard canonical jet emission model is proposed by Blandford & Konigl (1979). An illustration of the spectrum is shown in Figure 1.9. In this model, the observed flat or slightly inverted radio spectrum is explained with self-absorbed synchrotron emission of relativistic electrons. The overall radio spectrum is built up from emission from different regions in a self-absorbed jet. Each region of the jet contributes roughly the same spectral shape, with peak flux occurring lower in frequency the further out in the jet it originates. The flat radio spectrum extends up to a spectral break after which only the optically thin portion of the synchrotron self-absorption emission from the closest region to the black hole takes place. This spectral break is important in the sense that it is directly related to the jet properties such as the jet power, magnetic field strength at the jet base and radius of the jet base. Some recent works focus on the measurement of the spectral break to constrain the jet power and its relation to the accretion power (e.g. Gandhi et al., 2011; Russell et al., 2013).

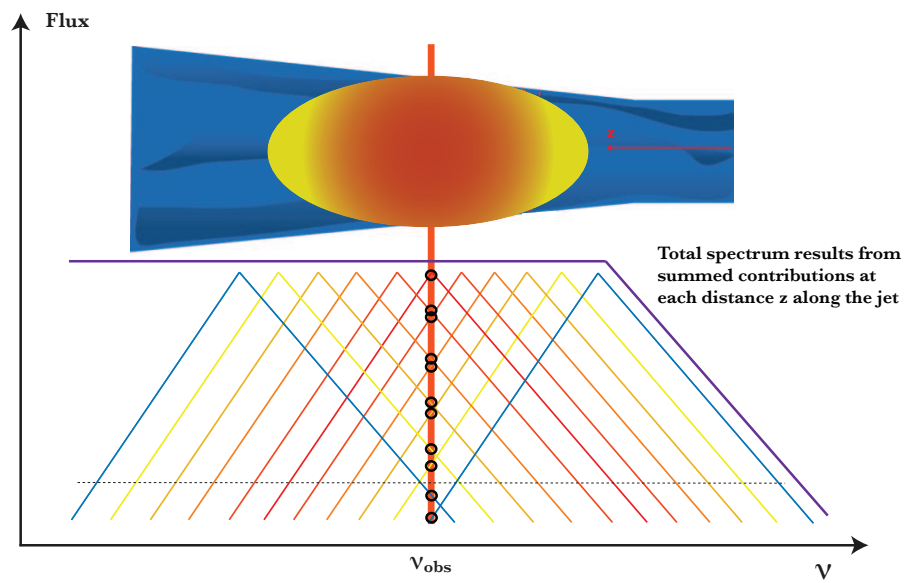


Figure 1.9 Spectrum from a standard canonical jet emission model. Each segment of the jet contributes approximately the same peaked, self-absorbed spectrum. Figure is taken from (Markoff, 2010).

CHAPTER 2

X-ray instruments and data analysis

2.1 X-ray instruments

2.1.1 The Rossi X-ray Timing Explorer

The Rossi X-ray Timing Explorer (*RXTE*) was launched on 1995 December 30 from NASA's Kennedy Space Center on a Delta II rocket. It was placed into a circular 580 km low-Earth orbit which has decayed during 10 years to about 490 km. The inclination of the orbit was 23° . After serving many fields of the X-ray astronomy, the *RXTE* was decommissioned on 2012 January 5.

The *RXTE* was an advantageous space telescope with its maneuverability so that it was able to respond quickly to the transient sources. With its large area sub-millisecond timing capability and broad spectral band (2–250 keV), it supported many multiwavelength and multimission observing programs. Therefore, the *RXTE* has been an ideal instrument for studying the black holes.

Figure 2.1 shows a schematic view of the *RXTE*. The spacecraft carries three instruments: the All Sky Monitor (ASM), Proportional Counter Array (PCA), and High Energy X-ray Timing Experiment (HEXTE). Unlike the current generation of X-ray telescopes, such as *Chandra X-ray Observatory*, *XMM-Newton* and *NuStar*, the *RXTE* does not have focusing capabilities. Instead the instruments consist of a mechanical collimators yielding a 1° square field of the view. The source density is low at these energies, so the source contamination other than X-ray background is rarely a problem.

Observations in the lower energy part (2–60 keV) are executed by the PCA, while the higher energy part (15–250 keV) are taken over by the HEXTE. The PCA (Jahoda et al., 1996) consists of five nearly identical Xenon Proportional Counter Units (PCUs). It has an energy resolution of 18% at 6 keV and a maximum timing resolution of $1 \mu\text{s}$. The HEXTE consists of two clusters (A and B) of four NaI(Tl)/CsI(Na)-Phoswich scintillation counters with an energy resolution of 16% at 60 keV and a maximum time sampling of $8 \mu\text{s}$. A detailed description of the HEXTE can be found in Rothschild et al. (1998). The ASM (Levine et al., 1996) consists of three Scanning Shadow Cameras, each contains a position-sensitive proportional counter. It was able to scan 80% of the sky every 90 minutes in 2–12 keV energy band. Therefore, it was very useful for detecting new transients or new outbursts of known transients, allowing to trigger follow-up observations. In this thesis, I used only PCA data from the *RXTE* for spectral and temporal analysis.

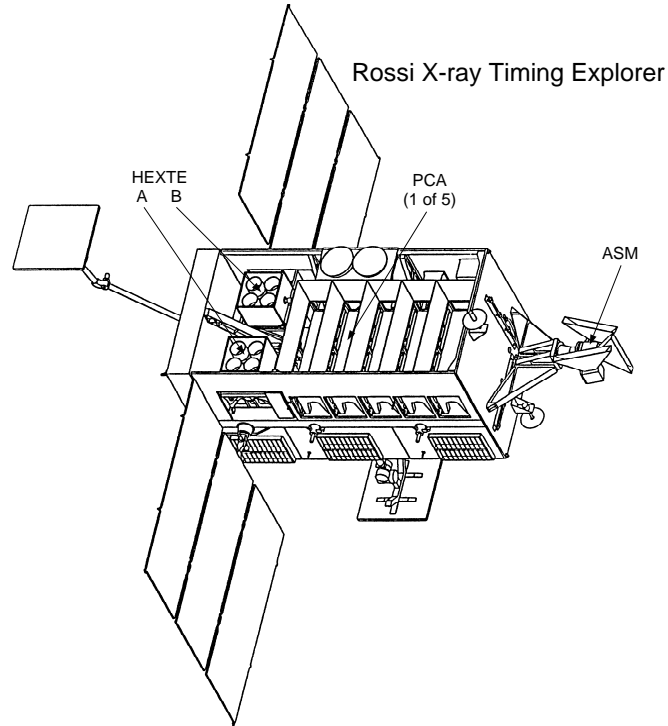


Figure 2.1 Schematic of the *RXTE* spacecraft, with the scientific instruments labeled: ASM, PCA, HEXTE.

2.1.2 Swift X-ray telescope

Swift was launched on 2004 November 20 from NASA's Kennedy Space Center on a Delta II rocket. It was placed into a nearly circular low-Earth orbit with an altitude of 586x601 km and an inclination of 20°.

It is specifically designed to study the Gamma-ray Bursts and their after glow with the three instruments on board: Burst Array Telescope (BAT) operating in the soft gamma-ray domain, the X-ray telescope (XRT) and the Ultraviolet/Optical telescope (UVOT). See Figure 2.2 for an illustration of the satellite.

The XRT consists of a grazing incidence Wolter I telescope with an X-ray CCD imaging spectrometer at the focal plane of a 3.5 m focal length. It has an effective area of 110 cm^2 , 23.6 arcmin field of view and 15 arcsec resolution. The XRT provides energy spectra in 0.2-10 keV range with a resolution of ~ 140 eV at 6 keV (during the launch), and light curves with resolution at least 50 ms.

The BAT is a large field of view, coded-aperture instrument with a CdZnTe detector plane designed to monitor a large fraction of the sky and an effective area of 5,240 cm^2 . It is sensitive to soft Gamma-rays in 15-150 keV energy range with a resolution of ~ 7 keV.

The UVOT uses a modified 30 cm aperture Ritchey-Chretien telescope. It has 6 band-pass filters operating over a range of 170-650 nm with a sensitivity of $B=22.3$ magnitude in a 1000 s exposure and two grism filters for low resolution spectrum. It can determine the position of the sources to an accuracy of 0.3 arcsec.

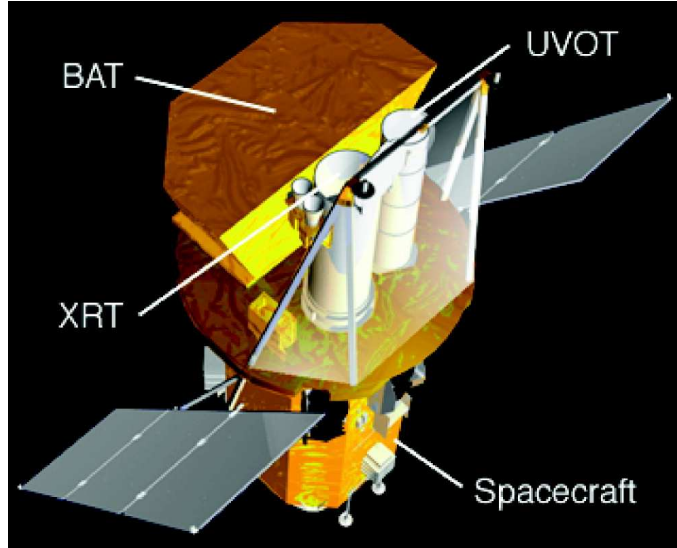


Figure 2.2 An illustration of Swift satellite, with the scientific instruments labeled: XRT, BAT, UVOT.

2.2 Timing analysis

The variations in the X-ray intensity of X-ray binaries are crucial for examining the close vicinity of the compact object. A standard tool for probing the variability is the power spectral density (PSD). Here, following the explanations of Pottschmidt (2002), I describe the mathematical background of the Fourier techniques used for calculating the PSD. A comprehensive review of Fourier analyses of astronomical time series can be found in van der Klis (1989).

2.2.1 The discrete Fourier transform

The variations in the X-ray intensity is usually expressed in terms of a time series of m evenly spaced time bins with the length Δt , each with corresponding count rate x_j where j denotes the time bin number. The discrete Fourier transform (X_k) of such a light curve is then given by

$$X_k = \sum_{j=0}^{m-1} x_j e^{2\pi k j / m} \quad (2.1)$$

where $i = \sqrt{-1}$. Independent values of these complex values, X_k , are obtained for the Fourier frequencies:

$$f_k = \frac{k}{T} = \frac{k}{m\Delta t} \quad (2.2)$$

Here, $T = m\Delta t$ is the length of the light curve. Formally, the Fourier frequencies are defined by $k \in [-m/2, +m/2]$, however, for a light curve the minimum frequency is set by the length of the light curve: $f_{min} = 1/T$, i.e. $k_{min} = 1$. The maximally accessible frequency, the Nyquist frequency, is set by the length of the time bin: $f_{max} = 1/2\Delta t$, i.e.

$k_{max} = m/2$. Since Fourier transform is symmetric, such a setting considers only half of the Fourier frequencies.

An X-ray light curve contains not only the source signal but also noise, i.e. Poisson noise. The measured count rate x_j can be written as a sum of the source s_j and the noise n_j components if the noise is random and uncorrelated. Since the Fourier transform is a linear transformation, then the following holds:

$$X_k = S_k + N_k \quad (2.3)$$

where S_k and N_k are the Fourier transforms of s_j and n_j at the frequency f_k .

2.2.2 The power spectral density (PSD)

2.2.2.1 Calculating and averaging the PSD

The PSD is obtained by multiplying the discrete Fourier transform and its complex conjugate, i.e. the PSD is the squared magnitude of the complex Fourier transform.

$$P_k = X_k^* X_k = |X_k|^2 \quad (2.4)$$

The power spectral density P_k is a quantity that describes the variance of the light curve that is due to the variability characterized by the frequency f_k .

The statistical uncertainty of an individual PSD is of the order of the PSD itself (see van der Klis, 1989). Two methods are often used to achieve a better signal-to-noise ratios (SNR). First is to rebin the power spectrum, averaging W consecutive frequency bins; the second is to split the data up into M equal segments, Fourier transform these segments each individually and then average the resulting M power spectra. Usually both methods are applied together. However, this in turn results in the degrading of the frequency resolution. The uncertainties after this process are reduced by the square root of the number M of independent measurements:

$$\sigma(\langle P \rangle) = \frac{\langle P \rangle}{\sqrt{M}} \quad (2.5)$$

where $\langle P \rangle$ denoting an average over a finite number M of independent measurements. Here, M , is the product of number of light curve segments M_{seg} and the number of Fourier frequencies M_f used to obtain a given $\langle P \rangle$ value:

$$M = M_{seg} \times M_f \quad (2.6)$$

2.2.2.2 Normalizing PSD values

In X-ray astronomy, there are several different conventions for the normalization of the PSD. The normalized PSD is obtained by multiplying the original PSD by a normalization factor A :

$$\langle P_{Norm} \rangle = A \langle P \rangle \quad (2.7)$$

Some commonly used definitions of A are the following:

$$A = \begin{cases} 1 & \text{unnormalized} \\ \frac{2}{TR} & \text{Leahy normalization (Leahy et al., 1983)} \\ \frac{2}{TRR_s} & \text{Miyamoto normalization (Miyamoto \& Kitamoto, 1989)} \end{cases} \quad (2.8)$$

where T is the total length of the observation, $R = \langle x_j \rangle$ is the total time-averaged count rate, and R_s is the signal count rate. R_s is obtained by subtracting the average count rate due to the X-ray background level present in measured light curves:

$$R_s = R - R_{bkg} \quad (2.9)$$

Each of these normalizations has desirable properties. In Leahy normalization, the PSD delivers the light curve variance or the squared root mean square variability, rms^2 , per frequency interval and the Poisson counting noise level have an average of 2. In Miyamoto normalization, the PSDs are in units of the squared fractional rms variability per frequency interval, $(rms/R_{sig})^2/Hz$. The Miyamoto normalization is used to make a comparison of systematic brightness independent similarities between PSDs (shape, fractional rms) whereas the Leahy normalization is used to understand the effects of varying source brightness. i.e. comparing different sources or different states.

2.2.2.3 Statistical uncertainty of the averaged PSD values

If the light curve is long enough, the counts x_j can be assumed to be approximately normally distributed (central limit theorem). In that case, the PSD values are χ^2 distributed with two degrees of freedom (van der Klis, 1989). For Poisson noise, 1σ uncertainty of an individual unbinned PSD value can be shown to be of the order of the intrinsic noise PSD itself. In Leahy normalization, the Poisson noise has a mean value of 2, independent of frequency (white noise). According to χ^2 distribution with two degrees of freedom, its uncertainty amounts to $\sigma(|N_{Poisson,j}|^2) = \sqrt{var(|N_{Poisson,j}|^2)} = \sqrt{4} = 2$. After re-binning, σ reduces to $2/\sqrt{M}$ and approximates a Gaussian distribution. The same is also valid for the signal component of the PSD (van der Klis, 1989):

$$\sigma\langle P \rangle = \frac{\langle P \rangle}{\sqrt{M}} \quad (2.10)$$

This uncertainty must be multiplied with the same normalization factor as chosen for $\langle P_{Norm} \rangle$:

$$\sigma\langle P_{Norm} \rangle = A\sigma\langle P \rangle \quad (2.11)$$

2.2.2.4 Recipe for the temporal analysis

To do timing analysis, one has to obtain a light curve in the desired energy band with the desired time resolution and light curve segmentation. Then the PSDs are calculated for each light curve segments via FFT and the PSDs are averaged to reduce the errors. For the normalization of the

In the early studies, the PSDs of BHXBs have been modeled by a combination of sufficient number of broken power-laws and narrow Lorentzians to take into account the

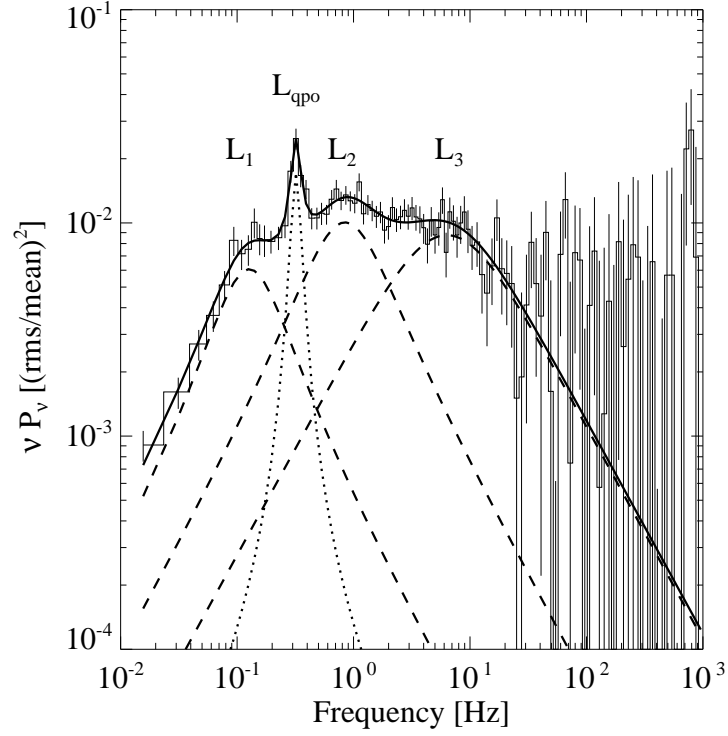


Figure 2.3 Lorentzian fit to a typical PSD. The dashed Lorentzians are broad components ($Q = f_i/\Delta_i < 2$) whereas the dotted Lorentzian is the narrow QPO ($Q > 2$)

broadband noise and the QPOs, respectively (Nowak et al., 1999; Tomsick & Kaaret, 2000). However, recent studies show that the PSDs of BHXBs and NSXBs can be fit successfully by using only broad and narrow Lorentzians (van Straaten et al., 2002; Belloni et al., 2002; Pottschmidt et al., 2003). In this thesis, the PSDs are fit using only Lorentzians for an easier comparison to the recent phenomenology.

The PSDs are fit with Lorentzians in the following form:

$$L_i(f) = \frac{R_i^2 \Delta_i}{2\pi[(f - f_i)^2 + (\frac{\Delta_i}{2})^2]} \quad (2.12)$$

where subscript i denotes each Lorentzian component in the fit, R_i is the rms amplitude of the Lorentzian (if integrated over $-\infty$ to ∞), Δ_i is the full width half maximum, and f_i is the resonance frequency. An important parameter of the Lorentzian is its peak frequency:

$$\nu_i = f_i \left(\frac{\Delta_i^2}{4f_i^2} + 1 \right)^{1/2} \quad (2.13)$$

It corresponds to the frequency at which the contribution to the total rms amplitude of the Lorentzian is maximum.

In Figure 2.3 a sample power spectrum is plotted in the form of PSD \times frequency and the the Lorentzian fits are overplotted. In this work, the Lorentzian components are described by the peak frequency, no the resonance frequency. The broad Lorentzians in

the fits are called as L_i , where $i = 1$ is the lowest frequency peak Lorentzian. The QPO is not counted and always referred as the L_{qpo} in this work.

In this work, only the ‘‘Miyamoto’’ normalization is used for the power spectra. Therefore, the area of the Lorentzians give the fractional rms amplitude. To find the total rms amplitude of variability, the Lorentzians are numerically integrated from 0 to ∞ .

2.3 Spectral Analysis and Models

2.3.1 Spectral Analysis

In X-ray detectors, we use spectrometers to measure the spectrum of a source. The spectrometer does not measure the real spectrum but the photon counts (C) at a given channel (I) which is called photon spectrum ($C(I)$). The photon spectrum $C(I)$ is related to the real spectrum of the source $S(E)$ by:

$$C(I) = T \int RMF(I, E) \cdot ARF(E) \cdot S(E) dE + N(I) \quad (2.14)$$

where T is the exposure time, $RMF(I, E)$ the detector response matrix, $ARF(E)$ the energy-dependent effective area of the telescope and detector system, $N(I)$ the additive noise component. RMF and ARF are combined in a single response file for *RXTE* while they are separate for Swift.

Ideally one would like to determine the real spectrum of the source to make a comparison between the physical data and the models. However, this is practically not possible, as the inversion of Eq. 2.14 tend to be non-unique due to the off-diagonal elements of the response matrix and unstable to small changes in $C(I)$. Alternatively one can choose a model spectrum $F(E)$ that can be described by a number of parameters, convolve it with the instrument response matrix (RMF and ARF) to obtain the predicted counts $C_p(I)$, and then compare the result with the observed photon counts $C(I)$. For the comparison, a fit statistics is computed to evaluate whether the model spectrum correctly describes the data. The most common fit statistics is the χ^2 :

$$\chi^2 = \sum (C(I) - C_p(I))^2 / (\sigma(I))^2 \quad (2.15)$$

where $\sigma(I)$ is the error for channel I. In case of $C(I)$ representing the photon spectrum, $\sigma(I)$ is usually given $\sqrt{C(I)}$. Once a best fit model parameters are obtained, it is considered good if the ratio of the χ^2 to the number of degrees of freedom (χ^2/DOF) is around 1. The ratio is called the ‘‘reduced χ^2 ’’: χ_{red}^2 . If $\chi_{red}^2 \gg 1$, this indicates a poor fit whereas a $\chi_{red}^2 \ll 1$ indicates that the errors on the data have been overestimated.

In this thesis, for the spectral fitting, I use XSPEC software (Arnaud, 1996) which includes commonly used models in the analysis of X-ray binaries.

2.3.2 Spectral Models

The X-ray spectra of a source of interest can be described by a number of model components:

$$S(E) = M_1 * (A_1 + M_2 * A_2) + A_3 \quad (2.16)$$

where $M_i(E)$ and $A_i(E)$ are multiplicative and additive components, respectively. Multiplicative components modify the model by a certain factor depending on the energy, such as the photoabsorption of the interstellar medium, or a normalization factor which takes different cross-calibrations of the instruments into account when data from different instruments are combined together. An additive component does not modify a model but acts only locally at the given energy, such as a Gaussian line or a blackbody.

Below, I present the XSPEC models that I use to fit the observed X-ray energy spectra.

phabs: This model describes the photoabsorption of X-rays by the interstellar medium (ISM). It is a multiplicative model and defined as

$$M(E) = \exp^{-n_H \sigma(E)} \quad (2.17)$$

where $\sigma(E)$ is the energy dependent photoelectric cross section from Balucinska-Church & McCammon (1992) and n_H is the Hydrogen column density in units of 10^{22} atoms/cm².

power law: It is phenomenological so-called the power law model and defined as

$$A(E) = K(E/1\text{keV})^{-\Gamma} \quad (2.18)$$

where K is the normalization (photons/keV/cm²/s) and Γ is the photon index (or spectral index) of power law.

diskbb (disk-blackbody): This physical model is for the optically thick radiation from a standard, geometrically thin accretion disk around a compact object (Makishima et al., 1986).

$$A(E) = \frac{8\pi}{3} r_{in}^2 \cos(i) \int_{T_{out}}^{T_{in}} (T/T_{in})^{-11/3} B(E, T) dT/T_{in} \quad (2.19)$$

where $T_{in} = T(r_{in})$ and $T_{out} = T(r_{out})$ are the innermost and outermost disk temperatures, respectively; E is the emitted photon energy; and $B(E, T)$ is the blackbody photon flux per unit photon energy from a unit surface area of temperature T . The model is parametrized by two variables in XSPEC, T_{in} and a normalization which is equal to $((r_{in}/km)/(D/10kpc))^2 \cos(i)$. Here, r_{in} is the inner disk radius in units of km, and D is the distance from the source in units of 10 kpc.

smedge (smeared iron edge): The energy spectra of accreting X-ray binaries show a significant absorption structure around 7.1 keV, which may be due to iron K_α absorption. It is broader and shallower than a simple edge, therefore to account for its effect a phenomenological model was proposed (Ebisawa et al., 1994). It is defined in XSPEC as

$$M(E) = \begin{cases} 1 & \text{for } E < E_c \\ \exp(-f (E/E_c)^\alpha (1 - \exp^{-(E_c - E)/W})) & \text{for } E > E_c \end{cases} \quad (2.20)$$

where E_c is the threshold energy in keV, f is the maximum absorption factor at threshold, α is the index for photoelectric cross-section (normally -2.67), and W is the smeared width in keV.

gaussian: X-ray binaries often show an excess above the continuum around 6.4 keV which is interpreted as iron emission line. For this I used a simple Gaussian line profile. It is defined as

$$A(E) = \frac{K}{\sqrt{2\pi} \sigma} \exp^{-0.5\left(\frac{E-E_0}{\sigma}\right)^2} \quad (2.21)$$

where E_0 is the centroid energy of the line in keV, σ is the line width, and K (normalization) is the total flux of the line in units of *photons/cm²/s*.

CHAPTER 3

X-Ray, optical and infrared observations of GX 339-4 during its 2011 outburst decay

3.1 Introduction

The X-ray observations of GX 339-4 in 2010 January revealed the start of an outburst (Yamaoka et al., 2010; Tomsick, 2010). Its multiwavelength observations during the rise and spectral properties during the state transitions have been reported elsewhere (Cadolle Bel et al., 2011; Gandhi et al., 2011; Shidatsu et al., 2011a,b; Stiele et al., 2011; Yan & Yu, 2012). In 2011 January, the source made a transition from the intermediate to the hard state during the outburst decay (Munoz-Darias et al., 2011). The optical observations through the end of 2011 February revealed a rebrightening (Russell & Lewis, 2011) which was also observed in previous outburst decays of GX 339-4 (Buxton et al., 2012). In the following, we present the analysis of *RXTE*, *Swift*, and SMARTS observations of GX 339-4 during its 2011 decay. The results of this section is published in Dincer et al. (2012).

3.2 Observations and data analysis

3.2.1 *RXTE* observations

The outburst decay was amply covered with 54 pointed *RXTE* observations between MJD 55,560 and 55,650 (2010 December 30 and 2011 March 30). However, some observations were not statistically satisfactory due to the short good time intervals (GTIs) and/or small number of Proportional Counter Unit (PCU) during the operation. Therefore, we did not include the observations with $GTI < 500$ s (see Table 3.1 for a log of observations).

We used data from the Proportional Counter Array (PCA) instrument on board the *RXTE* for the spectral analysis (Jahoda et al., 1996). In most of the observations, the spectra were extracted in the 3–25 keV energy band, but in a few cases for which the noise dominated above 20 keV, we used the 3–20 keV band. The response matrix and the background model were created using the standard FTOOLS (v6.11) programs. We added 0.5% systematic error to the energy spectra following the suggestions of the *RXTE* team.

The spectral analysis was performed using XSPEC 12.0.7 (Arnaud, 1996). We employed a spectral model for the continuum that consists of absorption, a multicolor disk

blackbody and, a power law. We also included a phenomenological smeared edge model (Ebisawa et al., 1994) for the iron K_{α} absorption edge seen around 7.1 keV to obtain acceptable χ^2 values for the observations before MJD 55,606. In the spectral fits, the hydrogen column density, N_{H} , and the smeared edge width were fixed at $0.5 \times 10^{22} \text{ cm}^{-2}$ (Kong et al., 2000) and 10 keV, respectively. This model was used previously in Tomsick et al. (2001) and Kalemci et al. (2004, 2005, 2006a).

The Galactic ridge emission was an important factor for the faint observations. In order to estimate its spectrum we compared quasi-simultaneous *RXTE* and *Chandra* observations obtained on MJD 52,911. We combined seven *RXTE*/PCA observations taken on the same day and fitted with a model consisting of interstellar absorption, a power law and a Gaussian to represent the Galactic ridge emission, and a second power law to represent the source. The centroid energy and width of Gaussian were fixed at 6.6 keV and 0.5 keV respectively. The parameters of the second power law from the source were set to the values obtained from *Chandra* observation (Gallo et al., 2003b). With this method we modeled the Galactic ridge emission with a power-law index of 2.1 and an unabsorbed flux of $7.55 \times 10^{-12} \text{ erg cm}^{-2} \text{ s}^{-1}$ in the 3–25 keV band (Dinçer et al., 2008; Coriat et al., 2009). We applied Galactic ridge emission correction to the spectra, fluxes and rms amplitudes of the observations after MJD 55,627. The contamination from Galactic ridge emission was not greater than 3% of the total flux for the observations before this date.

For each PCA observation, we produced power density spectrum (PDS) from segments of length 256 s with a time resolution of 2^{-9} s in the 3–30 keV energy band using IDL programs developed at University of Tübingen. The averaged PDS were normalized as described in Miyamoto & Kitamoto (1989) and corrected for the dead-time effects according to Zhang et al. (1995). Then, PDS were fit using Lorentzians in the 0.004–256 Hz range. The rms amplitudes are obtained by integrating the normalized PDS and corrected for both the background and the ridge emission as described in Kalemci et al. (2006a). All spectral and timing results are presented in Table 3.1.

3.2.2 *Swift* observations

We also analyzed *Swift* X-ray Telescope (XRT) observations conducted at the same time period with the *RXTE* observations. We found 12 observations carried out between MJD 55,622 and 55,647. We used them together with the *RXTE* observations and looked for the presence of any spectral softening.

We analyzed the XRT photon counting mode event data using XRTPIPELINE task provided in FTOOLS package. Pile-up was an issue for the first four observations whose count rates were greater than 1 counts s^{-1} . To remove its effects, following the Swift Science Data Center (SSDC) recommendations, we selected the source photons from a ring with an inner radius of $5''$ and an outer radius of $40''$. For the rest of the observations, the source photons were selected in a circular region with a radius of $40''$. The background photons were accumulated from a ring with an inner radius of $70''$ and an outer radius of $100''$ centered at the source position.

For the spectral analysis, only events with grades 0–12 were selected. The auxiliary response files were created by XRTMKARF and corrected using the exposure maps, and the standard response matrix swxpc0to12s6_20010101v013.rmf was used. We binned the energy spectra by fixing the number of counts per bin at 50. We fitted the spectra

with a model that consists of photoabsorption and a power law in the 0.6–8.0 keV band. In our initial spectral runs, we let the N_{H} free, and the resulting values were between $(0.3 - 0.7) \times 10^{21} \text{ cm}^{-2}$. As we were not able to constrain the N_{H} , we performed a second run with N_{H} fixed at $0.5 \times 10^{22} \text{ cm}^{-2}$. The log of *Swift* observations and the spectral results are presented in Table 3.1.

3.2.3 SMARTS observations

The regular optical/infrared observations were performed with the ANDICAM (DePoy et al., 2003) camera on the SMARTS 1.3m telescope in V , I , J and H bands. The observations covered the outburst decay on daily basis between MJD 55,582 and 55,720. In this paper, we focus on the OIR light curves and evolution of the SEDs.

The dereddening of the observed magnitudes and their conversion to physical units were critical to create SEDs. For this purpose, we used the optical extinction, $A_V = 3.7 \pm 0.3$ (Zdziarski et al., 1998) together with the extinction laws given by Cardelli et al. (1989). The same A_V was previously utilized in Corbel & Fender (2002), Coriat et al. (2009), and Buxton et al. (2012) for the SED creation. We calculated the extinction coefficient in the other bands using $A(\lambda)/A(V) = a(x) + b(x)/R_V$ and the relationships for $a(x)$ and $b(x)$ as given in O’Donnell (1994) for V and I bands, and Cardelli et al. (1989) for J and H bands. In calculating $a(x)$ and $b(x)$, we used the effective wavelength for each band (Frogel et al., 1978; Elias et al., 1982; Bessell et al., 1998): $V = 545 \text{ nm}$, $I = 798 \text{ nm}$, $J = 1250 \text{ nm}$, and $H = 1650 \text{ nm}$. The errors on the dereddened magnitudes are dominated by the error in A_V , and are as follows: $V_{err} = 0.3 \text{ mag}$, $I_{err} = 0.1 \text{ mag}$, $J_{err} = 0.1 \text{ mag}$, and $H_{err} = 0.1 \text{ mag}$. Adding the photometric and interstellar reddening errors in quadrature give the following total errors on dereddened magnitudes: $V_{err} = 0.30 \text{ mag}$, $I_{err} = 0.10 \text{ mag}$, $J_{err} = 0.10 \text{ mag}$, and $H_{err} = 0.10 \text{ mag}$.

To convert the dereddened magnitudes to flux (in units of Jy) we used the following zero-point fluxes (where the zero-point flux of a given filter is that corresponding to zero magnitude): $V_0 = 3636 \text{ Jy}$, $I_0 = 2416 \text{ Jy}$ (Bessell et al., 1998), $J_0 = 1670 \text{ Jy}$, and $H_0 = 980 \text{ Jy}$ (Frogel et al., 1978; Elias et al., 1982).

3.3 Results

3.3.1 X-ray evolution

In Figure 3.1, we present the evolution of the spectral and the temporal parameters. On MJD 55,594, dramatic changes occurred in both the X-ray spectral and the temporal parameters. The rms amplitude of variability jumped from 9.8% to 17.4% in one day. Both the disk flux and the temperature of the inner disk decreased. The power-law flux increased and the photon index started to harden. These changes in the evolution of the parameters suggest a reshaping of the accretion dynamics and lead to a transition from the soft-intermediate state toward the hard state. In Figure 3.2, we show the hardness–intensity diagram and mark the start of the state transition. Based on the extrapolation of the power-law model, the X-ray luminosity at the start of the transition is $L_{1-200 \text{ keV}} = 2.7 \times 10^{37} \text{ erg s}^{-1}$ or $\sim 2\% L_{\text{Edd}}$ if we adopt a distance of 8 kpc (Hynes et al., 2004;

Table 3.1. Observational Parameters Obtained from *RXTE* Data

Observation ID. ^a	MJD ^b	GTIs (ks)	Γ	T_{in} (keV)	PL Flux ^c	DBB Flux ^d	rms ^e (%)	ν^{f} (Hz)
45-00	55,559.58	0.77	2.44 ± 0.11	0.60 ± 0.01	4.45	8.02	<1.82	...
01-00	55,561.05	0.70	2.46 ± 0.09	0.58 ± 0.01	5.49	7.35	<2.75	...
01-01	55,563.14	0.74	2.34 ± 0.14	0.59 ± 0.02	4.14	7.33	<5.90	...
01-02	55,565.82	0.53	2.46 ± 0.13	0.57 ± 0.02	5.63	5.98	<6.08	...
01-03	55,567.91	0.60	2.60 ± 0.07	0.58 ± 0.02	8.71	5.30	<2.73	...
02-03	55,574.87	1.03	2.27 ± 0.09	0.56 ± 0.01	5.95	4.37	<5.25	...
03-00	55,576.85	1.44	2.50 ± 0.07	0.56 ± 0.01	7.51	4.02	<4.15	...
03-01	55,578.88	1.40	2.40 ± 0.06	0.56 ± 0.01	6.94	3.59	10.16 ± 1.71	...
03-02	55,580.61	1.32	2.45 ± 0.06	0.55 ± 0.02	8.05	3.62	8.08 ± 0.53	...
04-00	55,582.70	0.54	2.57 ± 0.12	0.54 ± 0.03	7.32	3.09	<7.50	...
04-04	55,585.94	0.98	2.32 ± 0.04	0.56 ± 0.01	7.62	3.20	8.88 ± 0.19	2.09 ± 0.06
04-02	55,586.49	0.70	2.46 ± 0.10	0.55 ± 0.03	7.56	2.96	8.52 ± 0.73	...
04-07	55,587.50	0.52	2.38 ± 0.12	0.54 ± 0.03	6.38	2.35	7.82 ± 1.00	...
04-08	55,588.55	0.54	2.36 ± 0.14	0.53 ± 0.03	4.95	2.53	<10.94	...
05-00	55,589.20	0.58	2.35 ± 0.12	0.52 ± 0.03	5.97	2.30	<9.90	...
05-04	55,590.43	0.58	2.43 ± 0.12	0.51 ± 0.04	6.10	1.87	<10.61	...
05-01	55,591.61	1.31	2.15 ± 0.05	0.53 ± 0.02	6.69	2.59	8.63 ± 0.25	1.77 ± 0.06
05-05	55,592.73	0.83	2.35 ± 0.10	0.51 ± 0.04	6.25	1.67	11.30 ± 0.87	1.72 ± 0.05
05-02	55,593.50	1.55	2.44 ± 0.08	0.52 ± 0.02	5.89	2.01	9.83 ± 0.43	...
05-03	55,594.89	1.23	2.29 ± 0.06	0.50 ± 0.05	7.31	1.10	17.54 ± 2.56	...
06-00	55,597.25	0.98	2.01 ± 0.03	0.42 ± 0.05	9.27	0.48	19.38 ± 1.29	1.03 ± 0.05
06-01	55,598.66	1.09	2.11 ± 0.06	0.44 ± 0.08	7.94	0.50	25.18 ± 1.48	...
06-02	55,601.88	1.80	1.89 ± 0.03	0.44 ± 0.18	8.35	0.11	22.94 ± 1.71	1.39 ± 0.05
07-00	55,603.98	0.74	1.77 ± 0.04	...	7.97	0.00	17.46 ± 1.62	...
07-03	55,604.89	1.28	1.75 ± 0.02	...	7.61	0.00	26.16 ± 1.93	...
07-01	55,606.89	1.05	1.67 ± 0.04	...	6.82	0.00	25.02 ± 1.12	...
07-02	55,607.76	1.26	1.71 ± 0.02	...	6.05	0.00	23.04 ± 1.96	...
07-04	55,609.84	1.24	1.66 ± 0.02	...	4.82	0.00	33.98 ± 2.58	...
08-00	55,611.60	1.44	1.70 ± 0.02	...	3.74	0.00	37.76 ± 4.00	...
08-02	55,613.72	0.66	1.70 ± 0.03	...	2.88	0.00	29.08 ± 1.93	...
08-01	55,615.45	0.85	1.64 ± 0.03	...	2.50	0.00	32.84 ± 1.68	...
08-03	55,616.57	0.58	1.70 ± 0.04	...	2.33	0.00	37.62 ± 8.70	...
09-00	55,617.53	1.68	1.69 ± 0.04	...	2.16	0.00	40.49 ± 8.33	...
10-02	55,628.65	1.54	1.77 ± 0.07	...	1.03	0.00	33.64 ± 2.97	...
10-03	55,630.23	0.70	1.70 ± 0.04	...	1.05	0.00	35.26 ± 6.05	...
11-00	55,632.05	1.22	1.77 ± 0.09	...	0.91	0.00	44.79 ± 4.17	...
11-02	55,636.20	0.59	1.68 ± 0.10	...	0.70	0.00	43.23 ± 5.35	...
12-00	55,638.73	1.46	1.69 ± 0.12	...	0.59	0.00	41.03 ± 3.58	...
12-01	55,639.50	1.52	1.86 ± 0.14	...	0.50	0.00	51.31 ± 10.72	...
13-00	55,646.29	1.23	1.38 ± 0.24	...	0.31	0.00
13-01	55,649.64	0.62	1.72 ± 0.35	...	0.28	0.00
00031931011	55,622.66	1.20	1.54 ± 0.10
00030943021	55,624.06	1.27	1.55 ± 0.10
00030943022	55,626.00	1.20	1.47 ± 0.12
00030943023	55,628.81	1.31	1.70 ± 0.12
00031931012	55,629.82	1.16	1.54 ± 0.17
00030943024	55,630.69	1.30	1.52 ± 0.10
00030943025	55,632.43	1.06	1.65 ± 0.21
00030943026	55,634.10	1.19	1.59 ± 0.16
00030943027	55,638.93	1.30	1.58 ± 0.14
00030943029	55,642.46	1.06	1.76 ± 0.19
00031931014	55,643.21	1.19	1.65 ± 0.16
00030943030	55,646.15	2.20	1.59 ± 0.13

^aFull observation ID is 95409-01-Obs for the first observation, and 96409-01-Obs for the rest.

^bModified Julian Date (JD−2,400,000.5) at the start of the observation.

^cUnabsorbed power law flux in the 3–25 keV band, in units of $10^{-10} \text{ erg cm}^{-2} \text{ s}^{-1}$.

^dUnabsorbed disk blackbody in the 3–25 keV band, in units of $10^{-10} \text{ erg cm}^{-2} \text{ s}^{-1}$.

^eThe total rms amplitude of variability integrated over a range of 0–∞ Hz in the 3–30 keV band.

^fQPO centroid frequency.

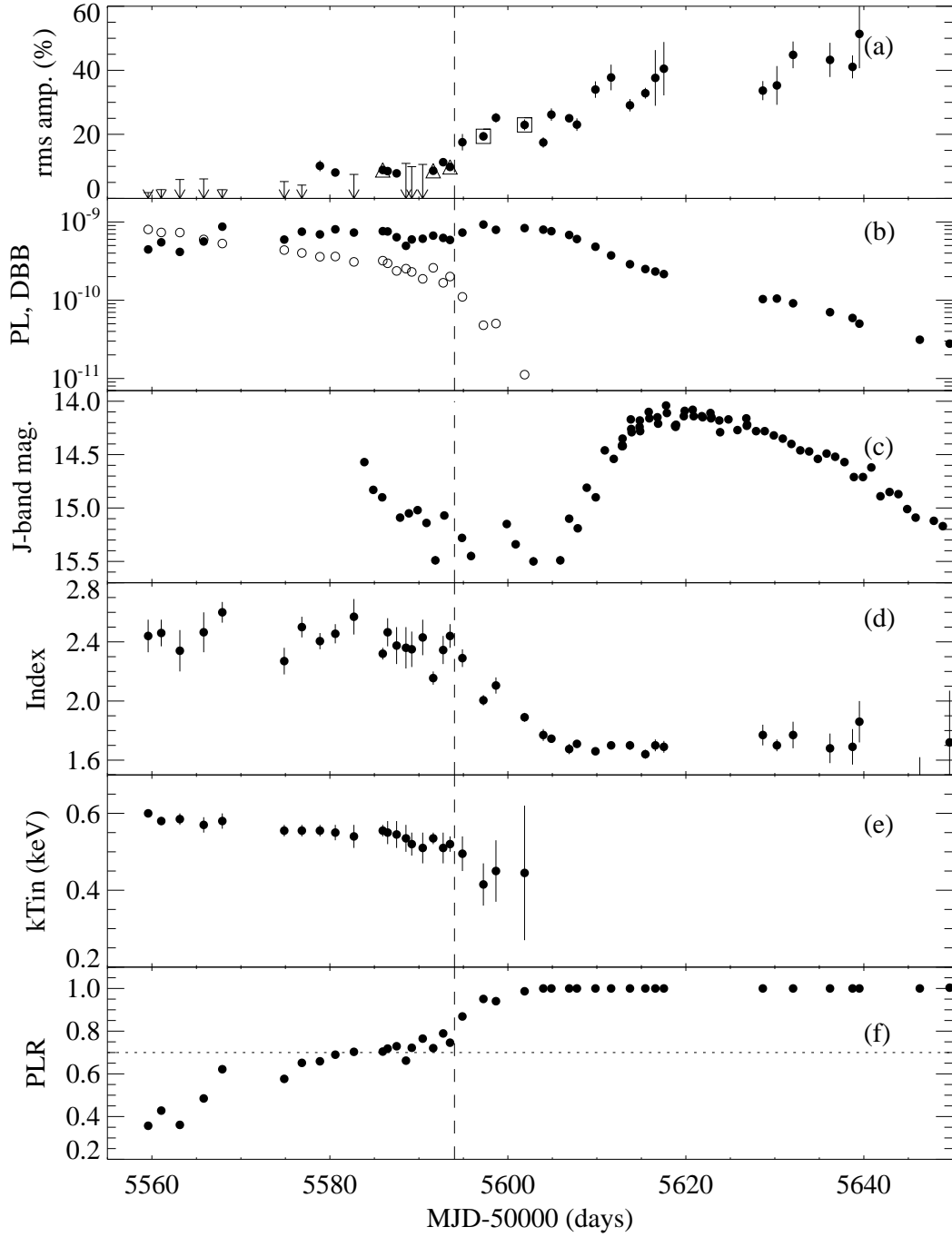


Figure 3.1 Evolution of (a) the total rms amplitude of variability in the 3–30 keV band, (b) the power-law flux (filled circles) and the disk blackbody flux (empty circles) in the 3–25 keV band in units of $10^{-10} \text{ erg cm}^{-2} \text{ s}^{-1}$, (c) J -band IR light curve, (d) the photon index Γ , (e) the inner disk temperature T_{in} , (f) the ratio of the power-law flux to the total flux in the 3–25 keV band. Dashed line indicates the time of state transition on MJD 55,594. Triangles and squares show the observations with type B and C QPOs, respectively.

Zdziarski et al., 2004) and a mass of $10 M_{\odot}$ (Hynes et al., 2003a; Muñoz-Darias et al., 2008).

Before the transition, the energy spectra were soft with a mean photon index of 2.37. There was comparable contribution to the total X-ray flux from the disk and the power-law components. The power-law ratio (PLR, the ratio of the power law flux to the total flux in the 3–25 keV band) was increasing from 0.40 to 0.75 level. This increase was due to the steady decrease in the disk flux. In addition to the decreasing disk flux, the inner disk temperature was also decreasing. The first detection of the X-ray variability occurred when the PLR reached 0.7. The rms amplitude of variability was less than 10%. Our analysis confirms the type B QPO detections reported in Stiele et al. (2011). All these spectral properties indicate that the source was in transition from the soft to the hard state, or simply in the intermediate state (Kalemci et al., 2004).

After the transition, the energy spectra became dominated by the power-law component in six days. At the same time, the photon index hardened from 2.3 to 1.8. The power-law flux increased and remained at a higher level than its soft-intermediate state level. Again during these six days the rms amplitude of variability increased to 25%. For two observations, type C QPOs (according to the classification in Motta et al. 2011) were detected (see Figure 3.1 and Table 3.1). After MJD 55,605 the disk component was no more significant and no longer needed in the energy spectra. The power law flux started to decay and the photon index kept decreasing until it leveled off at 1.70. The rms amplitude of variability gradually increased to 50% in 30 days.

3.3.2 No evidence for softening

We also inspected the possible presence of softening of the spectra at low flux. In Figure 3.3, we plotted the evolution of the photon index obtained from both the *RXTE* and *Swift* observations between MJD 55,611 and 55,650. The *RXTE* indices are systematically higher than the *Swift* indices, however both data sets are separately consistent with a flat evolution ($\Gamma = 1.53 \pm 0.06$, 1.70 ± 0.01 for *Swift* and *RXTE*, respectively). The reason for the systematic difference may be caused by the use of different energy bands in *RXTE* and *Swift* spectra. If the Galactic ridge emission is underestimated, the *RXTE* spectral indices would become slightly harder, but not enough to account for the entire difference. Regardless of the deviation between two data sets we conclude that the data suggest no evidence for the softening of the spectra between MJD 55,610 and 55,650.

3.3.3 Light curves

In Figure 3.4, we present the evolution of the power-law and disk blackbody fluxes together with the OIR light curves obtained during the 2011 decay. The dashed line shows the time of state transition from the soft-intermediate to the hard-intermediate state whereas the dotted line shows the start time of the OIR rebrightening. To find the start of the rebrightening, we first formed a baseline that smoothly connects the fluxes before (between MJD 55,590 – 55,604) and after (MJD 55,680 – 55,690) the flare as an exponential decay. We assumed that the physical origin of the rebrightening is separate from that of the baseline. We then fitted the rise of the rebrightening (between MJD 55,608 and 55,612) in the infrared bands only with a straight line over the baseline. We used the

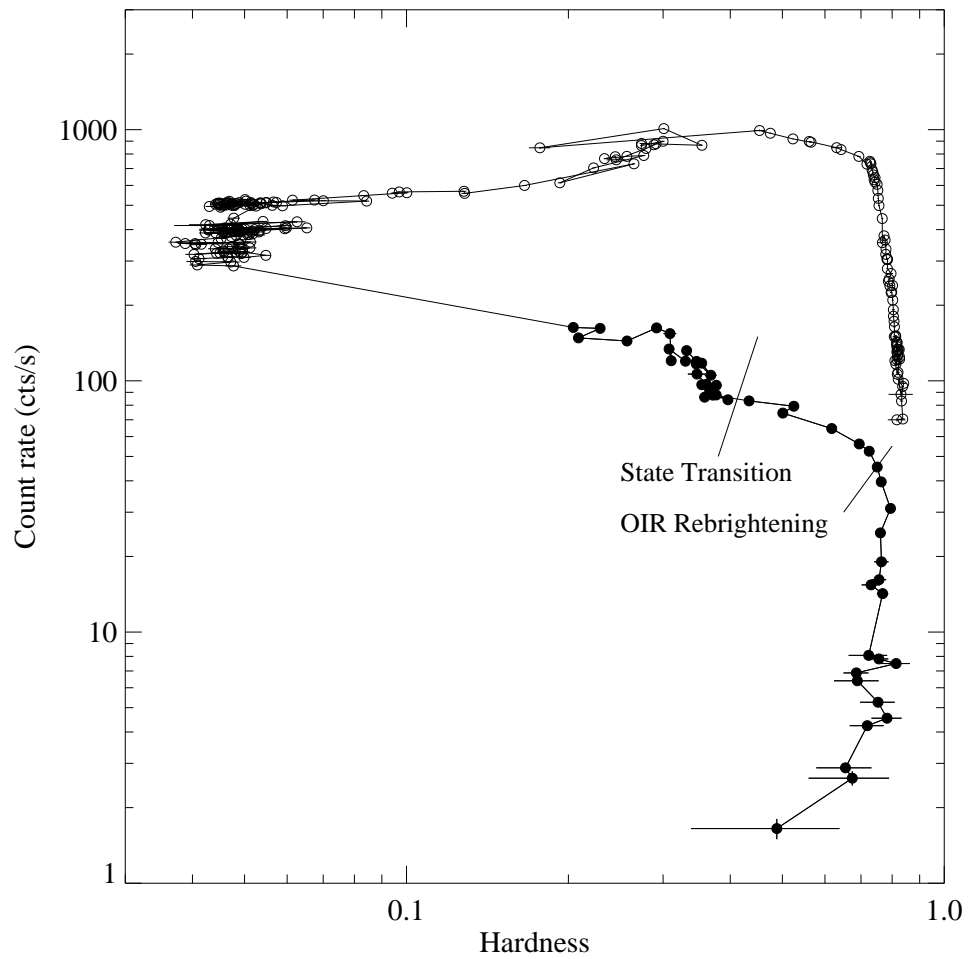


Figure 3.2 Start of the state transition and the approximate time of the OIR rebrightening are marked in the hardness-intensity diagram of the entire outburst. Observations analyzed in this thesis are shown with filled circles.

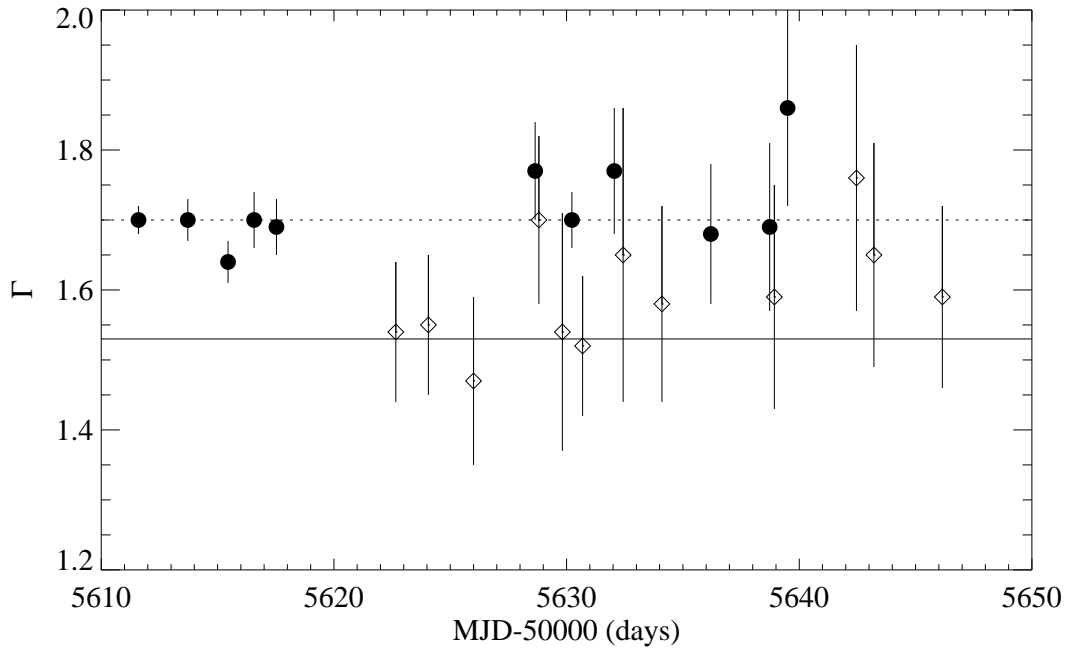


Figure 3.3 Evolution of the photon index obtained from RXTE (circles) and Swift (diamonds) observations between MJD 55,611 and 55,650. Best fit values at 1.53 and 1.70 constant levels for *RXTE* (dotted line) and *Swift* (solid line) only points, respectively.

infrared, since the fluctuations are lower during the early part of the rebrightening compared to the optical bands. The start of the flare is defined as the date that the linear fit intersects zero, and it is $\text{MJD } 55,607 \pm 1$ day.

The evolution of the disk and the power-law flux were described in Section 3.3.1. As the source transitioned to the hard-intermediate state the power-law flux increased, and the OIR rebrightening occurred when the spectrum was almost its hardest (see also Figures 3.1 and 3.2). There was a delay of ~ 12 days between the increase in the power-law X-ray flux and the OIR rebrightening. The rebrightening started at a PCA flux of $F_{3-25 \text{ keV}} = 7.6 \times 10^{-10} \text{ erg cm}^{-2} \text{ s}^{-1}$, resulting in a bolometric luminosity of $L_{1-200 \text{ keV}} = 1.8 \times 10^{37} \text{ erg s}^{-1}$ or $\sim 1.4\% L_{\text{Edd}}$. Note that such a delay has already been noticed for other black hole transients, namely XTE J1550-564 (Kalemci et al., 2006b), 4U 1543-47 (Kalemci et al., 2005) and also for GX 339-4 (Coriat et al., 2009).

The evolution in OIR in different bands are similar (see Figure 3.4). A decay is followed by ~ 70 days of rebrightening that peaked around the same dates before reaching a constant level. The amount of brightening is, however, different among the bands. Ratio of the peak flux to the baseline flux decreases from *H* to *V* (max ~ 4.9 to ~ 3 on MJD 55,620).

3.3.4 Evidence for binary period in the optical light curves

OIR light curves shown in Figure 3.4 fluctuate during the initial decay (between MJD 55,580 and 55,605) in a timescale of days. The fluctuations continue even on the rise and the peak of the rebrightening. Moreover, some parts of the light curves seem to show

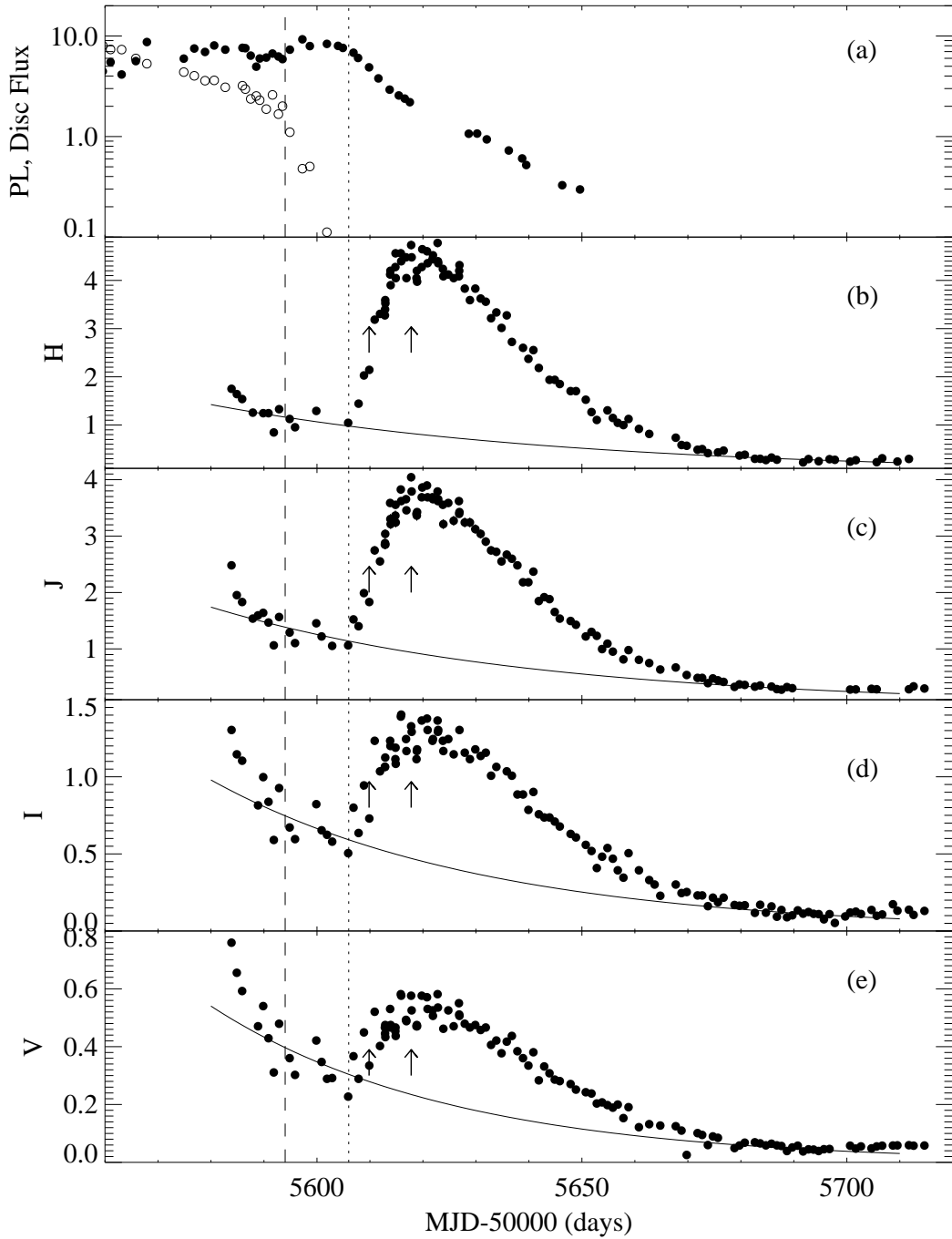


Figure 3.4 *RXTE*/PCA X-ray, and SMARTS OIR light curves of GX 339-4. (a) X-ray flux in the 3–25 keV band in units of $10^{-10} \text{ erg cm}^{-2} \text{ s}^{-1}$. Filled circles: power-law flux (PL), empty circles: disk flux. (b-e) Underreddened *H*, *J*, *I* and *V* light curves in units of mJy. (Error bars are smaller than the plot symbols.) The dashed line indicates the X-ray state transition and the dotted line indicates the start time of the OIR rebrightening. The solid lines show the baseline emission possibly originating in the disk. The arrows point the dates for which we constructed the SEDs (MJD 55,609.84 and MJD 55,617.53).

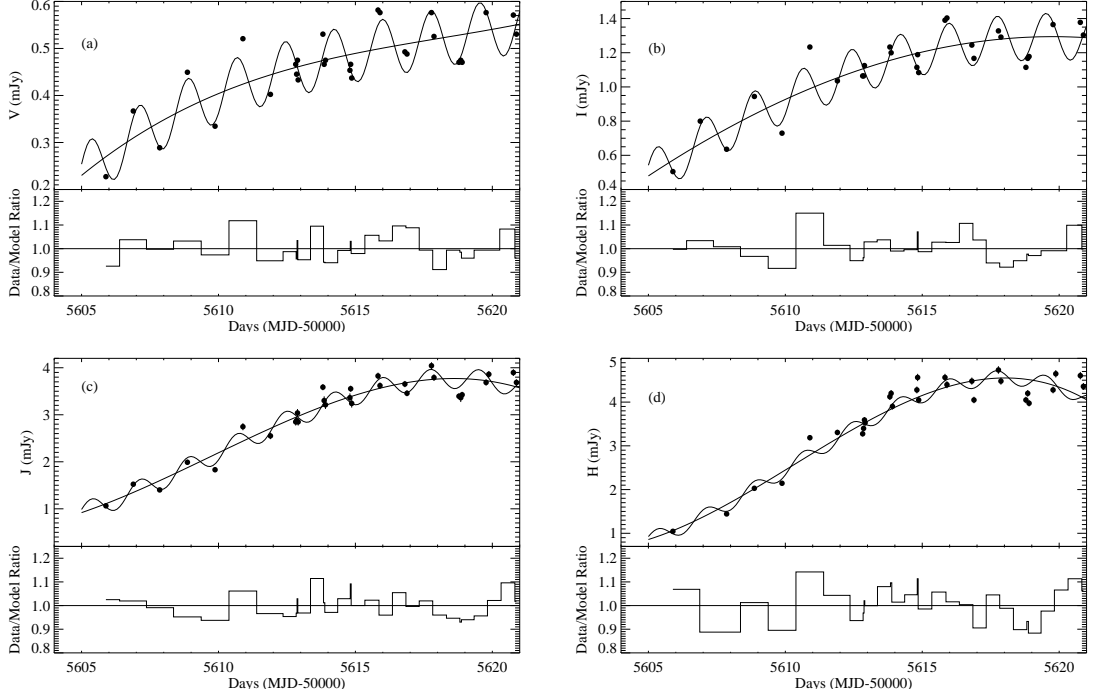


Figure 3.5 Fluctuations in (a-d) V , I , J and H light curves respectively in flux units of mJy. The solid lines describe the rise of the rebrightening together with the fluctuations with a third degree of polynomial with a sinusoidal.

regular modulations. Therefore, we decided to search for periodicity in all bands using the Lomb–Scargle algorithm (Scargle, 1982). The initial decay (between MJD 55,580 and 55,605) did not provide a significant peak in the periodogram in any of the bands. Likewise, there is no evidence for periodicity in the light curves after MJD 55,630.

On the other hand, we detected the known binary period of the system at 1.77 days (Hynes et al., 2003a; Levine & Corbet, 2006) in the V , I and J band light curves between MJD 55,605 and 55,621, which is the rise and the peak of the rebrightening. Using the method of Horne & Baliunas (1986) the false alarm probabilities of the known period are estimated as 2.2×10^{-4} , 1.6×10^{-4} , and 7.6×10^{-3} (3.69σ , 3.78σ , and 2.78σ) for the V , I , and J bands, respectively. We performed a detailed fitting with the following function:

$$F_{\text{oir}} = a + bt_0 + ct_0^2 + dt_0^3 + A \sin\left(\frac{2\pi}{P}t_0 + \phi\right) \quad (3.1)$$

where t_0 is defined as the time from MJD 55,605, and F_{oir} is in units of mJy. The polynomial part of the Equation (3.1) represents the continuum of the rebrightening whereas the periodic part represents the modulations with the binary period $P = 1.77$ days obtained from the periodogram. The model parameters obtained from the fits are given in Table 3.2 and the best model fits to the data are shown in Figure 3.5. The phases are consistent among all bands. Note that for the H band the periodic modulation is not necessary to fit the data, however the first few points are consistent with the binary period if the modulation is included in the fit.

Table 3.2. Model Parameters Derived from the Light Curves (for a Fixed Period $P = 1.77$ days)

Parameters	V	I	J	H
a (mJy)	0.229 ± 0.001	0.479 ± 0.007	0.918 ± 0.017	0.820 ± 0.050
b (mJy day $^{-1}$)	0.047 ± 0.002	0.105 ± 0.004	0.200 ± 0.029	0.213 ± 0.026
c (mJy day $^{-2}$)	-0.0029 ± 0.0003	-0.0031 ± 0.0006	0.017 ± 0.004	0.033 ± 0.004
d (mJy)	$(7.23 \pm 1.25) \times 10^{-5}$	$(-2.27 \pm 2.62) \times 10^{-5}$	-0.0011 ± 0.0002	-0.0021 ± 0.0001
A (mJy)	0.061 ± 0.001	0.136 ± 0.003	0.216 ± 0.02	0.17 ± 0.02
ϕ (rad)	0.40 ± 0.02	0.48 ± 0.02	0.320 ± 0.079	0.232 ± 0.105

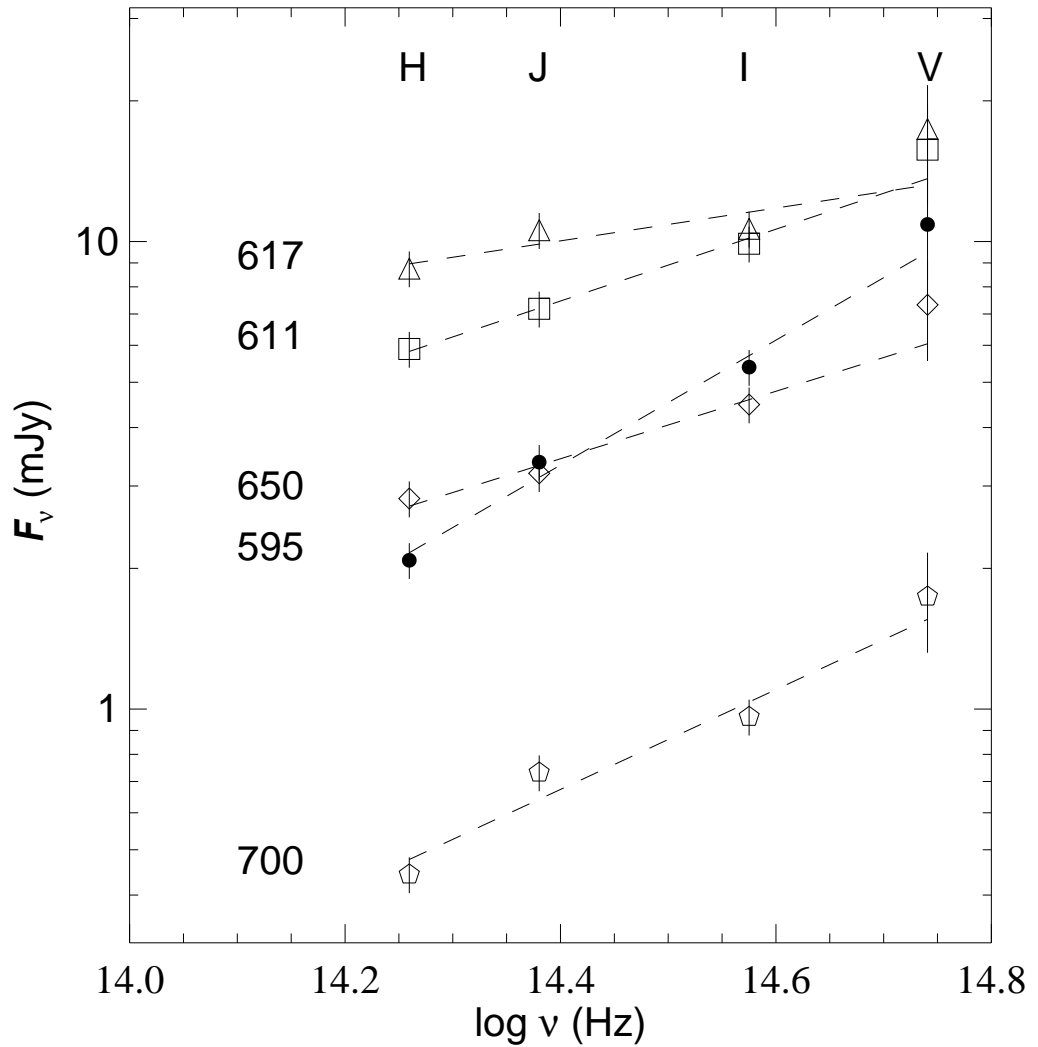


Figure 3.6 Dereddened OIR SEDs sampled from different stages of both intermediate and hard states. The numbers indicate the dates in the form of MJD–55,000. The dashed lines show the power-law best fits to the data from individual days.

3.3.5 SEDs

We created SEDs to inspect the physical components and the mechanisms that produce the observed emission in both the intermediate state and the hard state. Below we will present our observational results by exploring the evolution of the OIR SED alone, and then together with the X-rays.

3.3.5.1 OIR SEDs

Figure 3.6 shows several SEDs of the total emission sampled from different stages of the OIR evolution. In order to quantitatively track the evolution, each SED was fitted with a power law. The evolution of the SED started with higher spectral slopes (all slopes are negative, and α represents the absolute value of the slopes throughout the paper) in the hard intermediate state ($\alpha = 1.33$ on MJD 55,595) and continuously decreased ($\alpha = 0.76$ on MJD 55,611) until the peak of the OIR rebrightening in the hard state. During the peak, the slope of the SED became flatter ($\alpha = 0.35$ on MJD 55,618). As the OIR decayed, the slope started to increase again ($\alpha = 0.72$ on MJD 55,650). At the end of the decay where the OIR emission decreased to a constant level in all bands, the spectral slope had a less steep value ($\alpha = 1.07$ on MJD 55,700) than it was in the hard-intermediate state. The typical errors for the spectral slopes were around ± 0.15 at 1σ , but note that the relative slopes are not affected by the dereddening process which dominates the error calculation.

3.3.5.2 Broadband SEDs

In order to understand the emission mechanism that gives rise to the rebrightening, we constructed two broadband SEDs in Figure 3.7 with the total OIR (circles), the excess OIR (diamonds), and the X-ray fluxes from MJD 55,609.84 and 55,617.53 (rise and peak of rebrightening, see Figure 3.4). The total OIR fluxes were calculated using the polynomial part of Equation (3.1) (the solid curves in Figure 3.5). This way we removed the effect of modulations with the binary period found in Section 3.3.4. We then removed the baseline flux to find the SED of the excess. We calculated the errors on the flux densities by only considering the calibration and interstellar extinction. The errors from the baseline and the rebrightening fits were negligible. The excess OIR spectra yielded flat spectra with spectral slopes of 0.15 ± 0.15 for MJD 55,609.84 and -0.05 ± 0.15 for MJD 55,617.53. We refer to the Section 3.4 for the explanation of the lines in Figure 3.7.

3.4 Discussion

The changes observed in both the spectral and the temporal parameters imply a change in accretion dynamics. The most clear changes in both the X-ray spectral and temporal parameters occurred on MJD 55,594. We marked this date as the start of the transition from soft-intermediate state towards the hard state. Throughout the decay phase of the outburst, GX 339-4 generally presented typical X-ray and OIR behavior as observed from other black holes, and also of its previous outburst decays.

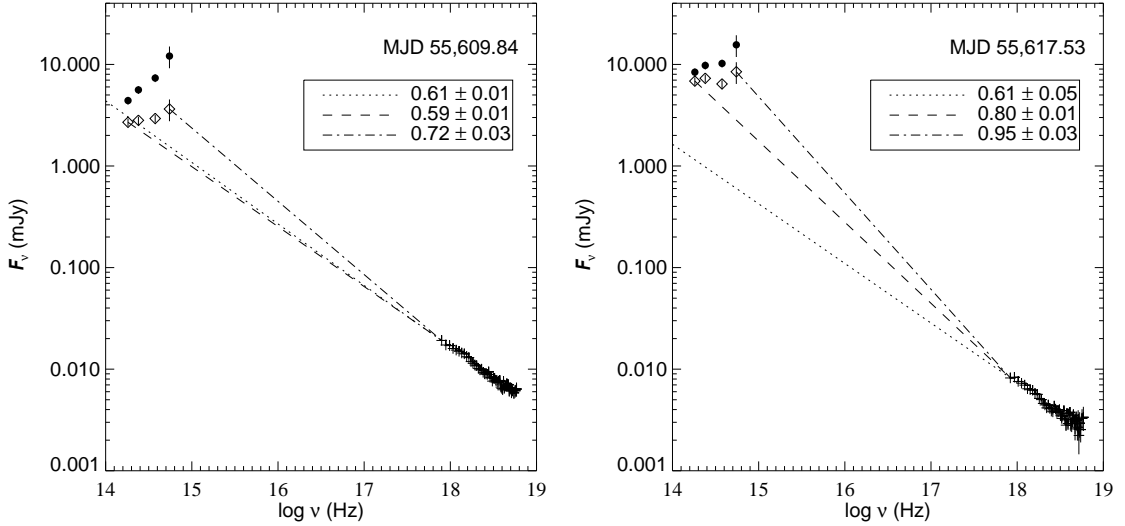


Figure 3.7 Broadband SEDs for MJD 55,609.84 and MJD 55,617.53. Black circles: the total flux density of the source; diamonds: baseline subtracted flux density. Dotted line: power-law fit extrapolations from X-rays; dashed line: power-law fit from the H band to softest X-rays (3 keV); dashed-dotted lines: power-law fit from the V band to softest X-rays (3 keV). The power-law indices from the fits are shown in the legends. The errors on the slopes are calculated from the difference between the two slopes obtained by the fits from mid points of the OIR flux densities and the 1σ above the mid points.

3.4.1 Evolution in the X-ray regime

In the soft-intermediate state, the evolution in X-ray and OIR regimes was quite typical. Smoothly decaying disk temperature and disk flux may imply the presence of a steadily cooling accretion disk. Variable power-law flux with a variable soft photon index can be thought as arising from a variable corona which has some overlap with the accretion disk that provides strong cooling. The emission mechanism that produces the power law component is most probably the thermal Comptonization (Sunyaev & Titarchuk, 1980).

After the start of state transition, the disk temperature and the disk flux rapidly decayed and remained out of the PCA energy range in about 10 days. As the disk is thought to be the source of seed photons in the Comptonization process, this is most often interpreted as the reduction in the number of soft seed photons. This results in a less cooling of the corona, and higher electron temperature which is consistent with the observed hardening of photon index. This simple Comptonization scenario could change or be modified with the onset of compact jet. Because the jet can either provide additional source of seed photons from non-thermal synchrotron emission at the base of jet (corona) and channel some portion of the accretion energy into its own power (Fender et al., 2003). These processes could provide a sharp increase in the rms amplitude of variability (Hynes et al., 2003b; Russell et al., 2012) and/or a softening of the X-ray spectrum (Dinçer et al., 2008; Russell et al., 2010), however no such sharp changes in the X-ray spectral and temporal properties were observed during rebrightening in the OIR.

3.4.2 Origin of OIR emission on the initial decay

At the initial decay (between MJD 55,585 and 55,605, see Figure 3.4), the OIR flux was most probably dominated by the thermal emission originating from the outer parts of the accretion disk as the secondary star is not expected to contribute to the OIR flux significantly (Shahbaz et al., 2001). This is supported by the higher spectral slopes observed compared to the slopes during the rebrightening (see Figure 3.6). Additionally, the spectral slope of 1.34 ± 0.16 in this stage is lower than the expected spectral index from the Rayleigh–Jeans tail of the blackbody ($F_\nu \propto \nu^2$) and seems consistent with the X-ray irradiation of the disk (Hynes, 2005; Coriat et al., 2009; Buxton et al., 2012). The strong variability in the light curve in the intermediate state also supports X-ray irradiation. Furthermore, recent optical and near-infrared spectroscopic observations at the soft state suggest that the irradiation might be enhanced due to a larger illumination area provided by a warped disk, and/or the winds launched at large radii of the accretion disk that up-scatter part of the X-ray and/or UV emission (Rahoui et al., 2012).

3.4.3 Rebrightening due to a jet?

The occurrence of OIR rebrightening in the hard state decay is similar to those observed in other black hole binaries 4U 1543-47 (Buxton & Bailyn, 2004; Kalemci et al., 2005), XTE J1550-564 (Jain et al., 2001; Russell et al., 2010), and XTE J1752-223 (Russell et al., 2012). Such a rebrightening has also been observed in 2003, 2005, and 2007 hard state decays of GX 339-4 (Coriat et al., 2009; Buxton et al., 2012). In all these cases, the rebrightening occurs at an X-ray luminosity range of 0.08–2% L_{Edd} (E. Kalemci et al., in preparation). 4U 1543-47 (Park et al., 2004), XTE J1550-564 (Corbel et al., 2001), and XTE J1752-223 (Miller-Jones et al., 2011) have shown radio revival sometime during the rebrightening, but the coverage for these cases were not adequate to describe radio behavior during the OIR rise. For 4U 1543-47, XTE J1550-564 and XTE J1752-223, the SED of the excess during the rebrightening has indicated a clear negative slope which is consistent with the optically thin synchrotron emission from a compact jet, and an extrapolation from radio to OIR matches well with flat or slightly inverted spectral slopes. GX 339-4 during the rebrightening in the 2005 hard state decay showed similar radio–OIR SEDs (Coriat et al., 2009). Note that rebrightening in the hard state decay of GX 339-4 in 2011 is also associated with radio revival (S. Corbel, private communication¹), hence it is natural to assume that the rebrightening has jet origin.

3.4.4 Understanding the broadband SEDs

We have produced two broadband SEDs from the rise and the peak of the rebrightening. Unlike 4U 1543-47 and XTE J1550-564 for which a clear negative slope is present, our baseline–subtracted SEDs indicate a flat to slightly inverted spectrum (see Figure 3.7). Assuming that the excess is from the jet, we tried to obtain the break frequency for the change from an optically thick to an optically thin synchrotron emission, which is an important parameter in determining the base radius of the jet, magnetic field and minimum total jet power (Fender, 2006).

¹Later published in Corbel et al. 2013b

The flat SEDs may indicate that all OIR points lie on the optically thick part. In this case, the break is around the V band, or at a higher frequency, which places a constraint on the slope of the optically thin synchrotron emission. A power-law fit from the V band that passes through the softest X-ray band would give the spectral slopes of $\alpha = 0.72 \pm 0.03$ and $\alpha = 0.95 \pm 0.03$ for MJD 55,609.84 and 55,617.53, respectively (the dot-dashed lines in Figure 3.7). These slopes are a lower limit to the possible absolute slopes that do not provide X-ray fluxes higher than the observed ones. The former is a typical spectral slope expected from an optically thin synchrotron jet emission, but the latter is above the given range $0.6 \lesssim \alpha \lesssim 0.8$ (Russell et al., 2012) depending on the lepton energy distribution. If the spectral slopes as steep as 1.5 for XTE J1550-564 (Russell et al., 2010) and XTE J1752-223 (Russell et al., 2012) are possible at the beginning of the OIR rebrightening, then the particle distributions inferred from SEDs would not be problematic.

If the break is at the V band, however, the ratio of the minimum integrated synchrotron power to the X-ray luminosity is $L_j/L_{1-200 \text{ keV}}=0.18$ and 0.95 for the SEDs on MJD 55,609.84 and MJD 55,617.53, respectively. For this calculation, we considered only the optically thick part of the SEDs and assumed a conservative jet radiative efficiency of 0.05 following (Corbel & Fender, 2002). The reported ratios for GX 339-4 are in between 0.05 and 0.10 (Corbel & Fender, 2002) and the maximum value reported so far is for XTE J1118+480 which is 0.20 (Fender et al., 2001). The ratio of 0.95 is too high to be accounted for scale-invariant jet models (Markoff et al., 2005). The ratio decreases down to 0.32 for a break at the H band for this observation, and 0.05 for the observation on MJD 55,609.84. The typical break frequencies reported so far for GX 339-4 are in the mid-infrared (Gandhi et al., 2011) to infrared range (Corbel & Fender, 2002; Coriat et al., 2009; Homan et al., 2005a; Buxton et al., 2012).

On the other hand, if we place the break at the H band or at a lower frequency, we encounter a problem with a simple post-shock emission model. In Figure 3.7, the dashed lines show the limiting cases of the power laws that can be fitted from the H band to softest X-ray band. The other three OIR bands remain significantly above the power law even when the errors are considered. This shows that the entire excess SED cannot be explained by optically thin synchrotron emission from a jet. Coriat et al. (2009) have studied SEDs from a similar stage of the hard state decay and claimed that significant reprocessing may be present during the OIR rebrightening. In this work, we show that even taking out the baseline emission that comes with reprocessing, there is still an excess. If a spectral break occurs at/below the H band, it either must have two components (such as pre-shock synchrotron; Markoff et al. 2003; Homan et al. 2005a) or a simple flat to inverted spectrum breaking in the near- or mid-infrared is not a good description of the jet behavior during its launch. Such an additional component has recently been observed by Rahoui et al. (2012). A full SED fitting (including radio fluxes) that takes into account the emission from different parts of the jet is required to find the break frequency, and this is beyond the scope of this paper.

We also extrapolated a power law (dotted lines) with spectral index obtained from X-ray spectral analysis down to the OIR band. In both days, the power law remained substantially below the OIR. This shows that the X-ray spectra cannot be explained by pure synchrotron emission without assuming a second emission component from the jet, at least during the early part of the OIR rebrightening. X-rays dominated by direct jet emission scenario such as stated in Maitra et al. (2009) are also dismissed in Buxton et al.

(2012). The synchrotron–self–Compton models are also able to explain the broadband nature of jet emission (Markoff et al., 2005; Coriat et al., 2009). However a detailed analysis of such models is beyond the scope of this paper.

3.4.5 On the modulations of the OIR light curves

We have found that the OIR light curves on the rise of the rebrightening are modulated with the binary period of the system (~ 1.77 days). This can be explained with the X-ray irradiation of the secondary star by the hard photons originating from the corona. Then, we need to explain why we do not detect variations with the binary period before the rebrightening, and after the peak of the OIR light curve. Between MJD 55,580 and 55,605 (before the rebrightening), the power-law flux is relatively high, however, the spectral indices are still high. During this time, the size of the corona may be relatively small, and therefore cannot illuminate the secondary star effectively while still effectively illuminating the warped disk. During this time, variations in the OIR flux from the disk is larger than the variations with the binary period. When the corona becomes larger, as indicated by the changes in the spectral index and the flux, it not only illuminates the secondary star effectively but also allows the magnetic flux to travel close to the black hole, aiding in the launch of the jet (Meier, 2001; Beckwith et al., 2009). At the peak, the lack of modulations with the binary period is most likely due to the strongly variable jet synchrotron (Rahoui et al., 2012) dominating the emission in all bands. After the peak, the X-ray power-law flux decreases so much that it cannot produce significant irradiation on the surface of the secondary star. In Figure 3.4, the decrease in the X-ray power-law flux after MJD 55,607 is accompanied by a decrease in the amplitude of variations in the V band which is in favor of X-ray irradiation of secondary star.

CHAPTER 4

Accretion–Jet process and X-ray variability

4.1 Introduction

In the following, we focus on the evolution of the broad noise components and narrow quasi-periodic oscillations identified in the Fourier power spectra of GBHTs during outburst decays. We compare them to the X-ray spectral properties and also to the infrared and/or radio emission properties to understand the relation between the jets and the short term X-ray variability properties. In particular, we i) seek for the changes in the X-ray timing properties during the jet turn on, ii) seek for the differences in the X-ray timing properties of sources that are separated into two groups in the radio–X-ray luminosity relation (‘standard’ and ‘outlier’ track), iii) evaluate the predictions of the MDAF theory (see Section 1.4.3.4). For this purpose, we use a large sample of GBHTs observed with *RXTE* in X-rays, SMARTS in IR, and in radio. The sample includes the outburst decays of 4U 1543–47 in 2002, GRO J1655–40 in 2005, GX 339–4 in 2003, 2005, 2007, 2011, H 1743–322 in 2003, 2008, 2009, XTE J1550–564 in 2000, XTE J1720–318 in 2003, and XTE J1752–223 in 2010. The results of this study has been turned into an article submitted to ApJ. This submitted article is complimentary to Kalemci et al. (2013) that discusses the changes in X-ray spectral properties as the compact jets form.

4.2 Data analysis

4.2.1 Spectral analysis

The spectral information is directly taken from Kalemci et al. (2013). We use PCA in the 3–25 keV band and HEXTE in the 15–200 keV band and fit the spectra together. However, we do not include HEXTE data if the background-subtracted 20–100 keV count rate in cluster A is less than 3 cts/s. Also, HEXTE data were not used after cluster B stopped rocking on December 14, 2009. For PCA we use all of the available PCUs for all observations and include systematic errors at a level of 0.8% up to 7 keV and 0.4% above 7 keV.

For all sources, the HEXTE background fields are checked using HEXTEROCK utility and compared to Galactic bulge scans. Only fields not contaminated with sources or strong background are used. HEXTE background are corrected for deadtime (Rothschild et al., 1998).

All the X-ray spectra are fitted with a uniform model that consists of an photo-electric absorption, a multicolor disk black body and a power law. A smeared edge model (Ebisawa et al., 1994) is also included to account for the residuals due to iron K_{α} absorption edge seen around 7.1 keV. In the spectral fits, the smeared edge width is fixed at 10 keV and the hydrogen column density is fixed at the values found in literature. For each observation, we introduce high energy cut-off to the model and check the improvement in the fit using F-test. If the chance of probability becomes less than 0.001, we include the cut-off in the fit.

We calculated the Eddington flux for each source. If necessary, we extrapolated our X-ray spectra to the 3-200 keV band using the spectral fits and defined the Eddington Luminosity Fraction (ELF) as the ratio of 3-200 keV flux to the Eddington flux of each source. This method underestimates the actual ELF because we are not calculating the bolometric luminosity. There are also some uncertainties coming from the extrapolation of the X-ray spectrum to 3-200 keV when HEXTE is not used. However, given the large uncertainties in mass and distance and also since the total energy budget should be dominated by X-rays, these uncertainties do not affect our results significantly.

4.2.2 Temporal analysis

For each observation, a Fourier power spectrum is calculated with a time resolution of 2^{-11} s (a Nyquist frequency of 1024 Hz) in the 3–25 keV energy band. Since all the features shift to lower frequencies in the power spectra as the flux decays, we use short (16 s) segments at higher flux levels and progressively increase the segment lengths to 128 s as the outburst decays to minimize error. The power spectra are normalized as in Miyamoto & Kitamoto (1989). The dead time effects are corrected using the model of Zhang et al. (1995) with a dead time of 10 μ s per event. For observations longer than one orbit, we split the data into single *RXTE* orbits and apply the whole PSD calculation process for each orbit.

Following Belloni et al. (2002), we fit all the power spectra by a number of Lorentzian components. To limit the number of Lorentzians in the model, we only keep the components whose inclusion gives a 3σ improvement of the fit according to an F-test. The Lorentzian components are described by their peak frequency $\nu_{max} = (f_0^2 + \Delta^2)^{1/2}$, where f_0 is the centroid frequency, Δ the HWHM, and by their quality factor ($Q \equiv f/2\Delta$). Lorentzians with $Q > 2$ are denoted as quasi-periodic oscillations (QPOs) and those with $Q < 2$ noise. In order to determine the fractional rms amplitude of variability, the Lorentzian profiles are integrated over 0– ∞ Hz range. To eliminate the reduction in the rms amplitudes by the Galactic ridge emission, the rms amplitudes are multiplied with a factor $\frac{T}{T-(B+R)}$, where T is the total count rate, B is the background rate and R is the rate due to Galactic ridge emission (Berger & van der Klis, 1994).

4.2.3 Transitions

During the transition from the soft state toward the hard state, the X-ray spectral and temporal properties of GBHTs show certain changes (Kalemci et al., 2006b, 2008b). One of these changes, the ‘timing’ transition, is a sharp increase in the total rms amplitude of variability often accompanied with an increase in the power-law flux (Kalemci et al.,

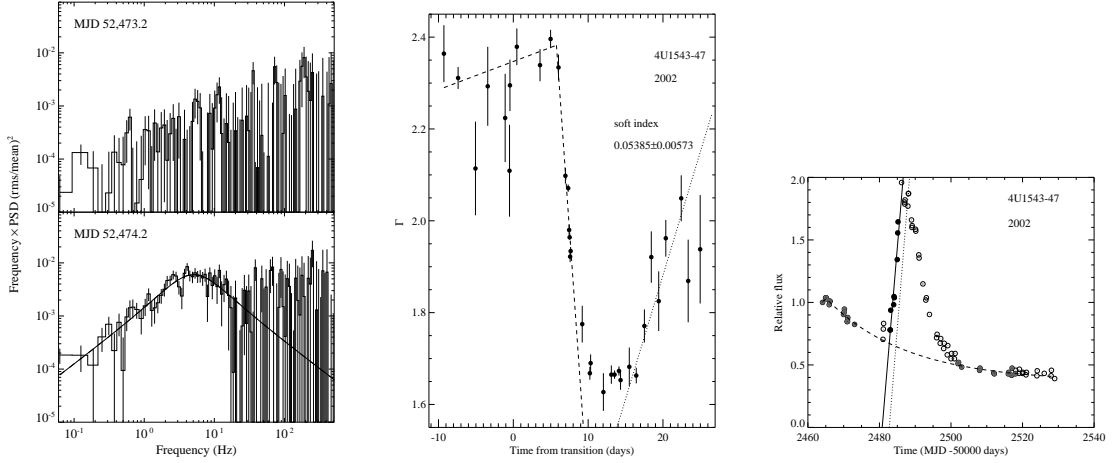


Figure 4.1 The changes that marks the timing (left), index (middle), and IR (right) transitions for 4U-1543–47. Figures are directly taken from Kalemci et al. (2013).

2004). Another change, the ‘index’ transition, is a significant hardening of the power-law component. Additionally, we define the start of the jet activity as a third transition as observed from the radio and IR activity. These transitions help us to characterize outburst decay evolution. In the following sections, we determine the date of the transitions for each outburst decay. The dates of all the transitions are tabulated in Table 4.1. An explicit form of the transitions and how they are determined are shown in Figure 4.1 for 4U 1543–47.

4.2.3.1 Timing transition

The identification of the timing transition in eight outburst decays, namely, 4U 1543-47, GX 339-4 (2005, 2007), GRO J1655-40, H 1743-322 (2003, 2008), XTE J1720-318, XTE J1752-223, is straightforward. It is based on a change from a featureless, Poisson noise-dominated PSD with only a few percent rms amplitude of upper limit to a PSD showing well defined broadband variability, and is determined by the middle of the dates of the two observations.

For the rest of the outburst decays, the identification of the timing transition is not as straightforward although depends on an increase in the rms amplitude of variability. Below we explain each case.

GX 339–4 (2003): The spectral and temporal analysis of the entire outburst is reported in Belloni et al. (2005). During the outburst decay, instead of monotonous hardening of the spectrum, the source goes hardened, softened and hardened again. The variability of the source shows a correlation with this spectral evolution, disappears at softer times and comes back at harder times. We mark the date that the variability enters to a monotonously increasing trend as timing transition at MJD 52,717.8.

GX 339– (2011): During the transition from the soft state toward the hard state, there are occasional detections of type-B QPOs sprinkled among the Poisson noise-dominated PSDs with only upper limits. We mark the timing transition at MJD 55,594 which corresponds to a change from a PSD with type-B QPO to a PSD showing well defined broadband variability. From this date on, the variability monotonously increases.

H 1743–322 (2009): The spectral and timing analysis of the entire outburst is reported in Motta et al. (2010). The variability never drops to detection level of the RXTE while the source was in the soft state. During the outburst decay, the rms amplitude of variability sharply increased from 12.9 to 16.9% between MJD 55,013.09 and 55,016.32 and a type-C QPO is detected. Based on these changes we mark the timing transition at MJD 55,014.7.

XTE J1550–564 (2000): The timing analysis of the entire outburst is reported in Rodriguez et al. (2004). Similar to H 1743–322 (2009), the variability never drops to detection level of the RXTE while the source was in the soft state. We mark the timing transition at MJD 51,674 because the rms amplitude of variability changes from a constant 10% level to a monotonously increasing trend.

4.2.3.2 Index transition

GBHTS during outburst decay harden quite rapidly from photon index ~ 2 to ~ 1.6 over a timescale of ~ 10 days. A sample evolution can be seen in Figure 4.2. We define the index transition as the start of the hardening. It is determined by the intersection point of two linear lines obtained from fitting the constant and decaying parts. We adopt their values given in Kalemci et al. (2013).

4.2.3.3 Radio and/or IR transition

We only have IR light curves of 4U 1543–47, GX 339–4 and XTE J1550–564. We define the IR transition as the start of the flaring in the infrared (IR) light curves. To determine the date of the IR transition, we fit the non-flare part of the light curve with an exponentially decay and the rise of the brightening with a linear line, then take the intersection point of the two curves. Such a modeling of the non-flare part of the light curve with an exponential decay is common in the literature (Kalemci et al., 2005; Russell et al., 2010; Dincer et al., 2012; Chun et al., 2013). We note that some arbitrariness exists in this method as the points to fit at the IR flare, and for the baseline are chosen by eye. Additionally, as discussed in Buxton et al. (2012), baseline before and after the flare might have an offset, and a single exponential may not fit all points. Despite these potential problems in the method, trying different group of points for the baseline, omitting the part of the baseline after the flare (for GX 339-4 in 2007, IR peak do not decay for more than 100 days, therefore we only used the data before the rise), or using slightly different group of points for the rise change the start time at most by a day.

For the definition of the radio transition we make use of the evolution of the flux densities and the radio spectral index if multiband observations are available. We define two radio transitions: i) the time of first radio detection of the source around the time when the source makes a transition from soft to hard state, and ii) the time of first optically thick radio spectrum. Such a distinction is made to deal with the sparse radio data. The radio transition of each outburst decay is discussed below.

XTE J1720–318: Its radio coverage with ATCA and VLA is reported in Brocksopp et al. (2005). There are a number of non-detections in the soft state. The first detection of the source is only at 4.8 GHz with a flux density of 0.34 ± 0.08 mJy on MJD 52,728.6 during the transition from the soft state to the hard state.

GRO J1665–40: There are two non-detections on MJD 53,630 and 53,631. The first detection is on MJD 53,634. The flux densities at 4.8 and 8.6 GHz result in a spectral index of $\alpha = 0.27 \pm 0.76$. Since the errors are large, it is not possible to make a distinction between an optically thin and optically thick spectrum.

XTE J1752–223: The radio core of the source is detected for the first time on MJD 55,311 in VLBI images (Miller-Jones et al., 2011). There are also frequent ATCA observations of this source at 5.5 and 9 GHz (Brocksopp et al., 2013). The ATCA observations show an optically thin radio spectrum and an excess emission during the VLBI core detection, indicating a contribution from an unresolved extended emission. During the radio core detection, there is also an excess emission in the optical light curve of the source (Chun et al., 2013).

H 1743–322: McClintock et al. (2009) reported the VLA radio observations of its 2003 outburst decay. The source is not detected in the soft state. The first detection is on MJD 52,940 during the transition from soft to hard state. The flux densities at 4.8 and 8.6 GHz result in a spectral index of $\alpha = -0.72 \pm 0.72$. This does not allow us to make a distinction between an optically thin or optically thick spectrum. In the second detection, on MJD 52,948, the spectral index is consistent with an optically thick spectrum ($\alpha = 0.81 \pm 0.87$).

During its 2008 decay, the source is observed many times with the VLA (Jonker et al., 2010). At the beginning of the outburst decay, between MJD 54,484 and 54,487, the radio flux densities at 4.86 and 8.46 GHz are higher than 0.6 mJy, and all the radio spectra are optically thin. A single ATCA observation on MJD 54,493 results in a non-detection with an upper limit of 0.15 mJy at 4.8 and 8.6 GHz (Kalemci et al., 2008a). After the ATCA non-detection, there are further detections of the source with the VLA. Between MJD 54,499 and 54,505, the radio spectral index is $\alpha = 0.03 \pm 0.18$ (Jonker et al., 2010). Again due to the large errors, it is not possible to make a distinction between an optically thin and optically thick spectrum.

The radio jet turn on during the 2009 outburst decay of H 1742–322 is broadly discussed in Miller-Jones et al. (2012). The source is continuously detected in the soft state. The nature of this radio emission is attributed to the external shocks as the jets interact with the surrounding medium. Between MJD 55,012 and 55,019, the radio data show a brightening and the authors associate this with the compact jet turn on.

4.3 Results

For each outburst decay, the evolution of the peak frequencies of the Lorentzians, the total rms amplitude of variability, and the QPO rms amplitude variability as well as the power-law and disk fluxes, the photon index (Γ) and the radio and/or IR data are shown in Figure 4.2. The Lorentzian components identified in each observation are distinguished from each other with different plotting symbols. In increasing frequency order, L_1 is shown with circle, L_2 with square, L_3 with diamond and L_{qpo} with empty diamond. The single Lorentzians are not classified and they are shown with cross. The observations before the timing transition are shown with turquoise color, the observations between the timing and the index transitions are with green, observations between index transition and the thick radio transition with blue, and after the thick radio transition with pink. The

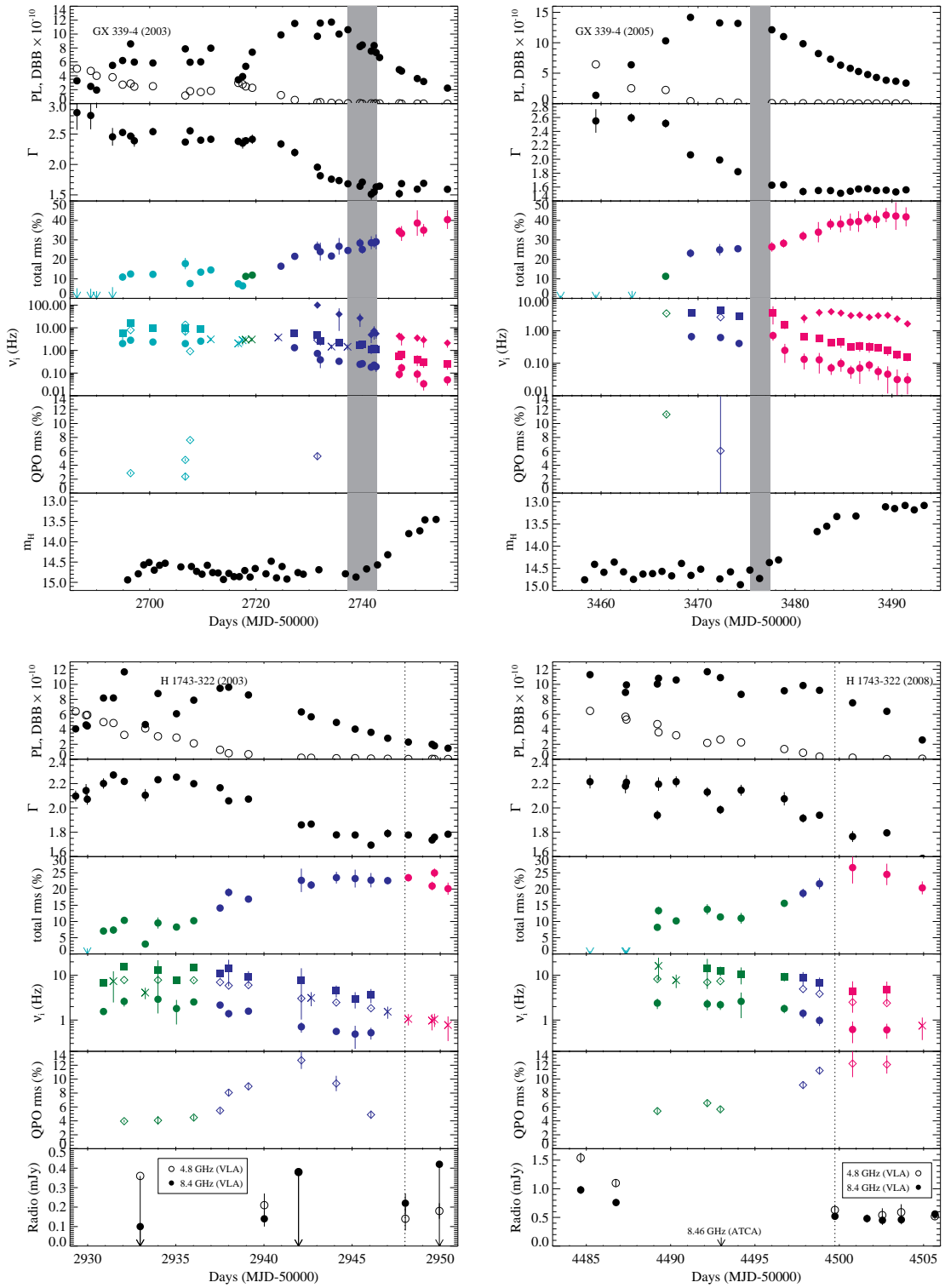


Figure 4.2 (a-d) Evolution of the X-ray power spectral parameters along with the IR and/or radio information for all the outburst decays.

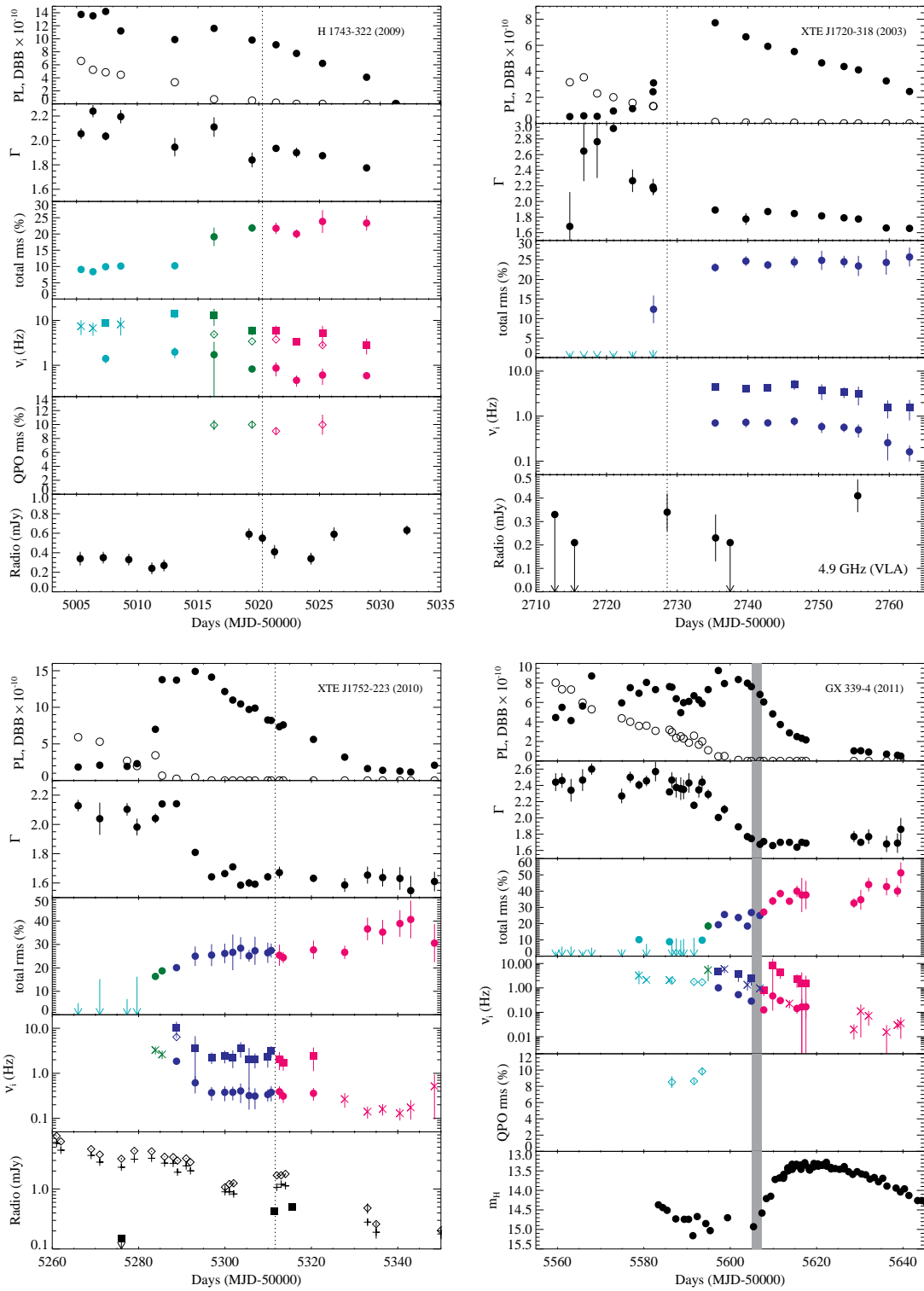


Figure 4.2 – continued (e-h) Evolution of the X-ray power spectral parameters along with the IR and/or radio information for all the outburst decays.

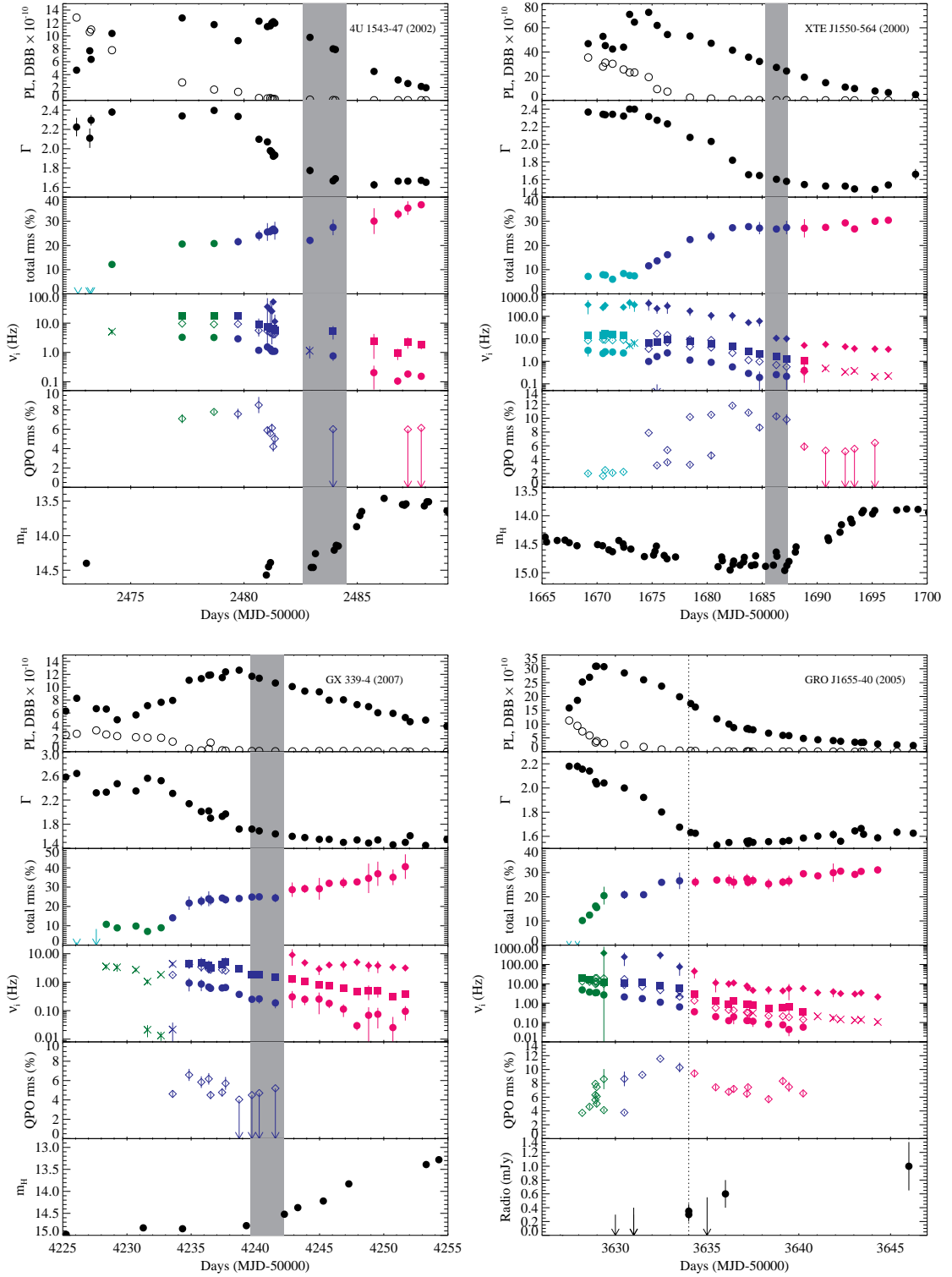


Figure 4.2 – continued (j-m) Evolution of the X-ray power spectral parameters along with the IR and/or radio information for all the outburst decays.

Table 4.1. Transition times of GBHTs during outburst decay

Source	Year	Timing (MJD-50000)	Index (d)	IR (d)	Radio	
					First ^a (d)	Thick ^b (d)
GX 339–4	2003	2717.8 ± 0.3	6.6 ± 0.3	22.2 ± 2.8
GX 339–4	2005	3464.9 ± 1.8	1.8 ± 0.7	11.5 ± 1.0	< 15.8	< 15.8
GX 339–4	2007	4228.0 ± 0.4	5.0 ± 0.3	12.9 ± 1.3	< 23.7	< 23.7
GX 339–4	2011	5594.0 ± 0.7	2.2 ± 0.5	12.2 ± 1.1	4.9	16.1
4U 1543–47	2002	2473.7 ± 0.5	5.7 ± 0.4	9.9 ± 1.0	< 13.3	< 16.3
XTE 1550–564	2000	1674.0 ± 0.6	0.6 ± 0.4	12.3 ± 1.0
XTE J1752–223	2010	5282.1 ± 2.1	3.7 ± 0.9	...	0.0	< 29.4
GRO J1655–40	2005	3628.1 ± 0.1	1.3 ± 1.1	...	< 5.9	< 5.9
H1743–322	2003	2930.4 ± 0.5	5.7 ± 0.2	...	< 9.6	< 17.6
H1743–322	2008	4488.3 ± 0.9	8.8 ± 0.6	...	< 11.4	< 14.3
H1743–322	2009	5014.7 ± 1.6	9.0 ± 1.0	...	< 0	< 11.5
XTE J1720–318	2003	2726.6 ± 0.0	-5.0 ± 1.0	...	< 2.0	< 28.9

Note. — Index, IR and radio transitions are given relative to timing transition.

^afirst radio detection

^bfirst flat/inverted spectrum

dashed vertical line shows the date of first radio detection of jet.

In the following, we characterize the evolution of the peaks, look for the changes in the properties of the Lorentzians across the IR and radio transitions, and also investigate bilateral relations between the X-ray spectral and temporal parameters.

4.3.1 Evolution of the peak frequencies

The most noticeable result in the evolution of all peak frequencies is their eventual decreasing trend. This decreasing trend is a well known characteristic of the GBHTs during outburst decay (e.g. Kalemci et al., 2003; Klein-Wolt & van der Klis, 2008). However, in eight outburst decays out of twelve (GX 339-4 in 2003 and 2005, 4U 1543-47, H 1743-322 in 2003 and 2008, XTE J1752-223, XTE J1720-318, and XTE J1550-564), the peak frequencies do not decay, instead shows a flat evolution for days to weeks while very little changes are observed in the total rms amplitude.

4.3.2 Changes in the evolution of the L_3

In the time evolution of the peak frequencies (Figure 4.2), the L_3 shows a sharp decrease in its peak frequency (GX 339–4 [2003], XTE J1550–564, GRO J1655–40) or a sudden appearance in the PSD (GX 339-4 [2005,2007], 4U 1543–47) within at most ~ 4 days prior to or following start of the IR rise or the first detection of the optically thick radio emission.

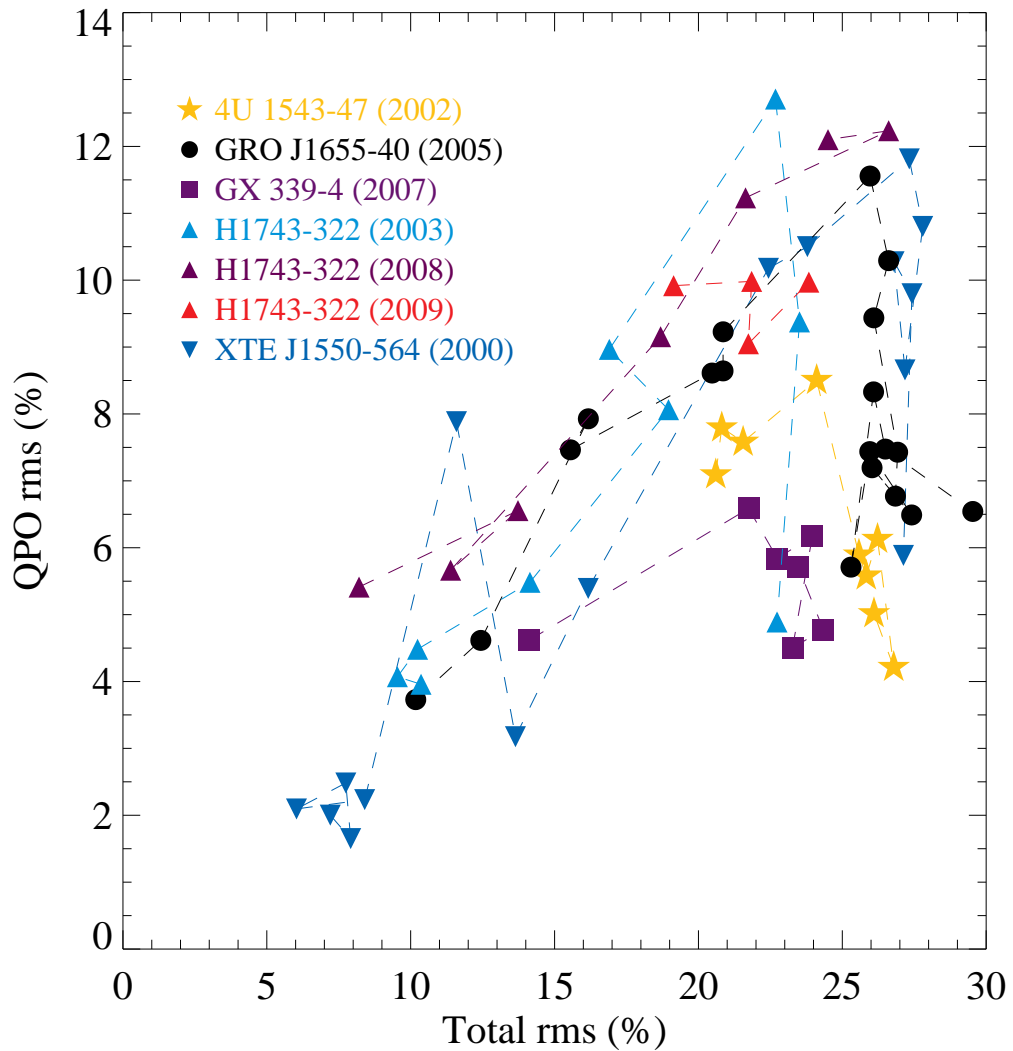


Figure 4.3 The total rms amplitude vs the qpo rms amplitude for all type-C QPOs.

4.3.3 Evolution of the type-C QPOs

Our data set provides a well track of the long term evolution of the type-C QPO (see Figure 4.2). In H1743-322 (2003), GRO J1655-40, XTE J1550-564, the rms amplitude of the type-C QPO first increases, then makes a peak and finally decreases. Its evolution in other outburst decays seem to exhibit only a portion of this trend. For instance, 4U1543-47 shows only the peak and the decrease whereas H1743-322 (2008) shows only the increase and the peak. We also note that the rms amplitude of the QPO decreases within a few days prior to or following the start of the IR rise or the first detection of the optically thick radio emission in H 1743–322 (2003), XTE J1550–564, 4U 1543–47, and GRO J1655–40.

In Figure 4.3, we plot the total against the QPO rms amplitude. At lower total rms amplitude a positive correlation exists between the two parameters, then the QPO rms amplitude of variability decreases whereas the total rms amplitude of variability remains high.

4.3.4 Rms variability: Tracks in the radio-X-ray luminosity relation

Using all *RXTE* observations investigated in this work, we show the total rms amplitude against the photon index, and the ELF in Figures 4.4a and 4.5a, respectively. In this plot, the pink color shows the observations after the IR or optically thick radio transition.

A global relation is observed for all GBHTs. As expected, the spectral indices are soft, and the rms amplitudes are small for observations before the timing transition (turquoise). During the hardening transition the rms amplitudes gradually increase (blue), and after the IR/radio transition the rms amplitudes sharply increase. In Fig. 4.5, we observe that at a few percent of the ELF, the rms amplitudes increase from a few to $\sim 25\%$. As the ELF decreases further, the rms amplitude reaches up to 45%.

When we divide the same data into two groups based on their association to the tracks observed in the radio–X-ray luminosity relation (e.g. see the tracks with the sources in Corbel et al., 2013a), we observe distinct differences in properties of ‘standard’ track, and ‘outliers’ track sources. For the ‘standard’ track sources, the hardening (blue) and IR/radio (pink) group are completely separated from each other: IR rise is always seen after hardening finishes, and it corresponds to a sharp rise in the rms amplitude seen in Figures 4.4b,c. Whereas for the ‘outliers’ track, the distinction is not clear. Except for XTE J1752–223, the rms amplitude approaches 30% and does not exceed this value. This distinction is more clear in Figures 4.5b,c; again except for XTE J1752–223, the rms amplitude almost stays constant below a few % ELF for the outliers, whereas they increase in the ‘standard’ track sources. Therefore the global trends seen in Figs. 4.4a and 4.5a are set by ‘standard’ track sources, but in reality the ‘outliers’ behave differently.

XTE J1752–223 seems to have higher rms amplitude at low flux levels compared to the other sources in the ‘outliers’ track. We must note that low flux observations of this source are strongly affected by the Galactic ridge emission. We have incorporated the effect of ridge emission in the rms amplitude (Chun et al., 2013), however the uncertainty in the ridge emission results in large errors in the rms amplitude. Therefore the high rms values from low luminosity XTE J1752–223 should be regarded with caution.

4.3.5 ν_{QPO} -luminosity relation

MDAF theory predicts a relation between the peak frequency of the QPO and the luminosity for outliers track sources (Meier, 2012). The relation is in the form of $\nu_{QPO} \propto L_X^p$ where ν is the peak frequency of the QPO, L_X the X-ray luminosity and $p = 0.9-1.1$. To test the prediction, we plot the observational data and scaling curves with $p = 1.1$ for various normalizations in Figure 4.6. Since none of the evolutions seem to be steeper than $p = 1.1$, we do not plot the scaling with $p = 0.9$.

The observational relation varies from decay to decay and there is not a complete agreement between the predicted scaling and the outliers track sources. If we take a look at the outliers sources one by one, GRO J1655–40 converges to the predicted scaling at lower luminosities and H 1743–322 (2009) is totally in agreement with the scaling. For the rest of the outliers track sources and the standard track sources, it is not possible to point to a partial agreement with the scaling due to lack of data.

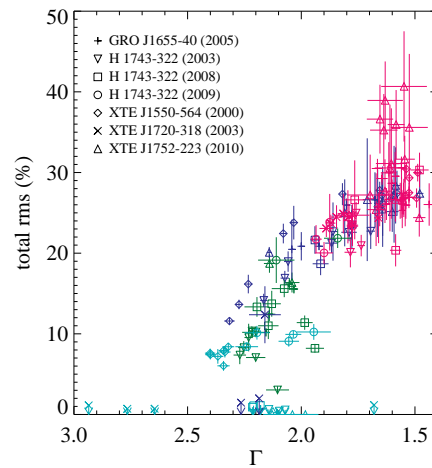
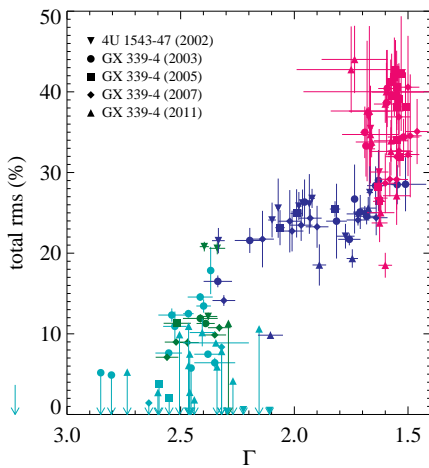
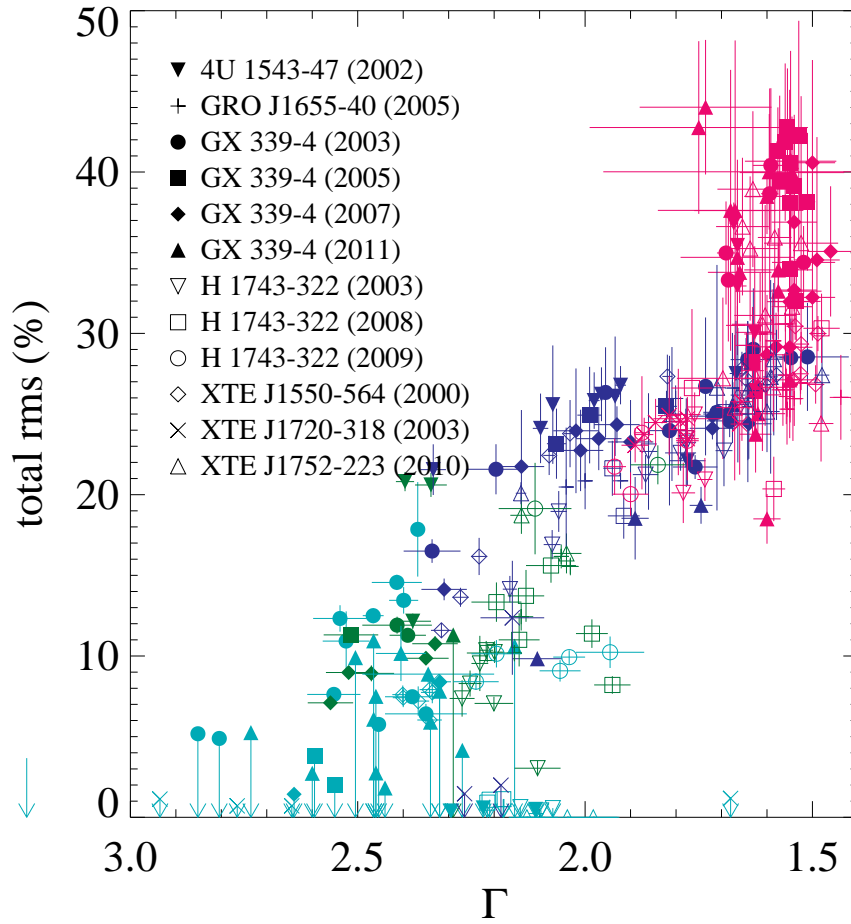


Figure 4.4 Rms amplitude of variability vs photon index (Γ) for a) all the sources, b) the 'standard' track sources, and c) the 'outliers' track sources in the radio-X-ray luminosity diagram.

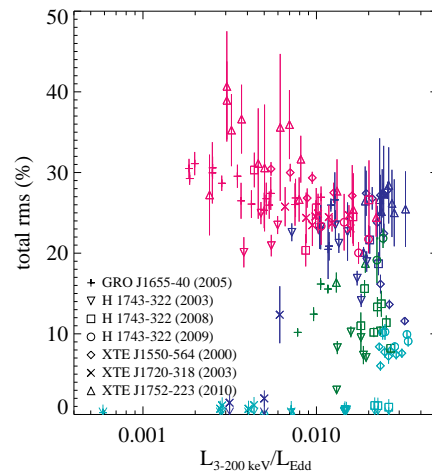
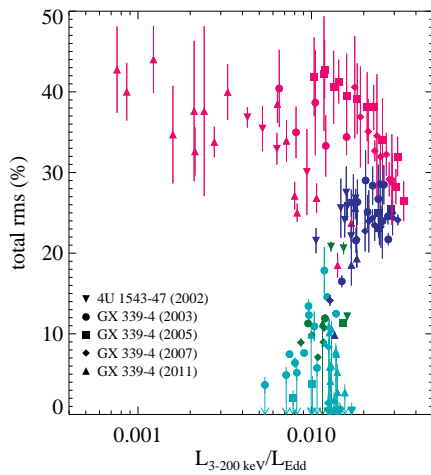
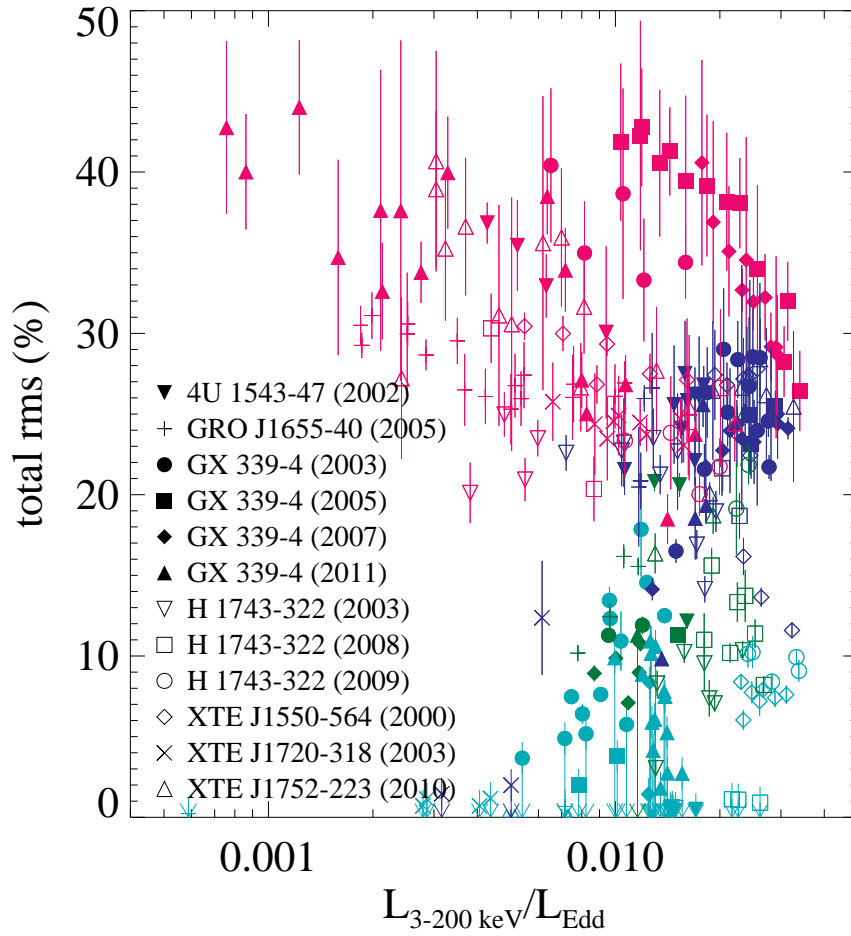


Figure 4.5 Rms amplitude of variability vs Eddington luminosity fraction for a) all the sources, b) the 'standard' track sources, and c) the 'outliers' track sources in the radio-X-ray luminosity diagram.

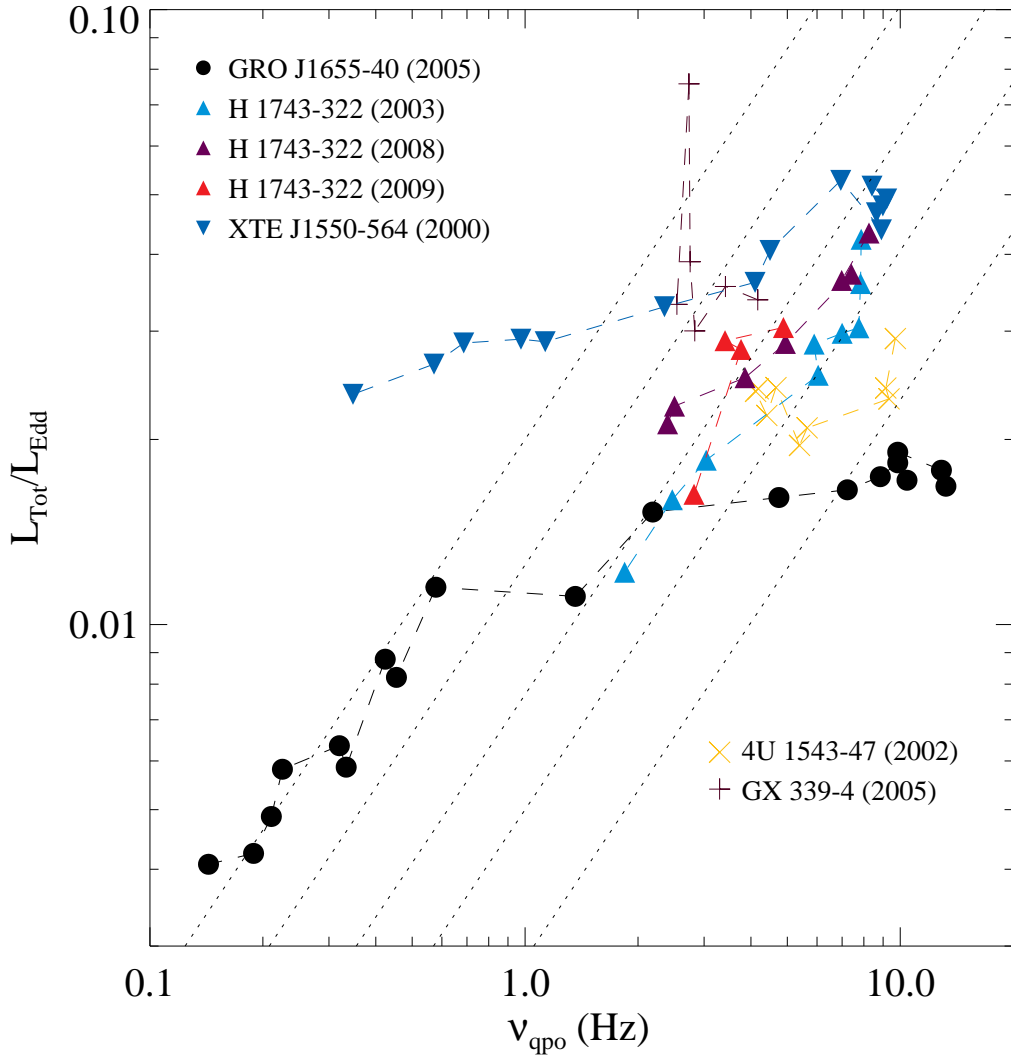


Figure 4.6 Peak frequency of the type-C QPO vs total ELF. Dotted lines show the $\nu_{QPO} = A L_X^{1.1}$ relation for $A = 50, 80, 130, 200, 350$ from top to bottom.

4.4 Discussion

We characterized the overall behavior of the PSD of GBHTs across the changes observed in the radio/IR emission properties during outburst decay. When combined with the spectral information, our results provided a wealth of information for the phenomenological understanding of the accretion-ejection process in GBHTs. In the following we discuss our findings.

4.4.1 Constraining the QPO behavior

When the evolution of the QPOs from all decays are considered together, there might be a global trend: the rms amplitude of the QPO first increases until a peak, then decreases.

This rising part of the rms amplitude is further correlated with the total rms amplitude of variability and while the QPO rms amplitude of variability decreases, the total rms amplitude of variability remains high.

The positive correlation between the QPO and the total rms amplitudes suggests a common mechanism for the evolution of both parameters. A very well known fact, also observed in our results, is that the total rms amplitude of variability increases as the contribution to the total flux from the disk becomes less and the power-law becomes more important. Such a change can be explained assuming if the disk produces Poisson noise and the power-law produces signal (Kalemci et al., 2004). In this case, both the total and the QPO rms amplitudes increase. Recently, Wilkinson & Uttley (2009); Uttley et al. (2011) found that the disk shows significant variability in the hard state. To explain this, they suggest that the variability in the disk is driven by the irradiation of the hard X-rays. In our case, the increase in the total rms amplitude occurs before the sources reach the hard state. Therefore, the hard X-ray emission may not be strong to drive the disk variability, making our explanation consistent with the finding of Wilkinson & Uttley (2009); Uttley et al. (2011).

Yan et al. (2013) found that the decrease in the QPO rms amplitude of variability coincides with the jet growth for GRS 1915+105 and the authors suggested a possible connection between two events. In our sample, the same behavior is seen within a few days prior to or following the start of the IR rise or the first detection of the optically thick radio emission. Although we do not know the mechanisms that produces the jets and the QPOs, the timescale we found support the possibility of a relation between the jet growth and the decrease in the QPO rms amplitude. Depending on the mechanism, the jets may either lower the QPO rms amplitude or completely destroy the QPO mechanism resulting in a non-detection of the QPOs. We note that if there is a destruction of the QPO mechanism by the jet, we are not able to constrain this because the upper limits on the QPO rms amplitudes are large. Such a scenario deserves to be investigated in the future observing campaigns of the black hole transients with large effective and high time resolution telescopes such as LOFT and ASTROSAT.

On the other hand, the decrease in the QPO rms amplitude is independent of the total rms amplitude, suggesting a difference between the two. This difference may be in the mechanisms producing the total and the QPO variabilities. For instance, the broadband variability may be produced via propagating waves in the accretion disk (Lyubarskii, 1997), and amplified in the corona and the QPO may be produced by precession of the corona as in Lens-Thirring mechanism (Ingram & Done, 2011). Such a combination of the mechanisms would also explain the increasing part of the rms amplitudes since both mechanisms depend on the establishment of a strong corona. Alternatively, a QPO produced in the inner regions where jet also operates would also be a viable explanation.

4.4.2 Connection between the radio-X-ray luminosity plane and the broadband X-ray variability

In our large sample, excluding XTE J1752–223, we found that the ‘standard’ track sources exhibit higher total rms amplitude than the ‘outliers’ track sources at a given X-ray luminosity when the jet is present in the hard state. XTE J1752–223 is also consistent with the distinction between the tracks at least down to a luminosity. The observations

indicate that XTE J1752–223 starts in the outliers track at the beginning of the outburst decay (Brocksopp et al., 2013). During this time, the rms amplitude of variability is low, consistent with the behavior of outliers track population. At some point the rms amplitude of variability increases although an ambiguity exists (see Section 4.3.4 for the caveat). If this increase is real then the X-ray variability behavior of XTE J1752–223 resembles the switch from the outliers track to the standard track seen in the radio-X-ray luminosity relation (e.g. H 1743–322 Coriat et al., 2011). The source, indeed, switches to the standard track in the radio-X-ray luminosity relation (Brocksopp et al., 2013). However the observations with higher total rms amplitude of variability (between MJD 55,333 and 55,353) belong to the times when the source is still in the ‘outliers’ track (see Ratti et al., 2012), implying no direct correspondence between the transitions in the two domains. We note that H 1743–322 also makes a transition in the radio-X-ray luminosity plane (Coriat et al., 2011) and we do not see an increase in its rms amplitude of variability. This is due to lack of X-ray variability information since the source count rate is too low to obtain power spectra with high signal to noise ratio at such low luminosities. For this reason, Figure 4.4c and 4.5c do not include H 1743–322 data while it makes a transition to the standard track.

Given the caveat for XTE J1752–223, this is the first distinction in the short term X-ray variability properties of the standard and the outliers track sources. Such a distinction can be explained within the internal shock model framework that is proposed to explain the flat SED of compact jets (Malzac, 2013). In this model, the radio jet luminosity is sensitive to the amplitude of the Lorentz factor fluctuations. These fluctuations of the jet Lorentz factor may be related, in some unknown way, to the fluctuations in the accretion flow and therefore to the X-ray variability. If one naively assumes that the amplitude of the jet Lorentz factor fluctuations is correlated with the X-ray variability amplitude then there may be a positive correlation between the radio luminosity and the rms amplitude of the X-ray variability. However, the relation between the jet and rms amplitude of X-ray variability may be more complex. Also the shape of the PSD may be affecting the relation. In internal shock model, the Lorentz factor fluctuations are assumed to be flicker noise ($P_\nu \propto 1/f$). Different noises would lead to different (non flat) shape of SEDs which can induces in turn large differences in the radio flux for the same integrated X-ray rms.

4.4.3 Evaluating the predictions of the MDAF theory

Meier (2012) suggests that the difference between the slopes of ‘standard’ and the ‘outliers’ tracks can be explained if the thin accretion disk is truncated by the ADAF in the former and in addition to this the ADAF itself is truncated at a radii by the MDAF in the latter. Since the MDAF is a laminar and non-turbulent flow, a high frequency cut-off is expected in the PSD of the outliers sources as opposed to the ADAF only configuration for standard track sources. In our analysis, the PSDs above 10 Hz have large errors. Therefore, we are not able to constrain the variability at higher frequencies. Another prediction of the MDAF theory is that the rotation frequency of the MDAF corresponds to the QPO frequency. However, the QPOs are seen in both track sources, indicating no difference between the standard and the outliers track sources. Finally, to evaluate the scaling between the X-ray luminosity and the QPO frequency, we have to assume that the origin of the QPOs in both track sources must be different. Then, we see that the scaling does not

explain all the outliers track sources.

4U 1543-47 (2002)

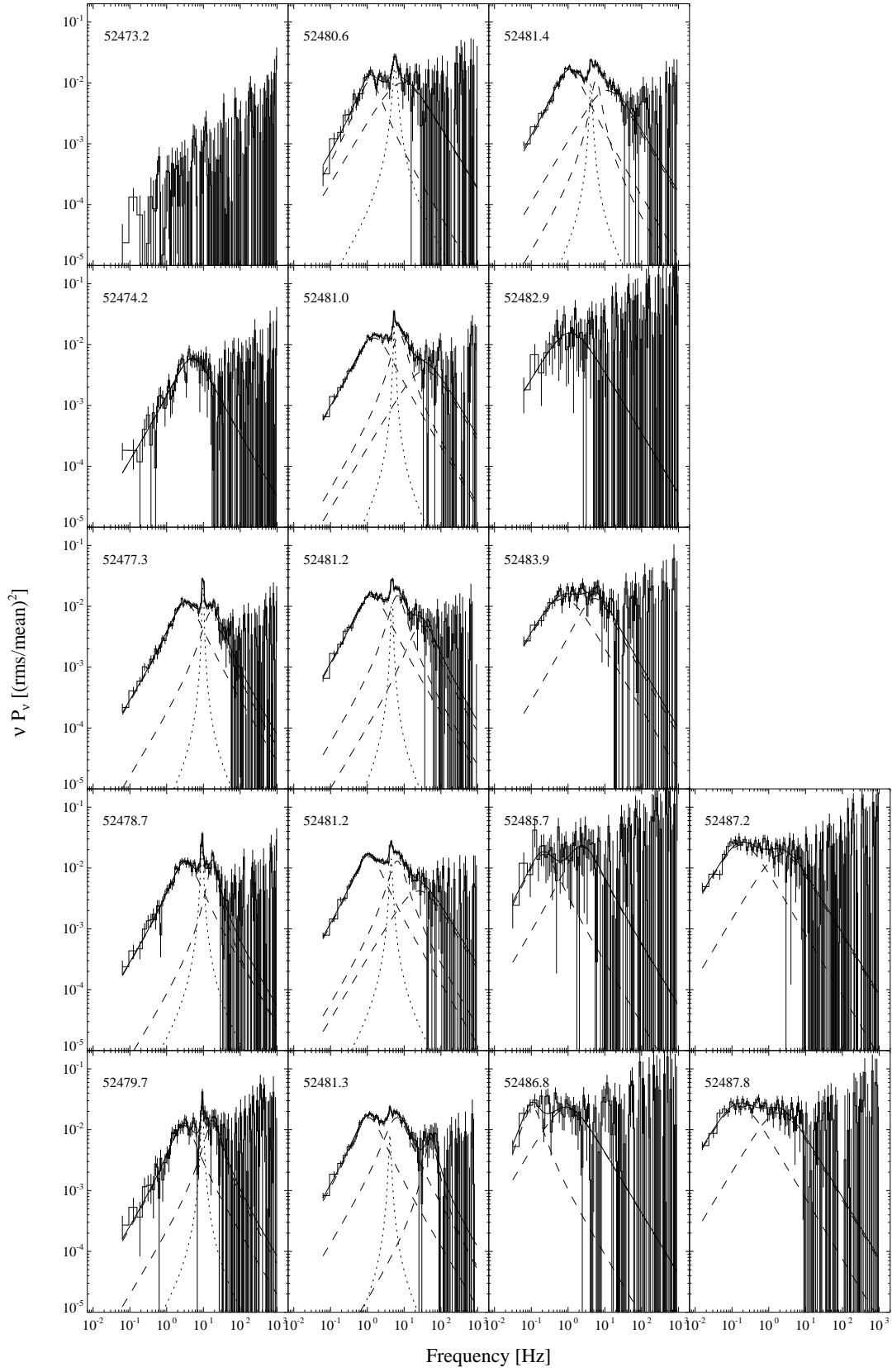


Figure 4.7 Evolution of the PSD modeled with Lorentzians for 4U 1543–47 during its 2002 outburst decay.

H 1743-322 (2003)

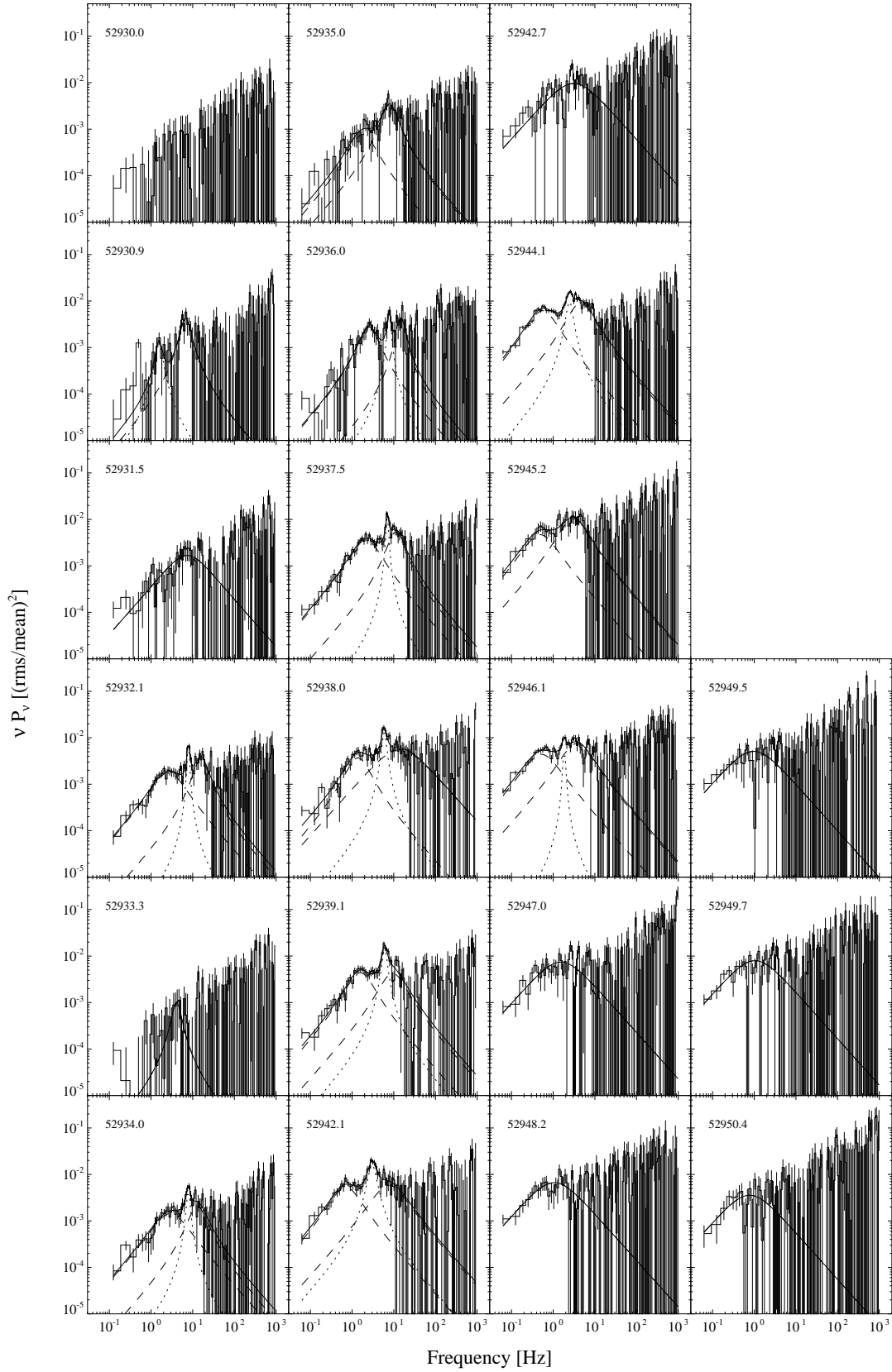


Figure 4.8 Evolution of the PSD modeled with Lorentzians for H 1743–322 during its 2003 outburst decay.

H 1743-322 (2008)

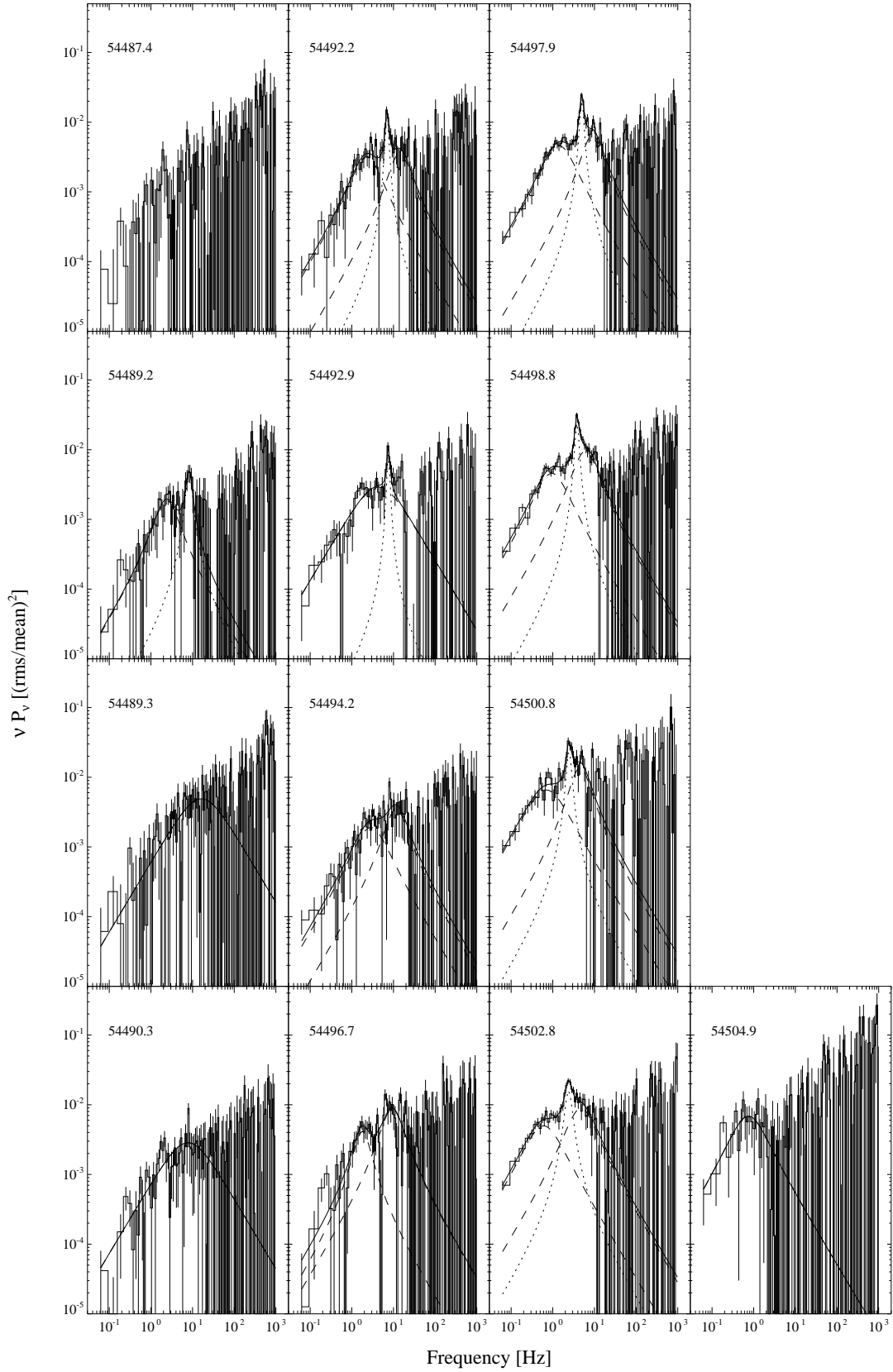


Figure 4.9 Evolution of the PSD modeled with Lorentzians for H 1743–322 during its 2008 outburst decay.

H 1743-322 (2009)

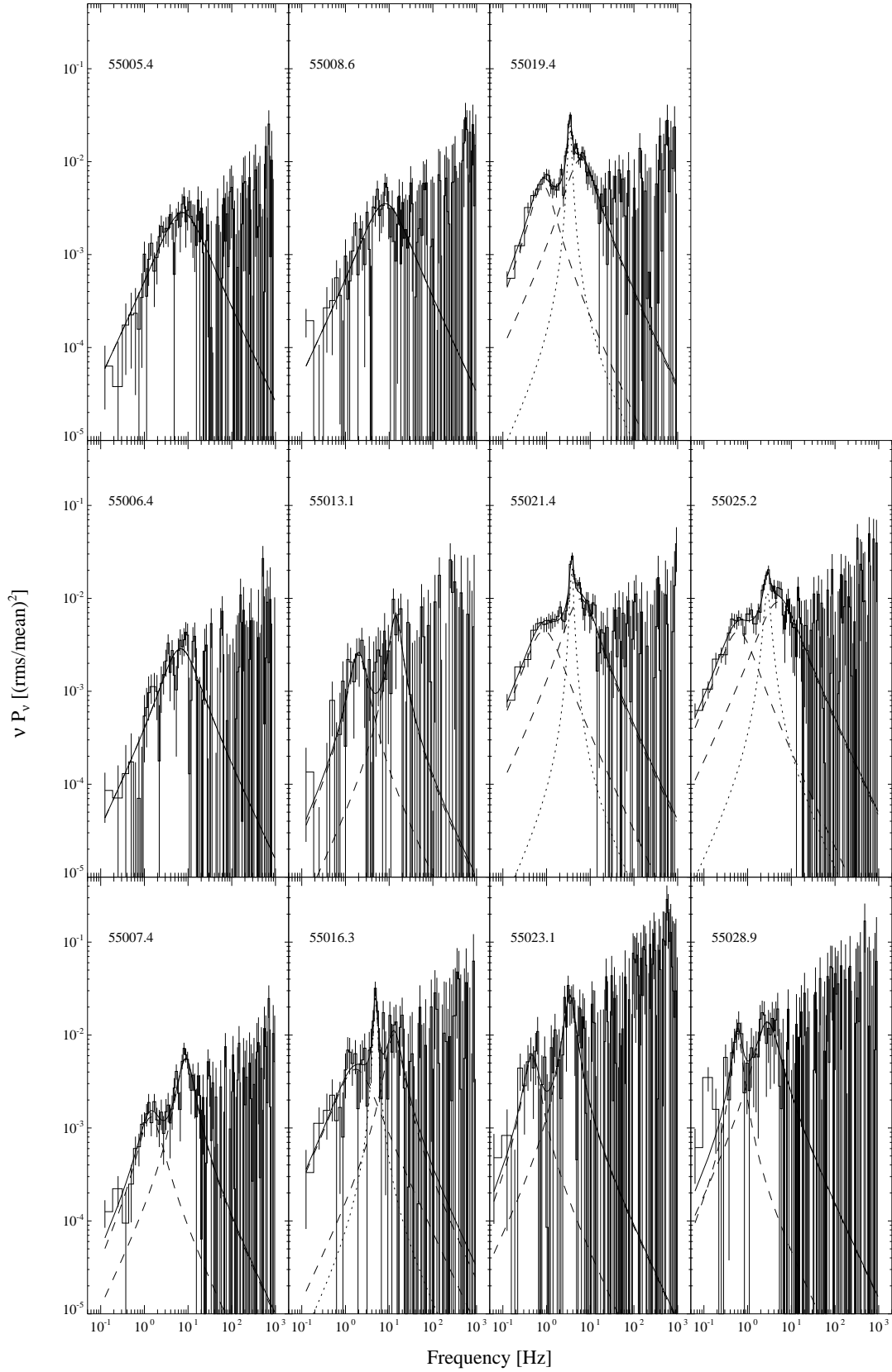


Figure 4.10 Evolution of the PSD modeled with Lorentzians for H 1743–322 during its 2009 outburst decay.

GRO J1655-40 (2005)

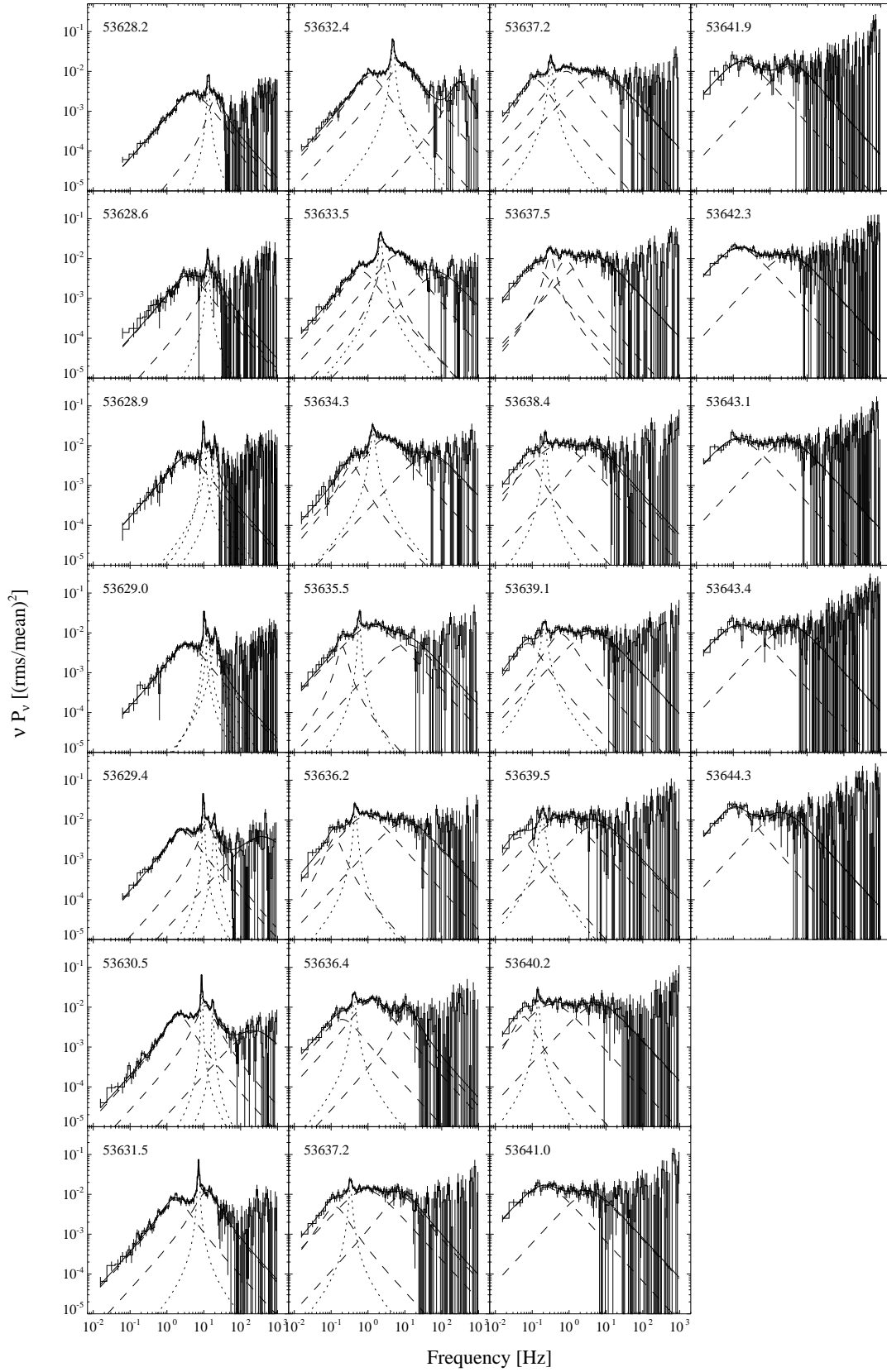


Figure 4.11 Evolution of the PSD modeled with Lorentzians for GRO J1655–40 during its 2005 outburst decay.

GX 339-4 (2003)

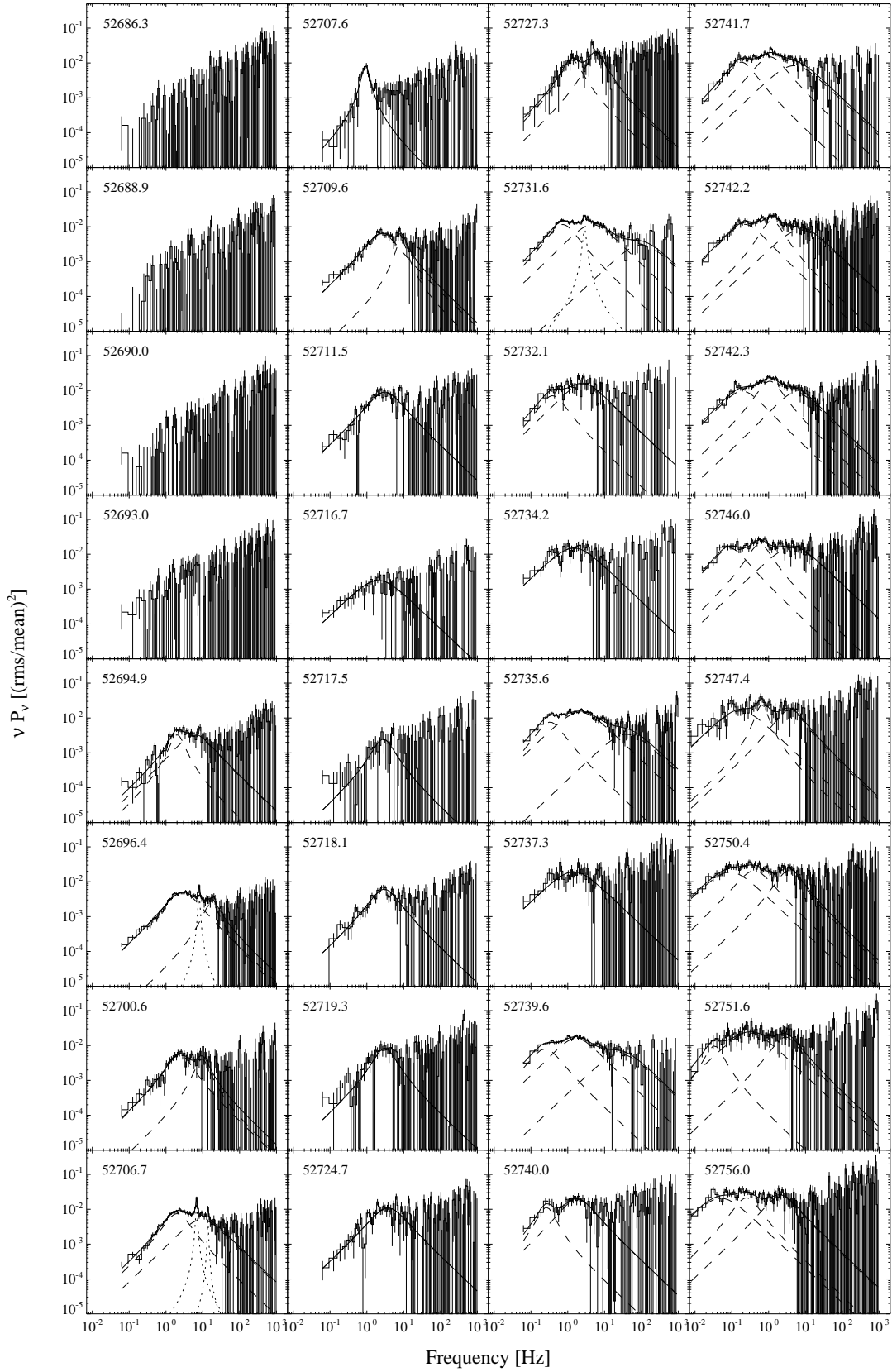


Figure 4.12 Evolution of the PSD modeled with Lorentzians for GX 339–4 during its 2003 outburst decay.

GX 339-4 (2005)

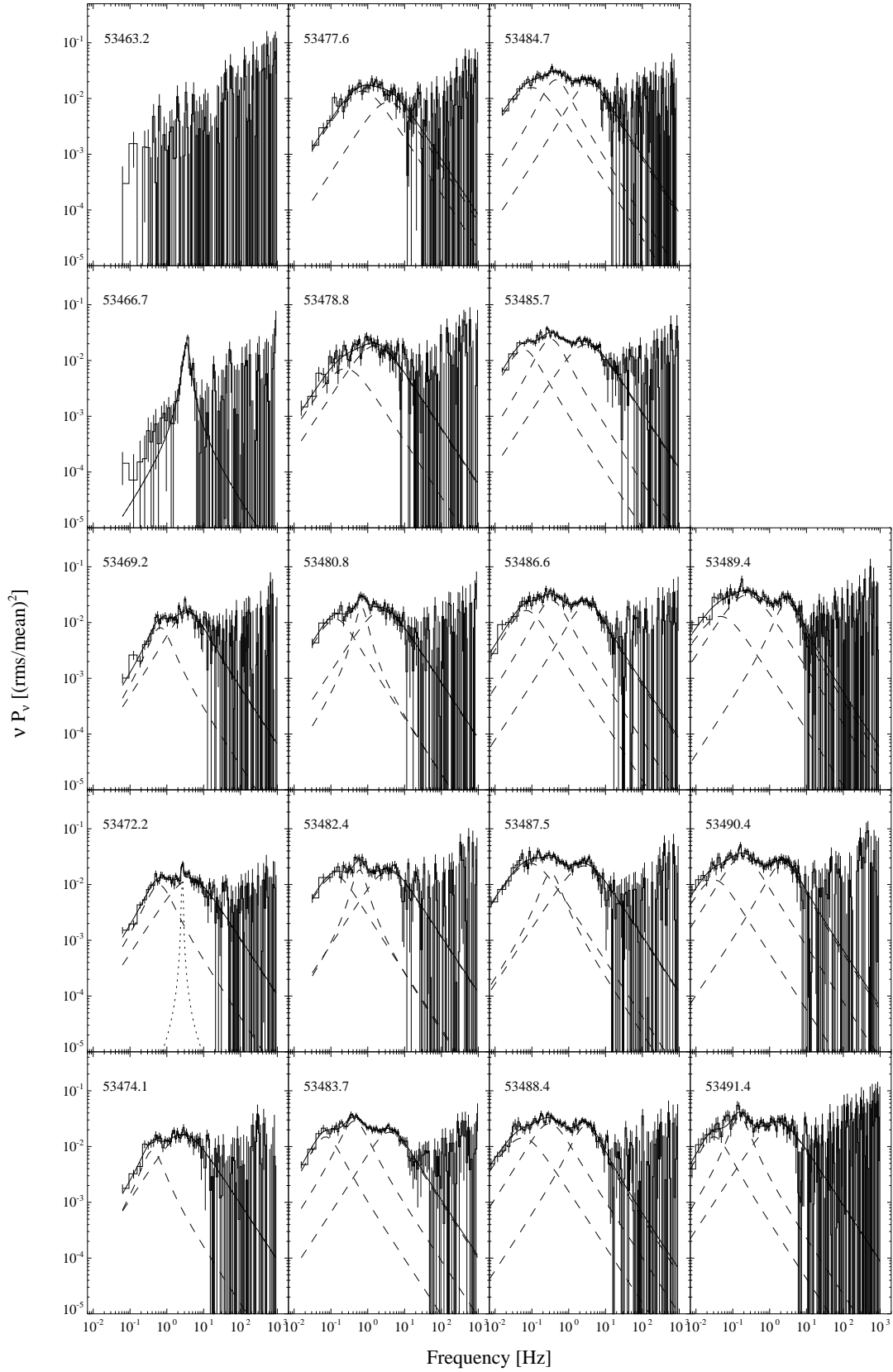


Figure 4.13 Evolution of the PSD modeled with Lorentzians for GX 339–4 during its 2005 outburst decay.

GX 339-4 (2007)

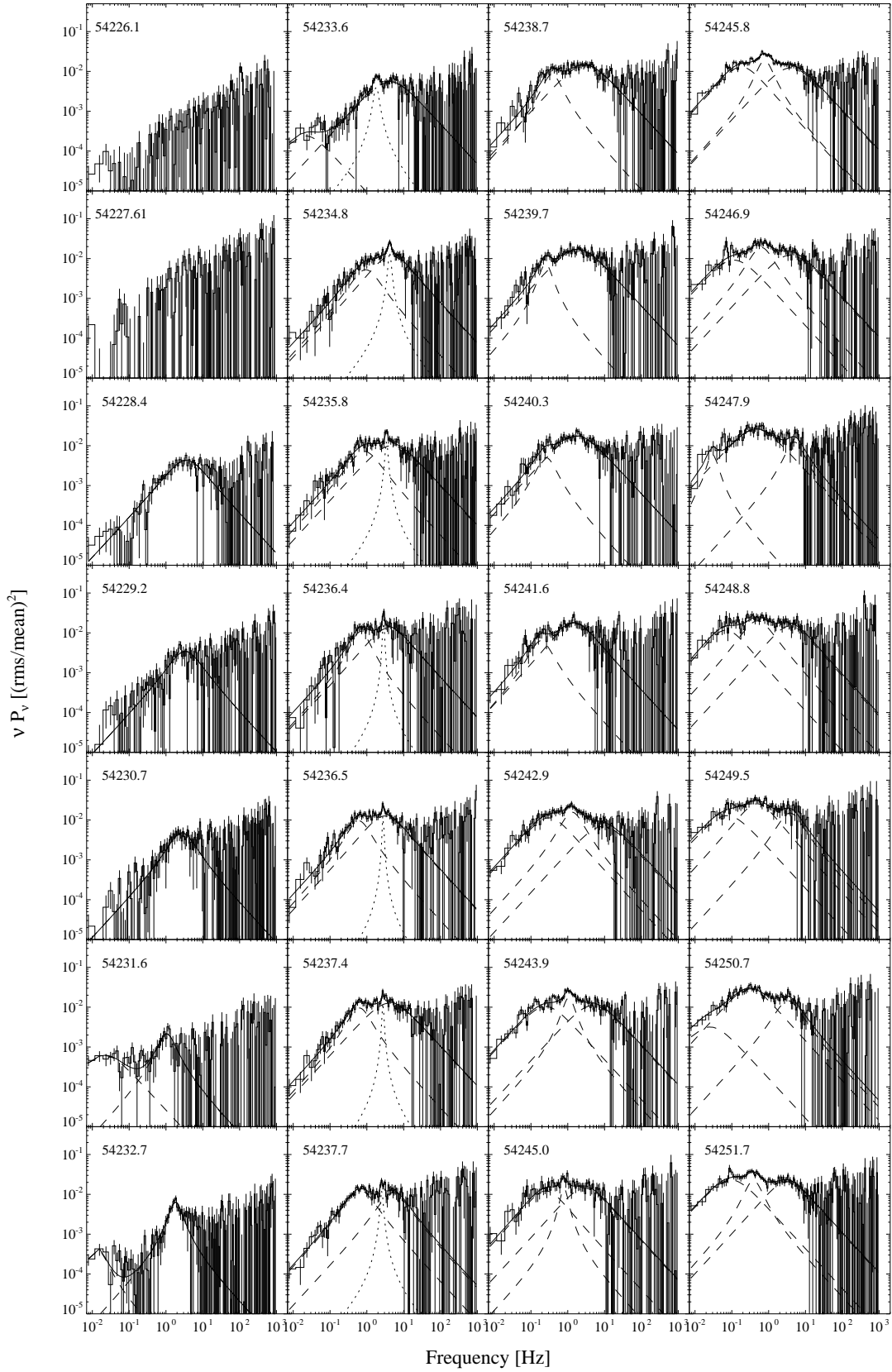


Figure 4.14 Evolution of the PSD modeled with Lorentzians for GX 339–4 during its 2007 outburst decay.

GX 339-4 (2011)

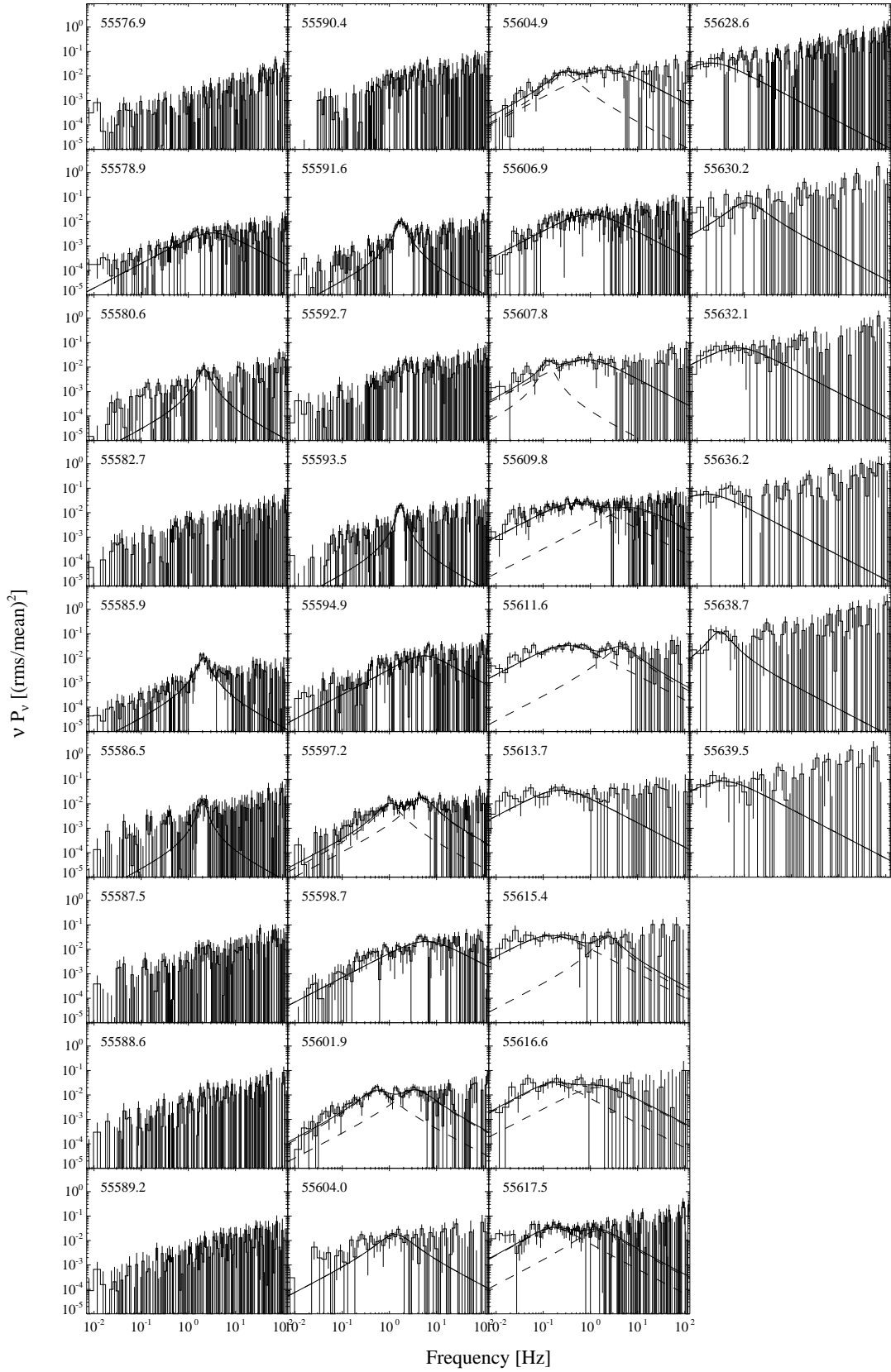


Figure 4.15 Evolution of the PSD modeled with Lorentzians for GX 339–4 during its 2011 outburst decay.

XTE J1550-564 (2000)

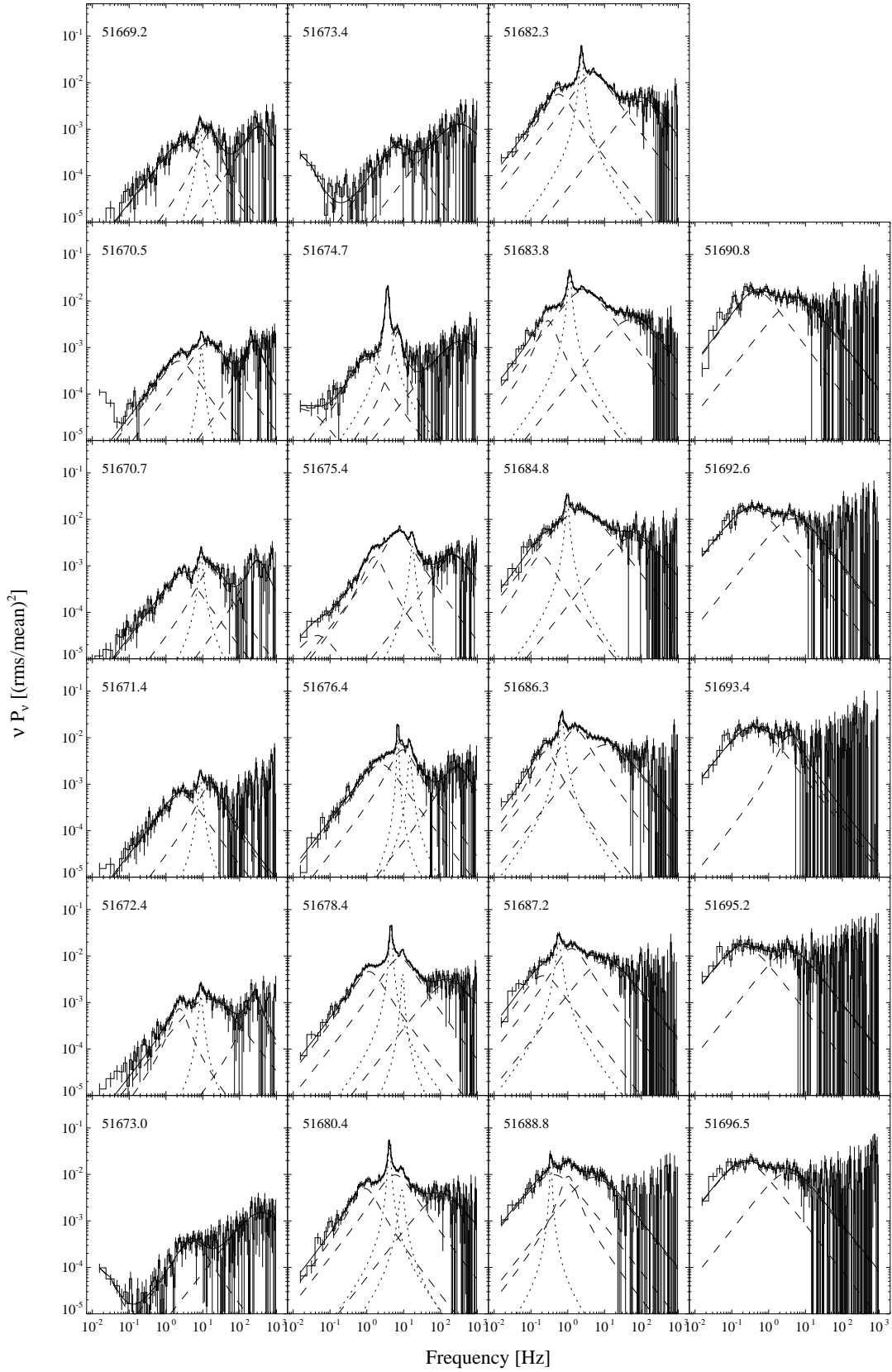


Figure 4.16 Evolution of the PSD modeled with Lorentzians XTE J1550–564 during its 2000 outburst decay.

XTE J1720-318 (2003)

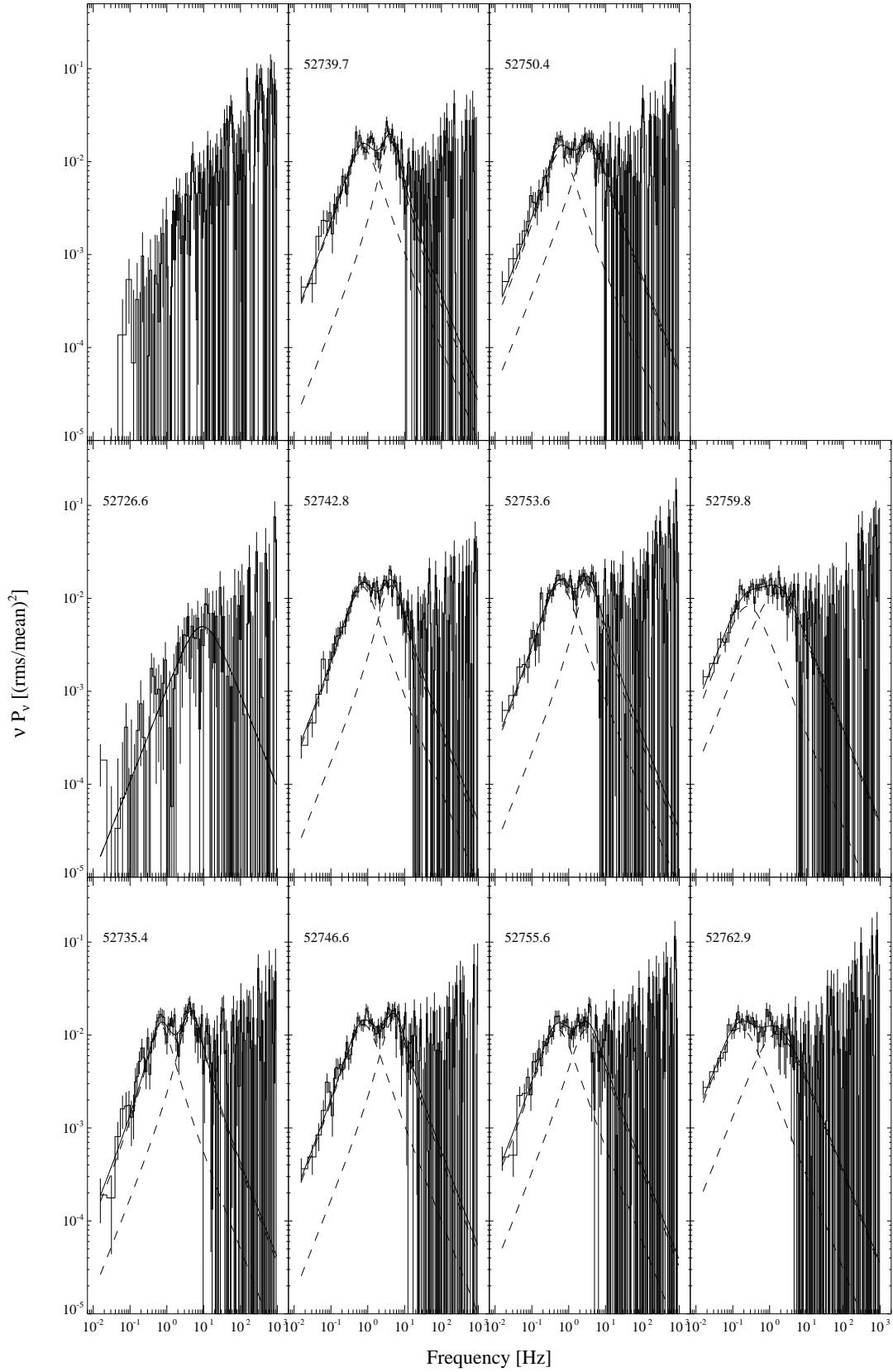


Figure 4.17 Evolution of the PSD modeled with Lorentzians for XTE J1720–318 during its 2003 outburst decay.

XTE J1752-223 (2010)

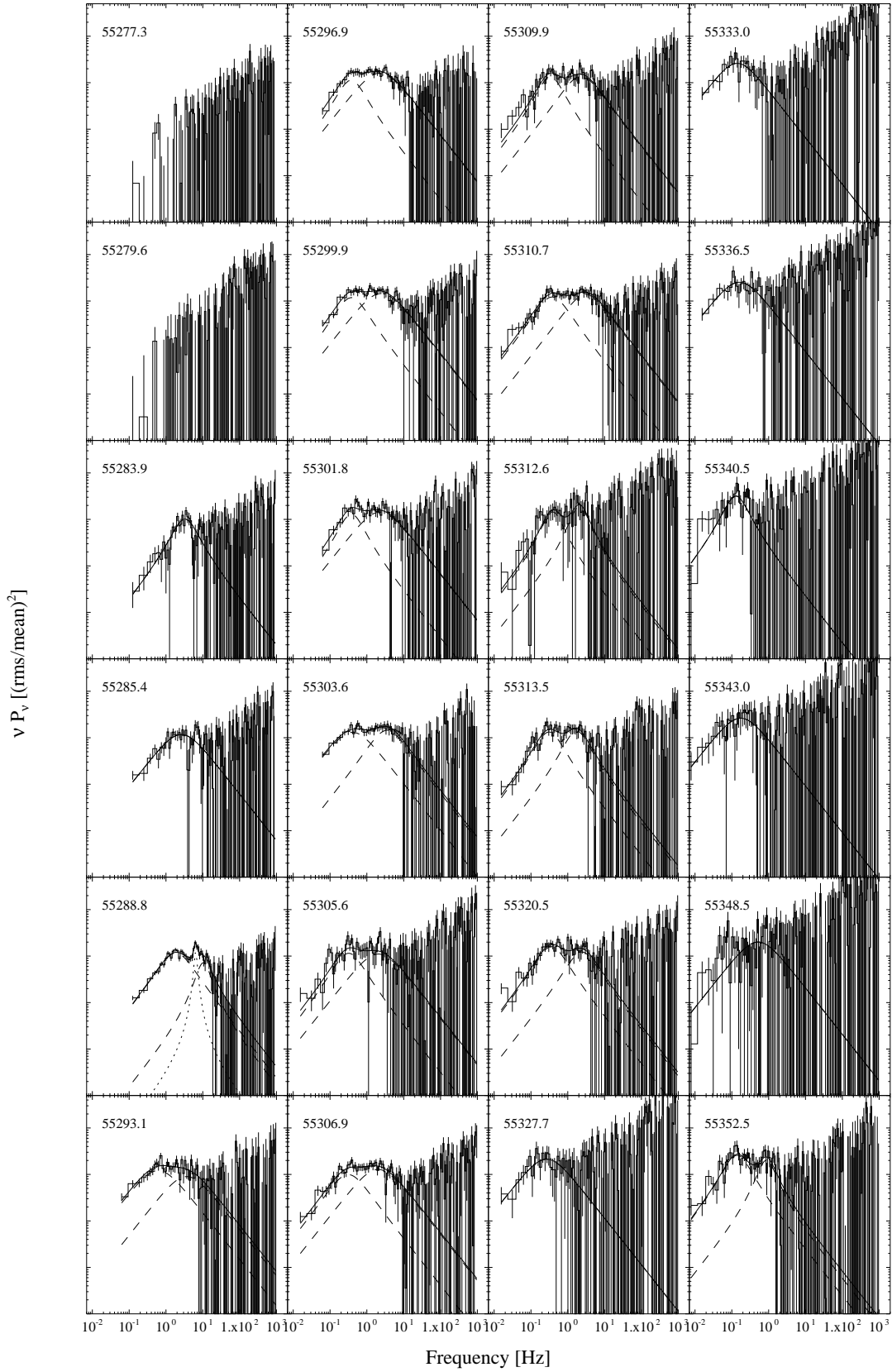


Figure 4.18 Evolution of the PSD modeled with Lorentzians for XTE J1752–223 during its 2010 outburst decay.

CHAPTER 5

Softening of the X-ray spectrum during outburst decays

5.1 Introduction

X-ray spectrum of GBHTs sometimes show a softening in the hard and quiescent states during outburst decay. This is evidenced in both single Chandra or daily RXTE monitoring observations at lower luminosities (Tomsick et al., 2001; Kalemci, 2002; Kalemci et al., 2005; Corbel et al., 2006, 2008; Plotkin et al., 2013). On the other hand, the times of the detection of the softening corresponds to the times of the presence of the radio and/or OIR brightening (Kalemci et al., 2005). Therefore there may be a possible connection between the softening and the launch of jets. Such a relation has not been studied systematically.

In this work, we revisit the softening of the X-ray spectrum of GBHTs and also look for the relation between the jet reappearance observed in the IR and/or radio bands and the softening. The results of this have been published in Dincer et al. (2008) and Kalemci et al. (2013).

5.2 Observations and data analysis

We use a large sample of outburst decays that show softening in the *RXTE* monitoring observations. The sample consists of seven outburst decays from six GBHTs. The X-ray spectral information of some outburst decays are gathered from the previous analysis of Emrah Kalemci and for other outburst decays we performed X-ray spectral analysis. For the spectral analysis, the PCA energy spectrum in the 3-25 keV for each observation was extracted using the standard FTOOLS programs. A systematic error of 0.8% up to 7 keV, and 0.4% above 7 keV was added to the energy spectra. Since the PCA collects all the photons within 1° field of view, Galactic ridge emission contaminates to observed source emission at lower flux levels, especially when sources are close to the Galactic plane. To subtract its contribution in the energy spectra of each sources, we estimated its spectral shape using simultaneous observations of imaging instruments, quiescent state observations, or the literature (Revnivtsev, 2003). For the X-ray spectral fitting, we used a model that consists of interstellar absorption, a multicolor disk black body, a smeared edge (Ebisawa et al., 1994), a power law, a second power law and a Gaussian to model ridge emission if necessary.

We also make use of the SMARTS IR or radio observations of GBHTs taken during the outburst decays that show softening. The IR photometric data was either collected from the literature or taken from Michelle M. Buxton and the radio data was exclusively gathered from the literature or ATELS.

5.3 Evolution of the softening during outburst decays

In the following sections, we plot the time evolution of the X-ray flux, the photon index and the IR and radio data (if available) for each outburst decay. These parameters aid us to follow the X-ray spectral hardness and the jet activity during outburst decay. Tracking the evolution of these parameters, we describe the conditions observed in the X-ray spectral properties and the jet activity during the softening.

5.3.1 4U 1543–47

The details of long term multiwavelength coverage and analysis of the 2002 outburst decay of the source can be found in Kalemci et al. (2005). The Galactic ridge emission was modelled using simultaneous *RXTE* and *XMM-Newton* observations (for its details, see Kalemci et al., 2005). The evolution of the spectral parameters along *J* band IR flux that belongs to the intermediate state and hard state are given in Fig. 5.1. At the beginning of the observations (between MJD 52,474 and 52,480), both the power-law and disk fluxes are high and the photon index is soft. This part of the outburst decay has no IR coverage. Since no IR brightening is reported under such X-ray conditions for other sources, the presence of an IR brightening is very unlikely at this stage. As the decrease in the disk flux accelerates, the photon index hardens and an IR brightening starts. Afterwards, the photon index saturates at $\Gamma=1.65$ during the peak of the IR brightening. After the peak of the IR flaring, while both the IR and power-law fluxes decay, the photon index softens to $\Gamma=2.00$ level. This softening was also noticed in Kalemci et al. (2005).

5.3.2 GX 339–4

For this source, the Galactic ridge emission was modelled using simultaneous *RXTE* and Chandra observations when the source was faint (Gallo et al., 2003a). Fig. 5.2 shows long term evolution of the spectral parameters and the *J* band IR magnitude during its 2007 outburst decay in the hard state. The observations in part of the decay that we analyzed do not require a disk component in the X-ray spectrum. At the beginning of the observations (between MJD 54,235 and 54,270), the X-ray flux and the photon index are correlated. During this time interval, the photon index decreases from $\Gamma=1.75$ to 1.55 while a brightening starts in the IR. Again during this time interval, the decrease in the X-ray flux is interrupted by a brightening. The peak of the brightening in the X-rays coincides with the peak of the flaring in the IR. During the peak of the brightening, the photon index is hard ($1.4 < \Gamma < 1.5$). As the IR and X-ray fluxes decay the photon index gradually increases to 1.7 level. We note that unlike in other outburst decays, the IR brightening lasts longer, more than 100 days.

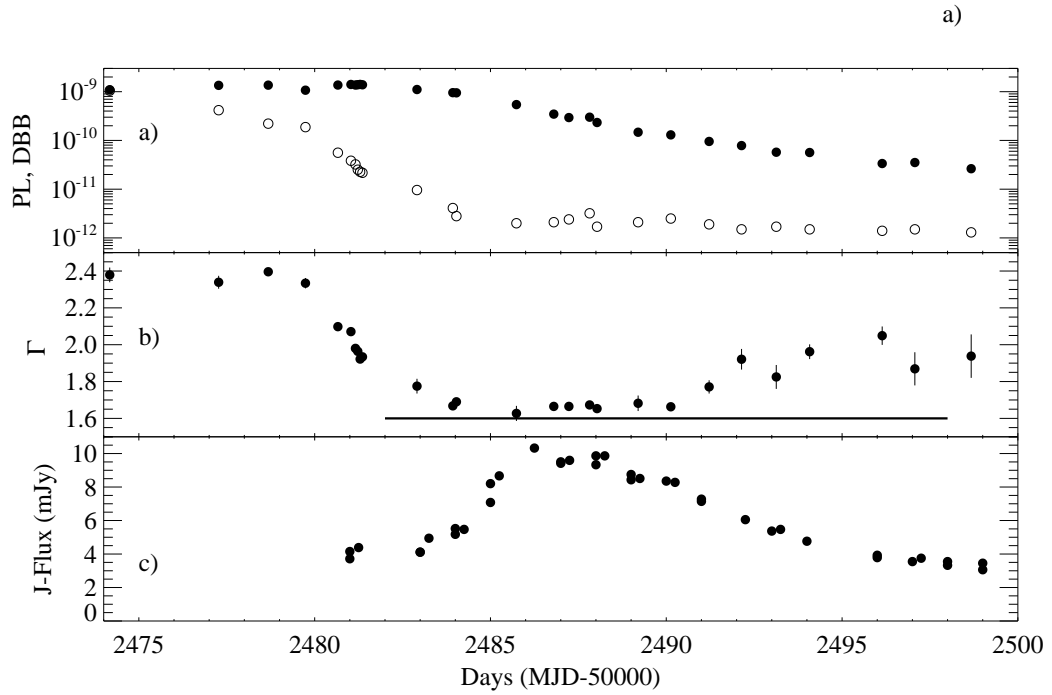


Figure 5.1 4U 1543–47; evolution of a) the power law (filled circles) and the disk black body (open circles) fluxes in the 3–25 keV band in units of $\text{ergs cm}^{-2} \text{s}^{-1}$, b) the photon index, c) the J band IR fluxes from Buxton & Bailyn (2004).

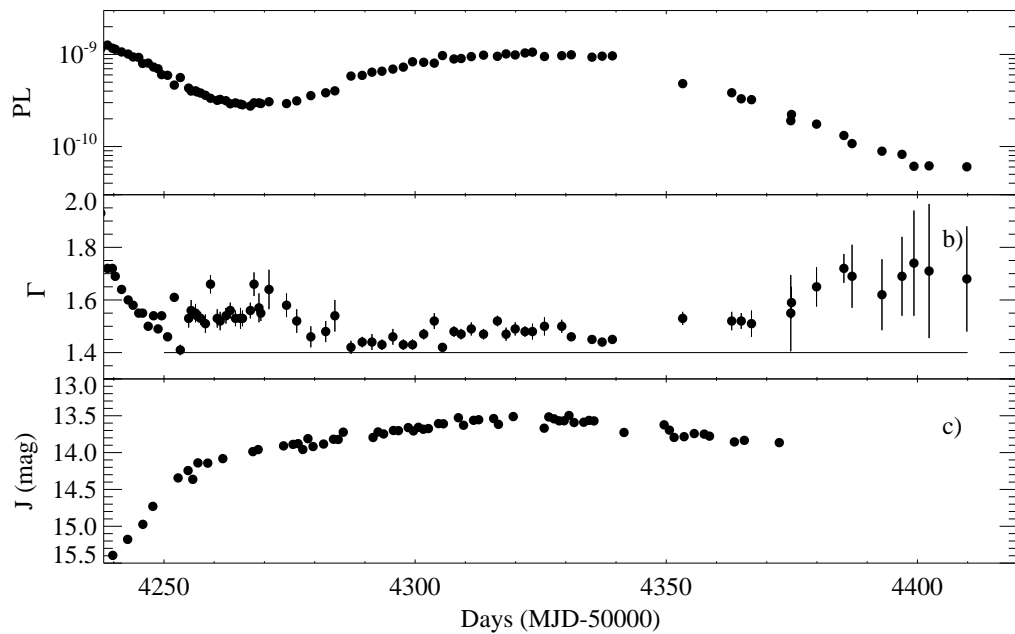


Figure 5.2 GX 339–4; evolution of a) the power law flux in the 3–25 keV band in units of $\text{ergs cm}^{-2} \text{s}^{-1}$, b) the photon index, c) the J band IR magnitudes from Buxton et al. (2012).

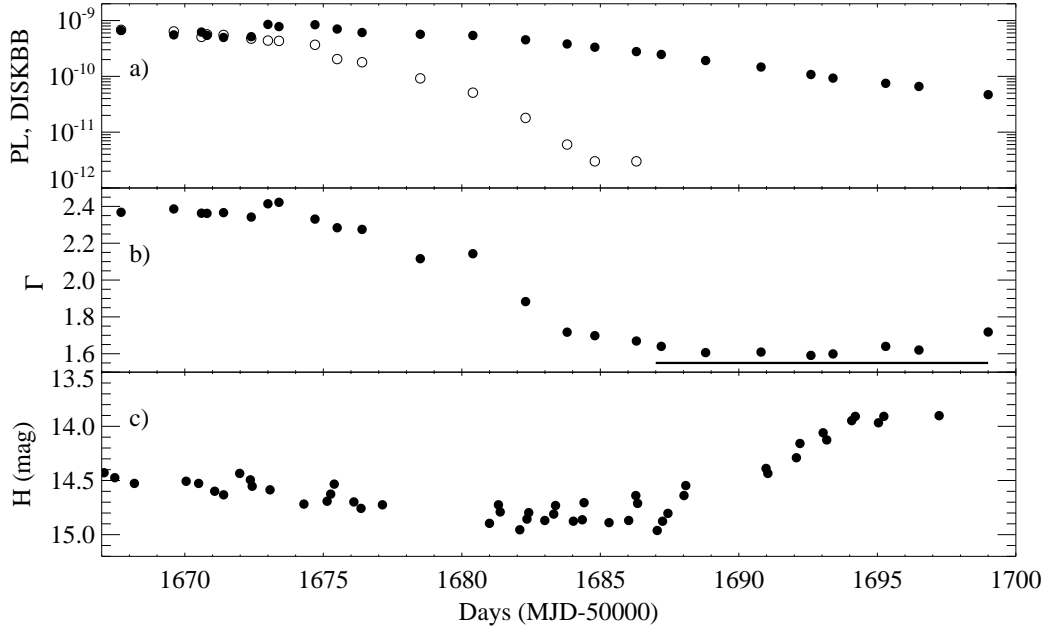


Figure 5.3 XTE J1550–564 in 2000; evolution of a) the power law (filled circles) and the disk black body (open circles) fluxes in the 2.5–20 keV band in units of $\text{ergs cm}^{-2} \text{s}^{-1}$, b) the photon index, c) the H band IR magnitude.

5.3.3 XTE J1550–564

XTE J1550-564 showed an outburst in 2000 and a minioutburst in 2001. X-ray spectral analysis of its 2000 outburst decay was reported in Tomsick et al. (2001). We use readily available analysis of Kalemci (2002).

Figure 5.3 belongs to the 2000 outburst decay when the source is in the hard state. At the beginning of the observations (between MJD 51,667 and 51,674), the power-law and disk fluxes are high at an equal level, the photon index is soft and the IR light curve shows an exponential decay. Then the photon index hardens to 1.6 while both the power-law and disk fluxes decrease. When the photon index reaches its hardest, an IR brightening occurs. The X-ray flux does not respond to the IR brightening. Afterwards, the photon index softens to $\Gamma=1.75$ when the IR brightening peaks. Further observation of the source by Chandra, at lower luminosities, show that the photon index even reaches to $\Gamma=2.30\pm 0.45$ (Tomsick et al., 2001).

For the minioutburst in 2001, we do not have IR coverage. Its X-ray spectral information is shown in Figure 5.4. The X-ray spectrum does not require a soft component over the course of outburst decay. Between MJD 51,940 and 51,961, the photon index is hard ($\Gamma=1.4$) and the X-ray flux is constant. As the X-ray flux decreases, the photon index softens to $\Gamma=1.75$.

5.3.4 XTE J1118+480

The X-ray data of the source during its 2000 outburst decay is directly taken from (Kalemci, 2002). During the outburst, the source never transitioned to the soft state and in part of

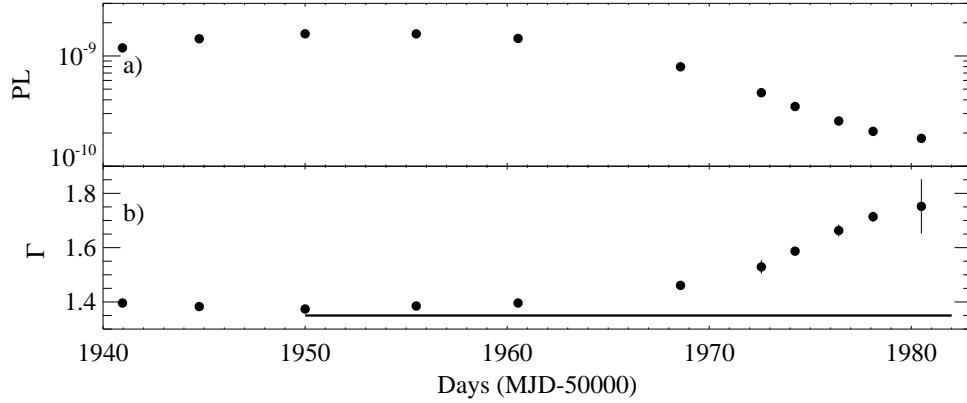


Figure 5.4 XTE J1550–564 in 2001; evolution of the power law in the 2.5–20 keV band in units of $\text{ergs cm}^{-2} \text{s}^{-1}$, b) the photon index.

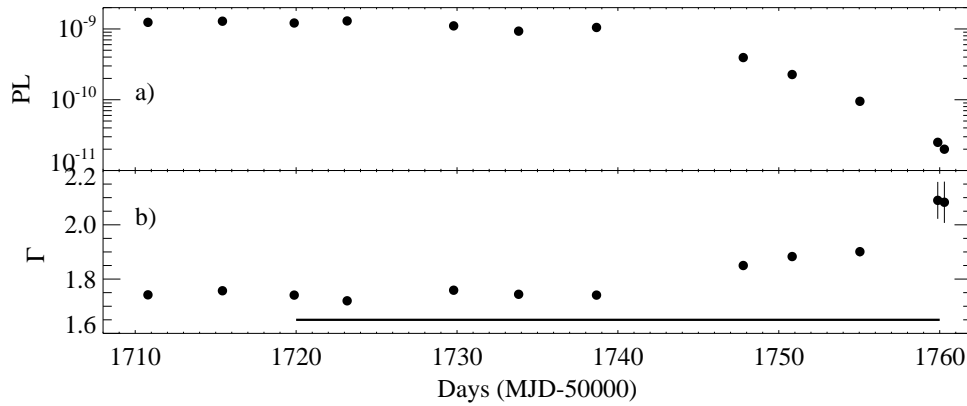


Figure 5.5 XTE J1118+480 in 2000; evolution of the power law in the 2.5–20 keV band in units of $\text{ergs cm}^{-2} \text{s}^{-1}$, b) the photon index.

the outburst decay that we present in Figure 5.5 the X-ray spectrum of the source can be described by a power-law component. At the beginning of the observations the X-ray flux and the photon index shows a flat evolution for about 30 days. The X-ray spectrum is hard with a photon index of $\Gamma=1.75$. Towards the end of the decay, as the X-ray flux decreases, the photon index softens to $\Gamma=2.1$.

5.3.5 GRO J1655–40

The long term multiwavelength coverage of 2005 outburst decay of the source was published in Kalemci et al. (2006b) excluding the lowest flux analysis. We analyzed the very end of the outburst decay taking into account the Galactic ridge emission. The Galactic ridge emission was modelled using simultaneous *RXTE* and *Swift* observations when the source was faint (Homan et al., 2005b). Figure 5.6 shows evolution of the spectral parameters and the radio flux. At the beginning of the observations (between MJD 53,627 and 53,634), the photon index, the power-law flux, and the disk flux decrease. During this

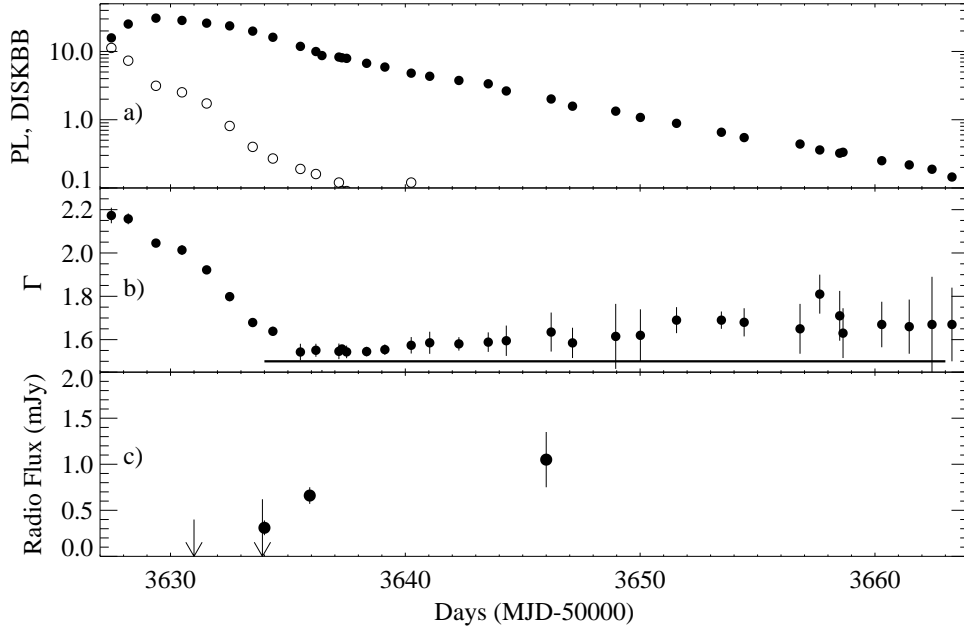


Figure 5.6 GRO J1655–40; evolution of a) the power law (filled circles) and the disk black body (open circles) fluxes in the 3–25 keV band in units of $10^7 \text{ ergs cm}^{-2} \text{ s}^{-1}$, b) the photon index, c) the radio flux.

time, radio observations do not show a detection of the source. Once the X-ray spectrum reaches its hardest at $\Gamma=1.5$ on MJD 53,634, the radio observations show a detection of the source for the first time. From then on, the photon index gradually increases to $\Gamma=1.7$ indicating a softening of the spectrum. The softening was also noticed in Sobolewska et al. (2011), however, our results show that the softening is present even we apply a Galactic ridge correction to the X-ray spectrum of the source.

5.3.6 H 1743–322

The long term multiwavelength coverage of the 2003 outburst decay of H 1743–322 is reported in Kalemci et al. (2006a). As H 1743–322 is close to the Galactic plane ($b = -1.83$), both the source confusion and the Galactic ridge emission are important for determining its spectral properties. A detailed subtraction of these factors are described in Kalemci et al. (2006a). Figure 5.7 shows the evolution of the X-ray spectral and radio properties. At the beginning both the PL and the disk fluxes are high and spectrum is soft with $\Gamma = 2.2$. While the X-ray flux decays, the spectrum hardens to $\Gamma = 1.7$ and a radio brightening occurs. In the last six observations, a significant softening of the spectrum is observed.

5.4 Relation of the photon index to the ELF

It would be interesting to know the luminosity level that the softening occurs since the accretion models depend primarily on the X-ray luminosity. Figure 5.8 shows the relation

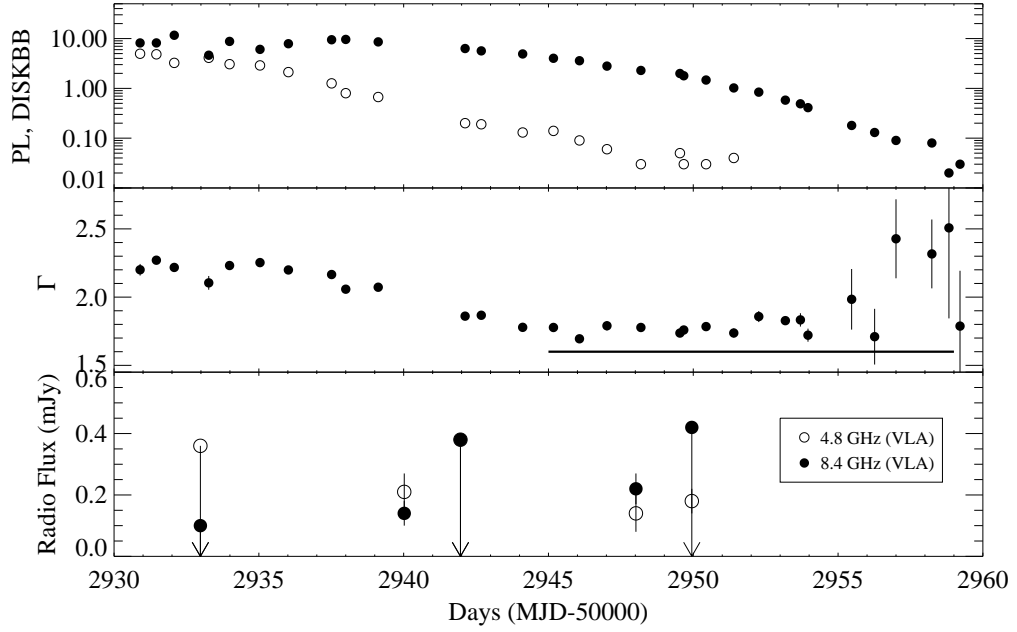


Figure 5.7 H 1743–322; evolution of a) the power law (filled circles) and the disk black body (open circles) fluxes in the 3–25 keV band in units of 10^{-10} ergs cm^{-2} s^{-1} , b) the photon index, c) the radio flux.

of the photon index to the total Eddington luminosity fraction (ELF) for all the outburst decays. It is clearly seen that the photon index Γ sharply decreases at higher ELF ($> 10^{-2} L_{Edd}$). Below a threshold ELF ($L_X/L_{Edd} < 10^{-2}$), a negative correlation is present which indicates the softening of the X-ray spectrum and varies for some sources. For instance, GRO J1655–40 softens at a faster rate than XTE J1550–564 (2001).

5.5 Power-law ELF decay rate

For individual outburst decays, we showed that the softening occurs while the power-law flux decays. The X-ray spectral investigations of a larger sample of GBHTs during outburst show that the disk blackbody flux decays in a very narrow time scale range whereas the power-law flux shows very different decay time scales (Kalemci et al., 2013). Moreover, no indications of softening is observed for some of these outburst decays. We decided to investigate a possible correlation between the decay rate of the power-law ELF and the softening.

We plot the time evolution of the power-law ELF during thirteen outburst decays from eight BHXBs that show significant evidence for a softening in Figure 5.9a and that lack of significant evidence for a softening in Figure 5.9b. In eleven cases, the decays are consistent with an exponential form and we quantified their e-folding decay rates (see Table 5.1). The e-folding decay rates for the outburst decays that show softening (Figure 5.9a) are concentrated between 2.04 and 7.59 days. There is only one outlier with softening to this trend, the 2007 decay of GX 339-4. We note that this outburst decay is not simply an exponential decay. The exponential decay occurs after an X-ray flar-

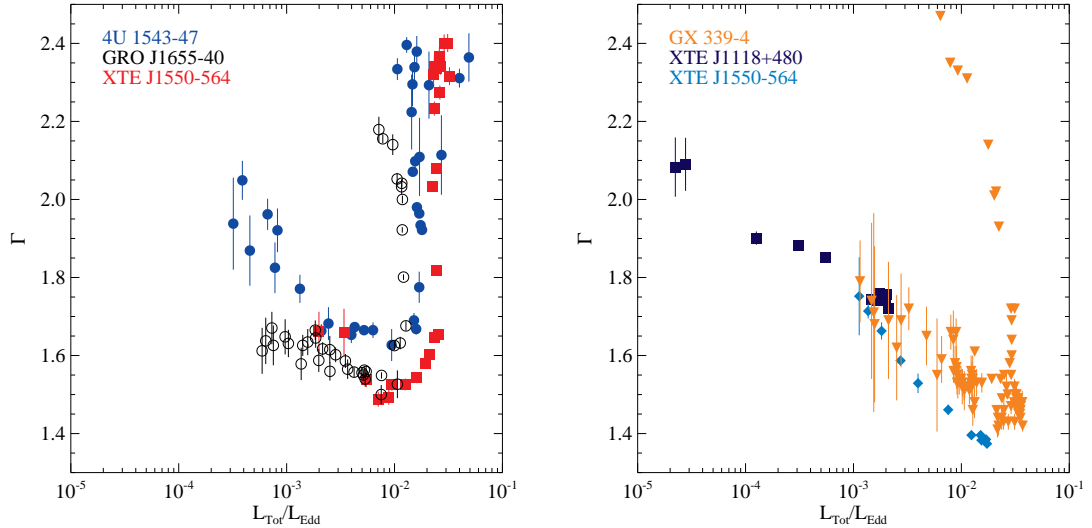


Figure 5.8 Relation between the photon index and Eddington luminosity fraction in the 3-200 keV range for all the outburst decays. For clarity the sample is divided into two plots. Since the errors on the ELF's are large (up to 50% for GX 339-4) due to errors on the mass and the distance measurements, they are not shown to avoid any cluttering in the plots

ing (see Figure 5.2). For the outburst decays with the lack of evidence for softening, the e-folding decay rates range between 5.55 and 15.15 days. For XTE J1720–318 and XTE J1752–223, we are not able to determine a decay rate. The former lacks of data at lower luminosities and the latter shows a complicated decay profile with a flaring (see Figure 5.9b).

5.6 Discussion

We characterized the evolution of the softening of the X-ray spectrum during seven outburst decays of six BHXBs. Among these outburst decays, five of them were already known to show a softening (see references in Wu & Gu, 2008) and we added the detection of the softening during outburst decays of GRO J1655–40 (2005) and GX 339-4 (2007). The photon index reaches its hardest at $L_{3-200keV} \approx 10^{-2} L_{Edd}$ then the softening starts before the luminosity drops below $L_{3-200keV} \approx 10^{-3}$. The luminosity at which the turn over is observed was known (Wu & Gu, 2008), and GRO J1655–40 (2005) and GX 339-4 (2007) are consistent with this.

Our sample also reveals that the softening is observed at the end of both hard only outbursts which a transition from the hard state to the soft state is not present (XTE J1550–564 [2001], XTE J1118+480) and outbursts that experience soft state (XTE J1550-564 [2000], 4U 1543–47, GX 339–4, GRO J1655–40, H 1743–322 [2003]). Such a distinction may be important for the understanding of the softening. For instance, for XTE J1550–564 (2001) and XTE J1118+480, the softening begins as soon as the decay in the X-ray flux starts (see Figure 5.4,5.5) whereas for other outburst decays the softening

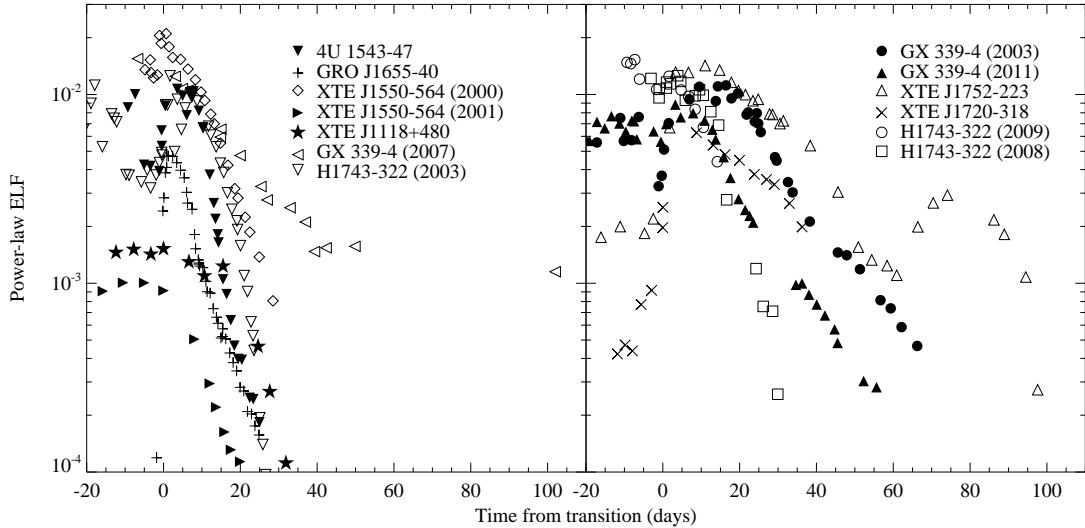


Figure 5.9 Time evolution of the power-law ELF for GBHTs that show a) significant evidence for softening and b) lack of evidence for softening.

begins some time after the start of the decay in the X-ray flux.

Our efforts on relating the decay rates to the occurrence of softening do not yield a simple picture due to the flarings that interrupts the exponential decays. However if we consider the decays only in the exponential form, we see that the occurrence of the softening is associated with the fastest decays.

The softening can be explained both in terms of radiatively inefficient flows or non-thermal jets. For detailed discussions of these alternatives, see Wu & Gu (2008); Russell et al. (2010); Sobolewska et al. (2011). We would like to emphasize an important finding: the cases with the clear softening are the ones with the fastest drop in the power-law flux. This is consistent with the scenario described in Russell et al. (2010). When the compact jet first forms, the X-rays it produced by synchrotron mechanism may be much less compared to the X-rays produced through thermal Comptonization. Since, for these sources, the hard Comptonization flux drops much quicker, softer X-rays from jet synchrotron may result in a steeper photon index at the end of outburst decays. For GX 339-4 (2007), the decay of Comptonized power-law flux is slow, and the effect cannot be seen within 30-40 days after the transition. In fact, for the 2003, 2005 and 2011 outbursts, the NIR flux also decreases within 80 days, but in 2007, the NIR flux stays constant for over 100 days, and the softening in the X-rays is observed as the X-ray flux decreases 130 days after the start of the NIR rise (see Figure 5.2 for the evolution of the NIR flux and the power-law flux). The drop in X-ray flux is also fast for H1743-322 in 2008, but the Galactic Ridge strongly affects the RXTE data for this source, and the large errors in the photon index does not provide any indication of softening for this source (Kalemci et al., 2013).

Table 5.1. E-folding decay rates of the power-law ELFs

Source	Year	Dates (MJD-50,000)	τ_e (days)	Comment
Decays that show evidence for softening				
4U 1543–47	2002	2,490-2,500	5.91 ± 0.23	-
GRO J1655–40	2005	3,636-3,660	7.25 ± 0.10	-
XTE J1118+418	2000	1,747-1,760	4.20 ± 0.08	-
XTE 1550–564	2000	1,682-1,702	7.46 ± 0.15	-
XTE 1550–564	2001	1,968-1,980	7.59 ± 0.32	-
H1743–322	2003	2,950-2,960	2.04 ± 0.02	-
GX 339–4	2007	4,350-4,400	21.94 ± 0.48	decay interrupted by a flaring
Decays with the lack of evidence for softening				
H1743–322	2008	4,500-4,519	5.55 ± 0.09	-
H1743–322	2009	5,020-5,030	9.31 ± 0.77	-
GX 339–4	2003	2,733-2,784	15.15 ± 0.19	-
GX 339–4	2011	5,610-5,650	15.15 ± 0.26	-
XTE J1720–318	2003	-	-	insufficient coverage
XTE J1752–223	2010	-	-	decay interrupted by a flaring

CHAPTER 6

Reflection in neutron star and black hole X-ray binaries

6.1 Introduction

The hard X-ray radiation of black hole X-ray binaries (BHXB) in the hard state can be characterized with a Comptonized emission generated in the optically thin plasma in the vicinity of the compact object (Sunyaev & Truemper, 1979). The unsaturated Comptonization of soft seed photons with characteristic temperature T_{seed} on a hot plasma (corona) with temperature T_e produces a nearly power-law shape in the energy range from $\sim 3kT_{seed}$ to $\sim kT_e$ (Sunyaev & Titarchuk, 1980). The photon index of the Comptonized spectrum depends on the ratio of the energy of the electrons in the hot corona and the energy flux brought into this corona by the soft seed photons; the lower the ratio the softer the Comptonized spectrum (Haardt & Maraschi, 1993).

In addition to the power-law shape, the X-ray spectrum of BHXBs also show deviations in the 5-30 keV energy band, the fluorescent K_α line of iron at 6.4 keV, iron K-edge at 7.1 keV and a broad hump at ~ 20 -30 keV. The deviations are characteristic signatures of the reflection of the the Comptonized radiation by a cold medium located in the vicinity of the optically thin corona (George & Fabian, 1991). This reflecting medium is thought to be the optically thick accretion disk surrounding the inner region occupied by the corona (see Figure 1.6).

The observational estimation of the reflection amplitude provides important clues on the accretion properties of BHXBs. For several systems, the slope of the hard X-ray spectrum is known to positively correlate with the reflection amplitude (Zdziarski et al., 1999; Gilfanov et al., 1999; Revnivtsev et al., 2001; Wilms et al., 2006). From the existence of such a relation, a commonly pronounced conclusion is that the accretion disk plays a dominant role as a source of the seed photons to the Comptonization region.

Weakly magnetized neutron star X-ray binaries (atolls) in the hard state are also known to exhibit a similar X-ray spectrum consistent with a Comptonized emission and reflection features (Gierliński & Done, 2002; Egron et al., 2013). However, their X-ray spectrum and the reflection features can be expected to be quantitatively different than observed in the BHXBs. This is due to the presence of a hard surface that provides additional source of seed photons. Here, we describe the X-ray continuum spectra of BHXBs and atolls with a physical model that consists of both thermal Comptonization and reflection features. The results of this study is published in Dinçer et al. (2011).

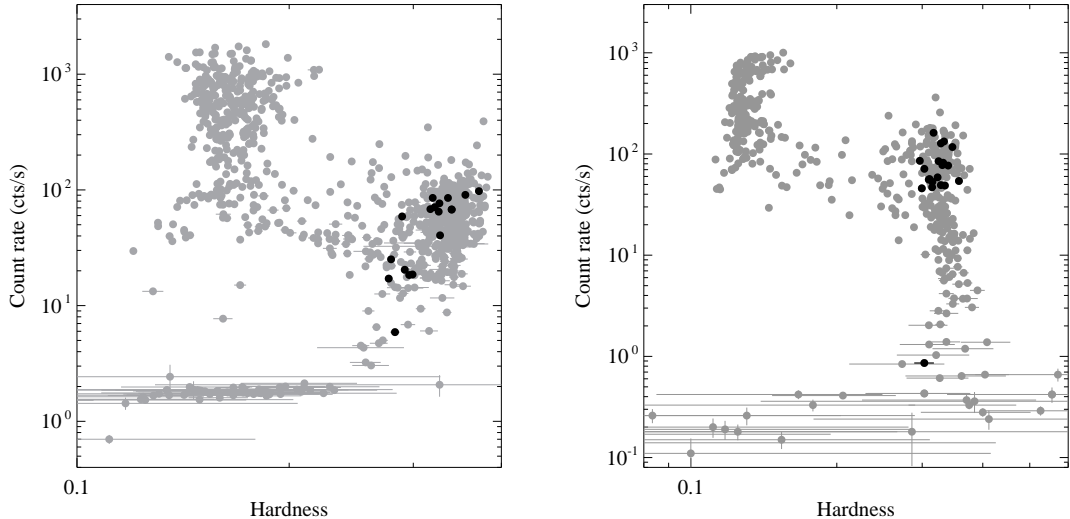


Figure 6.1 HIDs of 4U 1608–52 (left panel) and Aql X–1 (right panel) observed with the *RXTE*/ASM. Count rates are in the 4–20 keV band and hardness is defined as the ratio of count rates in the 9–20 and 4–9 keV bands. Only the darker points are selected for the spectral fitting.

6.2 Observations and data reduction

For our analysis, we used archival *RXTE*/PCA observations of BHXBs GX 339–4 from 1996–1997, XTE J1550–564 from 2000 and Cyg X–1 from 1996–1998 and atolls 4U 1608–52 and Aql X–1. To select the hard state observations of atolls, we constructed hardness-intensity diagrams (HID) using the *RXTE*/ASM data (see Figure 6.1). In the HID, the points are mainly concentrated in two regions separating the hard and soft state observations. We randomly picked hard state observations with exposure times greater than 2500s. The hard state observations of Cyg X–1 and GX 339–4, and XTE J1550–564 are sampled from Gilfanov et al. (1999), Revnivtsev et al. (2001), and Tomsick et al. (2001), respectively. The photon indices for the selected observations of BHXBs in these works are less than 1.9, consistent with the hard state.

We reduced all the data with the scripts developed at UC San Diego and University of Tübingen using HEASOFT v6.9. In the extraction of the energy spectra the photons in the 3–25 keV band from all available Proportional Counter Units (PCUs) were considered. The background spectra were created from “bright” or “faint” models on the basis of the net count rate being greater or less than $70 \text{ counts s}^{-1} \text{ PCU}^{-1}$, respectively. We added 0.5% systematic error to all spectra as suggested by the *RXTE* team.

6.3 Spectral model

In order to describe the observed X-ray spectra of both BHXBs and atolls, we use a photoabsorption model (*phabs* in Xspec) for the interstellar extinction and a thermal Comptonization model (*compps* in Xspec, Poutanen & Svensson, 1996). For the pho-

Table 6.1. Hydrogen column densities of BHXBs and atolls used in the spectral fits

Source	n_H (10^{22}cm^{-2})	Reference
GX 339–4	0.5	Kong et al. (2000)
XTE J1550–564	0.9	Jain et al. (1999); Tomsick et al. (2001)
Cyg X–1	0.6	Gilfanov et al. (1999)
4U 1608–52	1.08	Güver et al. (2010)
Aql X–1	0.34	Dickey & Lockman (1990)

toabsorption the Hydrogen column densities, n_H , are fixed at values given in Table 6.1. In the *compps* model, primary parameters describing the thermal Comptonization spectrum are the electron temperature of the plasma/corona (T_e), the seed photon temperature (T_{seed}), and the Compton y -parameter ($y = 4kT_e/m_e c^2 \max(\tau, \tau^2)$). A higher value of the Compton- y parameter implies a softer spectrum. The reflection component is intrinsically included in *compps* model, $R = \Omega/2\pi$, where Ω is the solid angle occupied by the cool material covers as viewed from the source of primary X-rays.

The limited energy range of PCA spectrum does not allow one to determine T_{seed} and T_e . Therefore, in the spectral fitting, we decided to fix these parameters at some reasonable values. A reasonable estimation of the corona temperature T_e comes from the hard state broadband spectral fitting. The fits point to a T_e between 20 and 80 keV for atolls (Gierliński & Done, 2002; Tarana et al., 2007), and 50 and 200 keV for BHXBs (Zdziarski et al., 2004; Motta et al., 2009). The origin of the seed photons are expected to be different for BHXBs and atolls. For BHXBs, the source of the seed photons is thought to be the inner region of the accretion disk. In the hard state, the observed values of disk temperature are around 0.3 keV (Di Salvo et al., 2001; Ibragimov et al., 2005; Reis et al., 2010; Reynolds & Miller, 2013). For atolls, the source of the seed photons has two possible origins, the inner region of the accretion disk and the surface of the neutron stars. To date the individual components are not resolved in the hard state. This is possibly due to a blending of the components. However, fits to the broadband spectra yield a T_{seed} of 0.2-0.6 keV in the hard state (Egron et al., 2013).

6.4 Compton- y - R relation

Figure 6.2 shows the relation between the Compton- y parameter and the reflection amplitude for both BHXBs and atolls. There are two important results. First, both type of sources show a negative correlation indicating that softer the X-ray spectrum higher the reflection amplitude. Second, for a given reflection amplitude the X-ray spectrum of atolls are softer than that of BHXBs.

In the fits, we assumed $T_{seed} = 0.3$ keV and $T_e = 50$ keV for atolls and $T_{seed} = 0.3$ keV and $T_e = 100$ keV for BHXBs. The particular values of the T_{seed} and T_e may be affecting the numerical values of the Compton- y parameter and the reflection amplitude. The assumed values for BHXBs are rather well constrained. To investigate this in atolls,

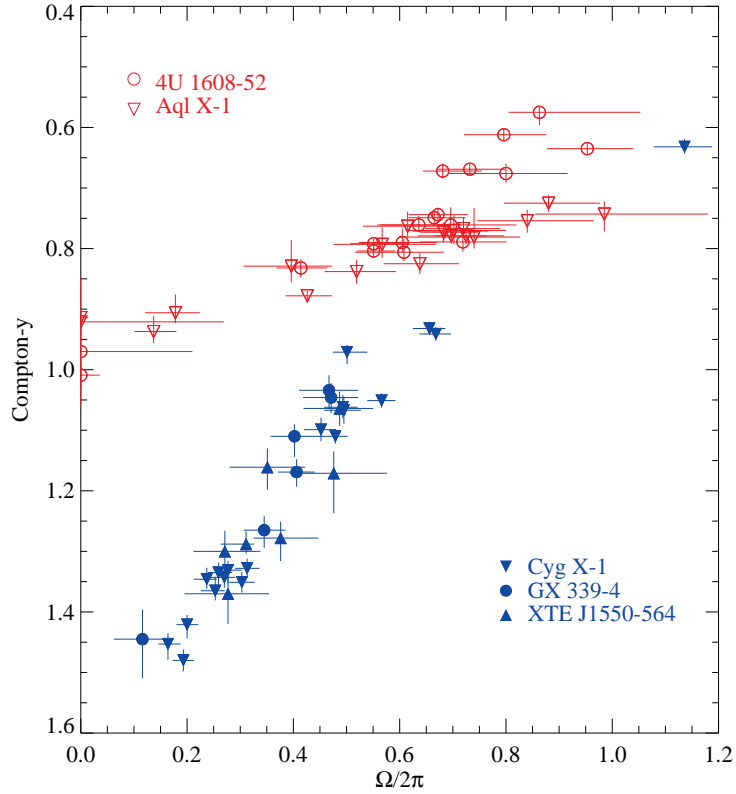


Figure 6.2 Compton- y parameter vs reflection amplitude for both BHXBs (blue) and atolls (red).

we fit the X-ray spectra of 4U 1608–52 using T_{seed} , $T_e = 0.1$, 50 keV and 0.1, 100 keV. The assumed values of T_{seed} and T_e do change the numerical values of the Compton- y parameter and the reflection amplitude (see Figure 6.3) but change neither the character of correlations nor the mutual location of BHXBs and atolls in the Compton- y - R plane.

6.5 Discussion

We studied the relation between the Compton y -parameter and the reflection amplitude in the hard state of BHXBs and atolls with a Comptonization model. Our results confirm the existing correlation for BHXBs (e.g. Gilfanov et al., 1999): softer the spectrum larger the reflection amplitude. Additionally, we found a similar correlation between the two parameters for atolls but with a softer X-ray spectrum at a given reflection amplitude.

The spectral correlation for both type of systems, suggests a close relation between the solid angle subtended by the reflecting media and the influx of the soft photons to the Comptonization region. The geometry commonly discussed in the hard state models of BHXBs and atolls involves a hot corona near the compact object surrounded by a cold, optically thick accretion disk (Done et al., 2007). In such a geometry the decrease of the inner radius of the disk would result in an increase of the solid angle subtended by the disk and an increase of the flux of the soft photons to the corona which then in turn soften

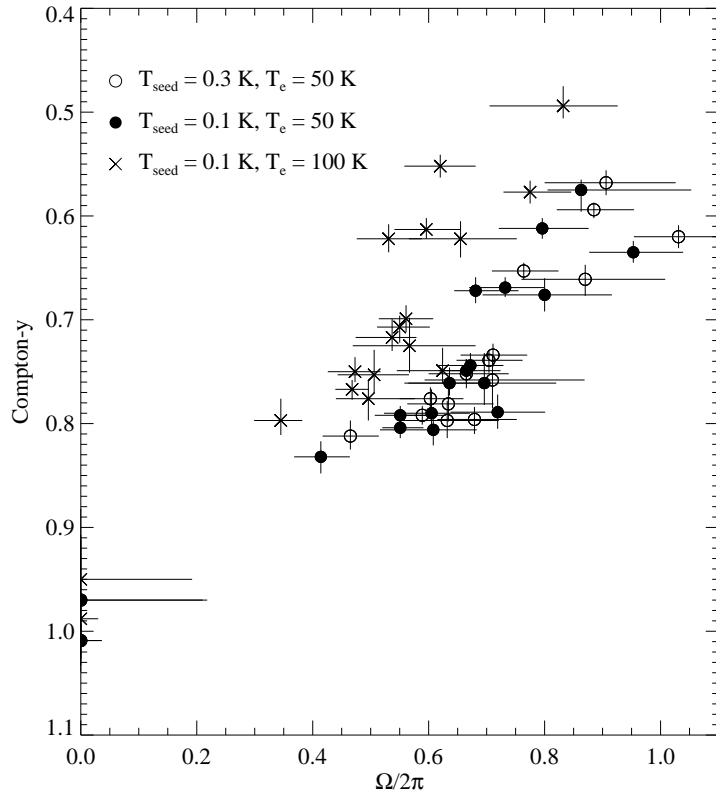


Figure 6.3 T_{seed} and T_e dependence of the correlation between the Compton-y parameter and the reflection amplitude for 4U 1608–52.

the spectrum.

The difference between the correlations of atolls and BHXBs, can be understood in terms of neutron stars having hard surface and black holes having no hard surface. A hard surface inside the corona provides additional soft photon flux which leads to a cooling of the corona and therefore to a softer spectrum.

CHAPTER 7

Conclusions

This thesis provides new insights on the understanding of the accretion-ejection process of the black hole X-ray binaries in the hard state by combining X-ray and optical and infrared (OIR) data. X-ray spectral and temporal properties along with the OIR photometric and radio data are investigated for large subset of black hole X-ray binaries during outburst decay to probe the conditions when the jets turn on as well as to probe the influence of the jet on the accretion process.

We analyzed the multiwavelength observations of the black hole transient GX 339-4 during its outburst decay in 2011 using the data from RXTE, Swift, and SMARTS. Based on the X-ray spectral, temporal, and OIR properties, we determined the states and transitions that the source went through as well as the conditions for the start of the IR brightening. The source evolved from the soft intermediate to the hard state. Twelve days after the start of the transition, a rebrightening was observed simultaneously in the OIR bands. This brightening occurred as soon as the source reached the hardest spectral index or the hard state branch in the HID. After we published our results, Corbel et al. (2013a) for the first time showed that there is a delay between the OIR and the radio brightening using our results. Moreover, this brought new insights to the understanding of the jet formation during outburst decay. Thanks to the OIR observing campaign we disentangled the excess and the baseline emission. We created SEDs from observations at the start, and close to the peak of the OIR rebrightening. The excess OIR emission above the smooth exponential decay yields flat spectral slopes for these SEDs. Assuming that the excess is from a compact jet, we constrained the jet models via the possible locations of the spectral break that mark the transition from optically thick to optically thin synchrotron components. Interestingly, we detected fluctuations with the binary period of the system only during the rising part of the rebrightening. We discussed a scenario that includes irradiation of the disk in the intermediate state, irradiation of the secondary star during OIR rise, and jet emission dominating during the peak to explain the entire evolution of the OIR light curve.

A comprehensive study of X-ray variability patterns and jet emission has never been done before for GBHTs in the hard state. For this reason, we compared the evolution of the frequency and rms amplitude of variability of QPOs and Lorentzian components in the PSD to the evolution of IR and radio fluxes. We found that the rms amplitude of the type-C QPOs first increases, correlating with the total rms amplitude, and then QPO rms amplitude decreases while the total rms amplitude increases. The decrease in the QPO rms amplitude occurs within a few days prior to or following the start of the IR rise or the first detection of the optically thick radio emission. There might be causal relation between the jet growth and the decrease in the QPO rms amplitude. Jets may be affecting

the QPO behavior or destroying QPO mechanism.

As we are interested in how compact jets affect the X-ray variability and spectral patterns, we also investigated the softening behaviour of these sources observed at low flux levels while the compact jets are presents. We showed that the softening occurs within a few days timescales prior to or following the start of the indications of the jet activity. We also investigated relation of the softening phenomena to the decay rate of the X-ray luminosities. Since both radiatively efficient flows and jet models are able to explain the observed softening, such attempts can provide constraints on different mechanisms. In our data set, the X-ray luminosities are mainly in the exponential decay form but there were a few cases interrupted by flaring. We found that the cases with the softening are associated with the faster exponential decay rates. We related our result with a scenario in which the X-ray emission from the Comptonization at higher energies decays faster than the jet X-ray emission at softer energies.

We grouped the sources with respect to their tracks in the radio - X-ray correlation and examined their variability patterns separately. We found that the outliers track sources show a lower rms amplitude than the standard track sources in the hard state. We interpreted this result in terms of internal shock jet emission model. This is the first time that a distinction between the short term timing properties of two populations discovered.

We also evaluated the predictions of the MDAF theory. There is no general agreement between the theoretical scaling and observational relation between the QPO frequency and X-ray luminosity of outliers track sources. The MDAF theory remains inadequate in explaining the distinction between the outliers and the standard track sources.

Finally, we studied the correlation between the spectral index and reflection amplitude for black hole and low magnetic field neutron star X-ray binaries. We confirmed the existing correlation for black hole X-ray binaries using a physical Comptonization model: softer the spectrum larger the reflection amplitude. This is commonly interpreted as the accretion disk playing a dominant role as a source of the seed photons to the Comptonization region. We also found a similar correlation for neutron star X-ray binaries with a softer spectral hardness for a given reflection amplitude. Since both type of systems have similar potential wells we interpreted the softer correlation for neutron star X-ray binaries as a direct result of the presence of a hard surface. The hard surface provides additional source of seed photons and cools the corona, providing softer spectra for a given reflection amplitude.

Bibliography

- Abramowicz, M. A., Czerny, B., Lasota, J. P., & Szuszkiewicz, E. 1988, *ApJ*, 332, 646
- Arnaud, K. A. 1996, in *Astronomical Society of the Pacific Conference Series*, Vol. 101, *Astronomical Data Analysis Software and Systems V*, ed. G. H. Jacoby & J. Barnes, 17
- Balucinska-Church, M., & McCammon, D. 1992, *ApJ*, 400, 699
- Barret, D., McClintock, J. E., & Grindlay, J. E. 1996, *ApJ*, 473, 963
- Beckwith, K., Hawley, J. F., & Krolik, J. H. 2009, *ApJ*, 707, 428
- Belloni, T., Homan, J., Casella, P., van der Klis, M., Nespoli, E., Lewin, W. H. G., Miller, J. M., & Méndez, M. 2005, *A&A*, 440, 207
- Belloni, T., Psaltis, D., & van der Klis, M. 2002, *ApJ*, 572, 392
- Belloni, T. M. 2010, in *Lecture Notes in Physics*, Vol. 794, *The Jet Paradigm*, ed. T. Belloni (Berlin: Springer), 53
- Berger, M., & van der Klis, M. 1994, *A&A*, 292, 175
- Bessell, M. S., Castelli, F., & Plez, B. 1998, *A&A*, 333, 231
- Blandford, R. D., & Begelman, M. C. 1999, *MNRAS*, 303, L1
- Blandford, R. D., & Konigl, A. 1979, *ApJ*, 232, 34
- Brocksopp, C., Corbel, S., Fender, R. P., Rupen, M., Sault, R., Tingay, S. J., Hannikainen, D., & O'Brien, K. 2005, *MNRAS*, 356, 125
- Brocksopp, C., Corbel, S., Tzioumis, A., Broderick, J. W., Rodriguez, J., Yang, J., Fender, R. P., & Paragi, Z. 2013, *MNRAS*, 432, 931
- Buxton, M. M., & Bailyn, C. D. 2004, *ApJ*, 615, 880
- Buxton, M. M., Bailyn, C. D., Capelo, H. L., Chatterjee, R., Dinçer, T., Kalemci, E., & Tomsick, J. A. 2012, *AJ*, 143, 130
- Caballero-Nieves, S. M., et al. 2009, *ApJ*, 701, 1895
- Cadolle Bel, M., et al. 2011, *A&A*, 534, A119
- Cantrell, A. G., et al. 2010, *ApJ*, 710, 1127
- Cardelli, J. A., Clayton, G. C., & Mathis, J. S. 1989, *ApJ*, 345, 245

- Casares, J., et al. 2009, *ApJS*, 181, 238
- Charles, P. A., & Coe, M. J. 2006, *Optical, ultraviolet and infrared observations of X-ray binaries*, ed. W. H. G. Lewin & M. van der Klis, 215–265
- Chun, Y. Y., et al. 2013, *ApJ*, 770, 10
- Corbel, S., Coriat, M., Brocksopp, C., Tzioumis, A. K., Fender, R. P., Tomsick, J. A., Buxton, M. M., & Bailyn, C. D. 2013a, *MNRAS*, 428, 2500
- Corbel, S., & Fender, R. P. 2002, *ApJ*, 573, L35
- Corbel, S., Fender, R. P., Tomsick, J. A., Tzioumis, A. K., & Tingay, S. 2004, *ApJ*, 617, 1272
- Corbel, S., Fender, R. P., Tzioumis, A. K., Nowak, M., McIntyre, V., Durouchoux, P., & Sood, R. 2000, *A&A*, 359, 251
- Corbel, S., Koerding, E., & Kaaret, P. 2008, *MNRAS*, 389, 1697
- Corbel, S., Nowak, M. A., Fender, R. P., Tzioumis, A. K., & Markoff, S. 2003, *A&A*, 400, 1007
- Corbel, S., Tomsick, J. A., & Kaaret, P. 2006, *ApJ*, 636, 971
- Corbel, S., et al. 2001, *ApJ*, 554, 43
- . 2013b, *MNRAS*, 431, L107
- Coriat, M., Corbel, S., Buxton, M. M., Bailyn, C. D., Tomsick, J. A., Körding, E., & Kalemci, E. 2009, *MNRAS*, 400, 123
- Coriat, M., et al. 2011, *MNRAS*, 414, 677
- Corral-Santana, J. M., Casares, J., Shahbaz, T., Zurita, C., Martínez-Pais, I. G., & Rodríguez-Gil, P. 2011, *MNRAS*, 413, L15
- Cowley, A. P. 1992, *ARA&A*, 30, 287
- Crowther, P. A., Barnard, R., Carpano, S., Clark, J. S., Dhillon, V. S., & Pollock, A. M. T. 2010, *MNRAS*, 403, L41
- DePoy, D. L., et al. 2003, in *Society of Photo-Optical Instrumentation Engineers (SPIE) Conference Series*, Vol. 4841, *Society of Photo-Optical Instrumentation Engineers (SPIE) Conference Series*, ed. M. Iye & A. F. M. Moorwood, 827–838
- Di Salvo, T., Done, C., Życki, P. T., Burderi, L., & Robba, N. R. 2001, *ApJ*, 547, 1024
- Dickey, J. M., & Lockman, F. J. 1990, *ARA&A*, 28, 215
- Diğer, T., Gilfanov, M., & Kalemci, E. 2011, in *American Institute of Physics Conference Series*, Vol. 1379, *American Institute of Physics Conference Series*, ed. E. Göğüş, T. Belloni, & Ü. Ertan, 226–227

- Dinçer, T., Kalemci, E., Buxton, M. M., Bailyn, C. D., Tomsick, J. A., & Corbel, S. 2012, *ApJ*, 753, 55
- Dinçer, T., Kalemci, E., Tomsick, J. A., & Buxton, M. 2008, in *Proceedings of the VII Microquasar Workshop: Microquasars and Beyond*, ed. E. Kalemci, (Turkey: Foca, Izmir), 61, <http://pos.sissa.it/cgi-bin/reader/conf.cgi?confid=62>
- Done, C., Gierliński, M., & Kubota, A. 2007, *A&A Rev.*, 15, 1
- Dunn, R. J. H., Fender, R. P., Körding, E. G., Belloni, T., & Cabanac, C. 2010, *MNRAS*, 403, 61
- Ebisawa, K., et al. 1994, *PASJ*, 46, 375
- Egron, E., et al. 2013, *A&A*, 550, A5
- Elias, J. H., Frogel, J. A., Matthews, K., & Neugebauer, G. 1982, *AJ*, 87, 1029
- Esin, A. A., Narayan, R., Ostriker, E., & Yi, I. 1996, *ApJ*, 465, 312
- Fabian, A. C., & Ross, R. R. 2010, *Space Sci. Rev.*, 157, 167
- Falcke, H., Körding, E., & Markoff, S. 2004, *A&A*, 414, 895
- Fender, R. 2006, *Jets from X-ray binaries*, ed. Lewin, W. H. G. & van der Klis, M., 381–419
- Fender, R., et al. 1999, *ApJ*, 519, L165
- Fender, R. P., Belloni, T. M., & Gallo, E. 2004, *MNRAS*, 355, 1105
- Fender, R. P., Gallo, E., & Jonker, P. G. 2003, *MNRAS*, 343, L99
- Fender, R. P., Hjellming, R. M., Tilanus, R. P. J., Pooley, G. G., Deane, J. R., Ogley, R. N., & Spencer, R. E. 2001, *MNRAS*, 322, L23
- Fender, R. P., Homan, J., & Belloni, T. M. 2009, *MNRAS*, 396, 1370
- Filippenko, A. V., & Chornock, R. 2001, *IAU Circ.*, 7644, 2
- Filippenko, A. V., Leonard, D. C., Matheson, T., Li, W., Moran, E. C., & Riess, A. G. 1999, *PASP*, 111, 969
- Filippenko, A. V., Matheson, T., & Ho, L. C. 1995, *ApJ*, 455, 614
- Frogel, J. A., Persson, S. E., Matthews, K., & Aaronson, M. 1978, *ApJ*, 220, 75
- Gallo, E. 2010, in *Lecture Notes in Physics*, Berlin Springer Verlag, Vol. 794, *Lecture Notes in Physics*, Berlin Springer Verlag, ed. T. Belloni, 85
- Gallo, E., Fender, R., & Corbel, S. 2003a, *The Astronomer's Telegram*, 196, 1
- Gallo, E., Fender, R. P., & Pooley, G. G. 2003b, *MNRAS*, 344, 60

- Gallo, E., Miller, B. P., & Fender, R. 2012, MNRAS, 423, 590
- Gandhi, P., et al. 2011, ApJ, 740, L13+
- Gelino, D. M., Balman, Ş., Kızıloğlu, Ü., Yılmaz, A., Kalemci, E., & Tomsick, J. A. 2006, ApJ, 642, 438
- George, I. M., & Fabian, A. C. 1991, MNRAS, 249, 352
- Gierliński, M., & Done, C. 2002, MNRAS, 337, 1373
- Gilfanov, M. 2010, in Lecture Notes in Physics, Vol. 794, The Jet Paradigm, ed. T. Belloni (Springer Berlin / Heidelberg), 17–51
- Gilfanov, M., Churazov, E., & Revnivtsev, M. 1999, A&A, 352, 182
- Greene, J., Bailyn, C. D., & Orosz, J. A. 2001, ApJ, 554, 1290
- Greiner, J., Cuby, J. G., & McCaughrean, M. J. 2001, Nature, 414, 522
- Güver, T., Özel, F., Cabrera-Lavers, A., & Wroblewski, P. 2010, ApJ, 712, 964
- Haardt, F., & Maraschi, L. 1993, ApJ, 413, 507
- Hameury, J.-M., King, A. R., & Lasota, J.-P. 1990, ApJ, 353, 585
- Hannikainen, D. C., Hunstead, R. W., Campbell-Wilson, D., & Sood, R. K. 1998, A&A, 337, 460
- Harlaftis, E. T., & Greiner, J. 2004, A&A, 414, L13
- Hjellming, R. M., & Johnston, K. J. 1988, ApJ, 328, 600
- Hjellming, R. M., & Rupen, M. P. 1995, Nature, 375, 464
- Homan, J., Buxton, M., Markoff, S., Bailyn, C. D., Nespoli, E., & Belloni, T. 2005a, ApJ, 624, 295
- Homan, J., Kong, A., Tomsick, J., Miller, J., Campana, S., Wijnands, R., Belloni, T., & Lewin, W. 2005b, The Astronomer's Telegram, 644, 1
- Homan, J., Wijnands, R., Kong, A., Miller, J. M., Rossi, S., Belloni, T., & Lewin, W. H. G. 2006, MNRAS, 366, 235
- Horne, J. H., & Baliunas, S. L. 1986, ApJ, 302, 757
- Hynes, R. I. 2005, ApJ, 623, 1026
- Hynes, R. I., Steeghs, D., Casares, J., Charles, P. A., & O'Brien, K. 2003a, ApJ, 583, L95
- . 2004, ApJ, 609, 317
- Hynes, R. I., et al. 2003b, MNRAS, 345, 292

- Ibragimov, A., Poutanen, J., Gilfanov, M., Zdziarski, A. A., & Shrader, C. R. 2005, *MNRAS*, 362, 1435
- Ingram, A., & Done, C. 2011, *MNRAS*, 415, 2323
- Jahoda, K., Swank, J. H., Giles, A. B., Stark, M. J., Strohmayer, T., Zhang, W., & Morgan, E. H. 1996, in *Society of Photo-Optical Instrumentation Engineers (SPIE) Conference Series*, Vol. 2808, Society of Photo-Optical Instrumentation Engineers (SPIE) Conference Series, ed. O. H. Siegmund & M. A. Gummin, 59–70
- Jain, R. K., Bailyn, C. D., Orosz, J. A., McClintock, J. E., & Remillard, R. A. 2001, *ApJ*, 554, L181
- Jain, R. K., Bailyn, C. D., Orosz, J. A., Remillard, R. A., & McClintock, J. E. 1999, *ApJ*, 517, L131
- Jonker, P. G., et al. 2010, *MNRAS*, 401, 1255
- Kalemci, E. 2002, PhD thesis, Univ. California, San Diego
- Kalemci, E., Dincer, T., Tomsick, J. A., Buxton, M. M., Bailyn, C. D., & Chun, Y. Y. 2013, *ApJ*
- Kalemci, E., Tomsick, J. A., Buxton, M. M., Rothschild, R. E., Pottschmidt, K., Corbel, S., Brocksopp, C., & Kaaret, P. 2005, *ApJ*, 622, 508
- Kalemci, E., Tomsick, J. A., Corbel, S., & Tzioumis, T. 2008a, *The Astronomer's Telegram*, 1378, 1
- Kalemci, E., Tomsick, J. A., Migliari, S., Corbel, S., & Markoff, S. 2008b, in *American Institute of Physics Conference Series*, Vol. 1053, American Institute of Physics Conference Series, ed. S. K. Chakrabarti & A. S. Majumdar, 201–208
- Kalemci, E., Tomsick, J. A., Rothschild, R. E., Pottschmidt, K., Corbel, S., & Kaaret, P. 2006a, *ApJ*, 639, 340
- Kalemci, E., Tomsick, J. A., Rothschild, R. E., Pottschmidt, K., Corbel, S., Wijnands, R., Miller, J. M., & Kaaret, P. 2003, *ApJ*, 586, 419
- Kalemci, E., Tomsick, J. A., Rothschild, R. E., Pottschmidt, K., & Kaaret, P. 2004, *ApJ*, 603, 231
- Kalemci, E., Tomsick, J. A., Rothschild, R. E., Pottschmidt, K., Migliari, S., Corbel, S., & Kaaret, P. 2006b, in *VI Microquasar Workshop: Microquasars and Beyond*
- Kalogera, V., & Baym, G. 1996, *ApJ*, 470, L61
- Klein-Wolt, M., & van der Klis, M. 2008, *ApJ*, 675, 1407
- Kong, A. K. H., Kuulkers, E., Charles, P. A., & Homer, L. 2000, *MNRAS*, 312, L49
- Körding, E., Falcke, H., & Corbel, S. 2006a, *A&A*, 456, 439

- Körding, E. G., Fender, R. P., & Migliari, S. 2006b, MNRAS, 369, 1451
- Kuulkers, E., et al. 2013, A&A, 552, A32
- Lasota, J.-P. 2001, New A Rev., 45, 449
- Leahy, D. A., Darbro, W., Elsner, R. F., Weisskopf, M. C., Kahn, S., Sutherland, P. G., & Grindlay, J. E. 1983, ApJ, 266, 160
- Levine, A. M., Bradt, H., Cui, W., Jernigan, J. G., Morgan, E. H., Remillard, R., Shirey, R. E., & Smith, D. A. 1996, ApJ, 469, L33
- Levine, A. M., & Corbet, R. 2006, The Astronomer's Telegram, 940, 1
- Lyubarskii, Y. E. 1997, MNRAS, 292, 679
- Maitra, D., Markoff, S., Brocksopp, C., Noble, M., Nowak, M., & Wilms, J. 2009, MNRAS, 398, 1638
- Makishima, K., Maejima, Y., Mitsuda, K., Bradt, H. V., Remillard, R. A., Tuohy, I. R., Hoshi, R., & Nakagawa, M. 1986, ApJ, 308, 635
- Malzac, J. 2013, MNRAS, 429, L20
- Markoff, S. 2010, in Lecture Notes in Physics, Berlin Springer Verlag, Vol. 794, Lecture Notes in Physics, Berlin Springer Verlag, ed. T. Belloni, 143
- Markoff, S., Nowak, M., Corbel, S., Fender, R., & Falcke, H. 2003, A&A, 397, 645
- Markoff, S., Nowak, M. A., & Wilms, J. 2005, ApJ, 635, 1203
- McClintock, J. E., Garcia, M. R., Caldwell, N., Falco, E. E., Garnavich, P. M., & Zhao, P. 2001, ApJ, 551, L147
- McClintock, J. E., Narayan, R., & Rybicki, G. B. 2004, ApJ, 615, 402
- McClintock, J. E., Remillard, R. A., Rupen, M. P., Torres, M. A. P., Steeghs, D., Levine, A. M., & Orosz, J. A. 2009, ApJ, 698, 1398
- Meier, D. L. 2001, ApJ, 548, L9
- . 2005, Ap&SS, 300, 55
- . 2012, Black Hole Astrophysics: The Engine Paradigm
- Merloni, A., Heinz, S., & di Matteo, T. 2003, MNRAS, 345, 1057
- Meyer, F., Liu, B. F., & Meyer-Hofmeister, E. 2000, A&A, 354, L67
- Meyer, F., & Meyer-Hofmeister, E. 1994, A&A, 288, 175
- Migliari, S., & Fender, R. P. 2006, MNRAS, 366, 79

- Miller-Jones, J. C. A., Jonker, P. G., Dhawan, V., Brisken, W., Rupen, M. P., Nelemans, G., & Gallo, E. 2009, *ApJ*, 706, L230
- Miller-Jones, J. C. A., Jonker, P. G., Ratti, E. M., Torres, M. A. P., Brocksopp, C., Yang, J., & Morrell, N. I. 2011, *MNRAS*, 415, 306
- Miller-Jones, J. C. A., et al. 2012, *MNRAS*, 421, 468
- Mineshige, S., & Osaki, Y. 1983, *PASJ*, 35, 377
- Mitsuda, K., et al. 1984, *PASJ*, 36, 741
- Miyamoto, S., & Kitamoto, S. 1989, *Nature*, 342, 773
- Motta, S., Belloni, T., & Homan, J. 2009, *MNRAS*, 400, 1603
- Motta, S., Muñoz-Darias, T., & Belloni, T. 2010, *MNRAS*, 408, 1796
- Motta, S., Muñoz-Darias, T., Casella, P., Belloni, T., & Homan, J. 2011, *MNRAS*, 418, 2292
- Muñoz-Darias, T., Casares, J., & Martínez-Pais, I. G. 2008, *MNRAS*, 385, 2205
- Munoz-Darias, T., Motta, S., Belloni, T., & Stiele, H. 2011, *The Astronomer's Telegram*, 3117, 1
- Narayan, R., McClintock, J. E., & Yi, I. 1996, *ApJ*, 457, 821
- Narayan, R., & Yi, I. 1994, *ApJ*, 428, L13
- Neil, E. T., Bailyn, C. D., & Cobb, B. E. 2007, *ApJ*, 657, 409
- Neilsen, J., Steeghs, D., & Vrtilik, S. D. 2008, *MNRAS*, 384, 849
- Nowak, M. A., Wilms, J., & Dove, J. B. 1999, *ApJ*, 517, 355
- O'Donnell, J. E. 1994, *ApJ*, 422, 158
- Oppenheimer, J. R., & Volkoff, G. M. 1939, *Physical Review*, 55, 374
- Orosz, J. A. 2003, in *IAU Symposium, Vol. 212, A Massive Star Odyssey: From Main Sequence to Supernova*, ed. K. van der Hucht, A. Herrero, & C. Esteban, 365
- Orosz, J. A., Bailyn, C. D., McClintock, J. E., & Remillard, R. A. 1996, *ApJ*, 468, 380
- Orosz, J. A., McClintock, J. E., Remillard, R. A., & Corbel, S. 2004, *ApJ*, 616, 376
- Orosz, J. A., Steiner, J. F., McClintock, J. E., Torres, M. A. P., Remillard, R. A., Bailyn, C. D., & Miller, J. M. 2011, *ApJ*, 730, 75
- Orosz, J. A., et al. 2001, *ApJ*, 555, 489
- . 2007, *Nature*, 449, 872

- . 2009, *ApJ*, 697, 573
- Osaki, Y. 1974, *PASJ*, 26, 429
- Özel, F., Psaltis, D., Narayan, R., & McClintock, J. E. 2010, *ApJ*, 725, 1918
- Park, S. Q., et al. 2004, *ApJ*, 610, 378
- Plotkin, R. M., Gallo, E., & Jonker, P. G. 2013, *ApJ*, 773, 59
- Pottschmidt, K. 2002, PhD thesis, Universität Tübingen
- Pottschmidt, K., et al. 2003, *A&A*, 407, 1039
- Poutanen, J., & Svensson, R. 1996, *ApJ*, 470, 249
- Prestwich, A. H., et al. 2007, *ApJ*, 669, L21
- Quataert, E., & Gruzinov, A. 2000, *ApJ*, 539, 809
- Rahoui, F., et al. 2012, *MNRAS*, 2651
- Ratti, E. M., et al. 2012, *MNRAS*, 423, 2656
- Reid, M. J., McClintock, J. E., Narayan, R., Gou, L., Remillard, R. A., & Orosz, J. A. 2011, *ApJ*, 742, 83
- Reis, R. C., Fabian, A. C., & Miller, J. M. 2010, *MNRAS*, 402, 836
- Remillard, R. A., & McClintock, J. E. 2006, *ARA&A*, 44, 49
- Revnivtsev, M. 2003, *A&A*, 410, 865
- Revnivtsev, M., Gilfanov, M., & Churazov, E. 2001, *A&A*, 380, 520
- Revnivtsev, M. G., Suleimanov, V. F., & Poutanen, J. 2013, *MNRAS*, 434, 2355
- Reynolds, C. S. 1996, PhD thesis, Univ. of Cambridge
- Reynolds, M. T., & Miller, J. M. 2013, *ApJ*, 769, 16
- Rodriguez, J., Cadolle Bel, M., Tomsick, J. A., Corbel, S., Brocksopp, C., Paizis, A., Shaw, S. E., & Bodaghee, A. 2007, *ApJ*, 655, L97
- Rodriguez, J., Corbel, S., Kalemci, E., Tomsick, J. A., & Tagger, M. 2004, *ApJ*, 612, 1018
- Rothschild, R. E., et al. 1998, *ApJ*, 496, 538
- Russell, D. M., Fender, R. P., Hynes, R. I., Brocksopp, C., Homan, J., Jonker, P. G., & Buxton, M. M. 2006, *MNRAS*, 371, 1334
- Russell, D. M., & Lewis, F. 2011, *The Astronomer's Telegram*, 3191, 1

- Russell, D. M., Maitra, D., Dunn, R. J. H., & Markoff, S. 2010, MNRAS, 405, 1759
- Russell, D. M., Miller-Jones, J. C. A., Maccarone, T. J., Yang, Y. J., Fender, R. P., & Lewis, F. 2011, ApJ, 739, L19
- Russell, D. M., et al. 2012, MNRAS, 419, 1740
- . 2013, MNRAS, 429, 815
- Rybicki, G. B., & Lightman, A. P. 1979, Radiative processes in astrophysics
- Scargle, J. D. 1982, ApJ, 263, 835
- Shahbaz, T., Fender, R., & Charles, P. A. 2001, A&A, 376, L17
- Shakura, N. I., & Sunyaev, R. A. 1973, A&A, 24, 337
- Shapiro, S. L., & Teukolsky, S. A. 1983, Black holes, white dwarfs, and neutron stars: The physics of compact objects
- Shidatsu, M., et al. 2011a, PASJ, 63, 803
- . 2011b, PASJ, 63, 785
- Silverman, J. M., & Filippenko, A. V. 2008, ApJ, 678, L17
- Smartt, S. J. 2009, ARA&A, 47, 63
- Sobolewska, M. A., Papadakis, I. E., Done, C., & Malzac, J. 2011, MNRAS, 417, 280
- Soleri, P., & Fender, R. 2011, MNRAS, 413, 2269
- Soleri, P., et al. 2010, MNRAS, 406, 1471
- Steiner, J. F., McClintock, J. E., & Reid, M. J. 2012, ApJ, 745, L7
- Stiele, H., Motta, S., Muñoz-Darias, T., & Belloni, T. M. 2011, MNRAS, 1664
- Sunyaev, R., & Revnivtsev, M. 2000, A&A, 358, 617
- Sunyaev, R. A., & Titarchuk, L. G. 1980, A&A, 86, 121
- Sunyaev, R. A., & Truemper, J. 1979, Nature, 279, 506
- Tanaka, Y., & Shibazaki, N. 1996, ARA&A, 34, 607
- Tarana, A., Bazzano, A., Ubertini, P., & Zdziarski, A. A. 2007, ApJ, 654, 494
- Tomimatsu, A., & Takahashi, M. 2001, ApJ, 552, 710
- Tomsick, J. A. 2010, The Astronomer's Telegram, 2384, 1
- Tomsick, J. A., Corbel, S., & Kaaret, P. 2001, ApJ, 563, 229
- Tomsick, J. A., & Kaaret, P. 2000, ApJ, 537, 448

- Uttley, P., Wilkinson, T., Cassatella, P., Wilms, J., Pottschmidt, K., Hanke, M., & Böck, M. 2011, MNRAS, 414, L60
- Uzdensky, D. A. 2004, ApJ, 603, 652
- van den Heuvel, E. P. J., & Heise, J. 1972, Nature Physical Science, 239, 67
- van der Klis, M. 1989, in Timing Neutron Stars, ed. H. Ögelman & E. P. J. van den Heuvel, 27–+
- van Straaten, S., van der Klis, M., di Salvo, T., & Belloni, T. 2002, ApJ, 568, 912
- Webb, N. A., Naylor, T., Ioannou, Z., Charles, P. A., & Shahbaz, T. 2000, MNRAS, 317, 528
- Wilkinson, T., & Uttley, P. 2009, MNRAS, 397, 666
- Wilms, J., Nowak, M. A., Pottschmidt, K., Pooley, G. G., & Fritz, S. 2006, A&A, 447, 245
- Wu, Q., & Gu, M. 2008, ApJ, 682, 212
- Yamaoka, K., et al. 2010, The Astronomer's Telegram, 2380, 1
- Yan, S.-P., Ding, G.-Q., Wang, N., Qu, J.-L., & Song, L.-M. 2013, MNRAS, 434, 59
- Yan, Z., & Yu, W. 2012, MNRAS, 427, L11
- Yuan, F. 2001, MNRAS, 324, 119
- Zdziarski, A. A., Gierliński, M., Mikołajewska, J., Wardziński, G., Smith, D. M., Harmon, B. A., & Kitamoto, S. 2004, MNRAS, 351, 791
- Zdziarski, A. A., Lubiński, P., & Smith, D. A. 1999, MNRAS, 303, L11
- Zdziarski, A. A., Poutanen, J., Mikołajewska, J., Gierlinski, M., Ebisawa, K., & Johnson, W. N. 1998, MNRAS, 301, 435
- Zhang, W., Jahoda, K., Swank, J. H., Morgan, E. H., & Giles, A. B. 1995, ApJ, 449, 930
- Zurita, C., Durant, M., Torres, M. A. P., Shahbaz, T., Casares, J., & Steeghs, D. 2008, ApJ, 681, 1458
- Zurita, C., et al. 2002, MNRAS, 334, 999